Optimization of the internal quantum efficiency of luminescent devices based on GaN and operating from the yellow to the red

Thi Huong Ngo

THÈSE

Pour obtenir le grade de

Docteur

Délivré par **l'Université de Montpellier**

Préparée au sein de l'école doctorale **I2S**

Et de l'unité de recherche **L2C-UMR 5221**

Spécialité : **Physique**

Présentée par **Thi Huong NGO**

Optimisation du rendement quantique des dispositifs luminescents à base de nitrures opérant du jaune au rouge

Soutenue le 05.10.2017 devant le jury composé de

Lucyna FIRLEJ	Professeur, Univ. Montpellier	Présidente
Maria TCHERNYCHEVA	Ingénieur-chercheur, C2N-CNRS	Rapportrice
Alexey KAVOKIN	Professeur, Univ. Southampton	Rapporteur
Guillaume CASSABOIS	Professeur, Univ. Montpellier	Examinateur
Pierre RUTERANA	Directeur de Recherche, CNRS	Examinateur
Hai Son NGUYEN	Maitre de conférences, EEA/INL	Examinateur
Benjamin DAMILANO	Chargé de Recherche, CRHEA-CNRS	Examinateur
Bernard GIL	Directeur de Recherche, CNRS	Directeur

Acknowledgements

First, I would like to warmly thank Lucyna Firlej for accepting to be the president of the jury. I would like to address many thanks to Maria Tchernycheva and Alexey Kavokin for accepting to report about my thesis. I would also like to warmly thank Pierre Ruterana, and Hai Son Nguyen for accepting to be the members of the jury. I am also thankful to Guillaume Cassabois for introducing me to my supervisor and for accepting to be a member of the jury. This is a great honour to me.

My greatest thanks go to my supervisor Bernard Gil, for offering me opportunity to be his PhD student at L2C and for his insightful guidance. His advice and support throughout my thesis have been invaluable. He has always been available for any kind of help, any discussion and for the scientific writing.

I also want to address my sincerest thanks to my co-supervisor, Benjamin Damilano, for his kind guidance in growing the samples I studied and help in scientific writing. His useful discussions helped me to complete my understanding of my research. I would also like to thank my two supervisors for their patient guidance and for always forgiving my mistakes.

This is also a great pleasure for me to acknowledge my previous and current colleagues in L2C and CRHEA for their help. I am thankful to Pierre Valvin for his many teaching and endless helpful discussions regarding the photoluminescence experimental setup. I would also like to thank Kaddour Lekhal, Aimeric Courville and Philippe de Mierry for growing some of the samples I used for my experiments. Many thanks also to Daniel Rosales, Julien Selles, and Rereao Hahe for being nice friends and sharing with me my first period time and training me to what has been since the end of my master, this new life in France, in a research laboratory. Thanks also to Thi Quynh Phuong Vuong, Mohammed Mohammed Ali, Isabell Gross and Clément Beaufils, for sharing good times, in our small office.

I would like to extend my thanks to the full administration staff and in particular to Christelle Eve, Adoration Gabillard and Jean-Christophe Art for taking care of the administration procedure during three years of my thesis. I would also like to thank Christian L'hénoret for sharing nice times in his realm, the workshop, and Patrick Ejarque for his courtesy and his coffee services.

I would also like to thank GaNEX and his leader, Jean-Yves Duboz, for financial support. It has been a real luck for me to be a student of this excellent network. I had the great chance to learn a lot about physics of nitrides-semiconductors during the annual meeting, the summer and winter schools of GaNEX.

Finally, I am grateful to my parents, who are kind and traditional Vietnamese people. They have been always supporting me with all the love that can be given. I would also like to thank my brother and my sister for their support and encouragements during these three years.

Montpellier, October 2017

Ngo Thi Huong

Table of Contents

List of abbreviations

2D	Two-dimentional
3D	Three-dimentional
AE	Auger effect
Al	Aluminum
AlGaN	Aliminum gallium nitride
AlN	Aluminum nitride
CWPL	Continuous wavelength photoluminescence
EQE	External quantum efficiency
Ga	Gallium
GaN	Gallium nitride
In	Indium
InGaN	Indium gallium nitride
InN	Indium nitride
IQE	Internal quantum efficiency
LDs	Laser diodes
LEDs	Light emitting diodes
LT	Low temperature
ML	Monolayer
MOCVD	Metal organic chemical vapor deposition
MQW	Multiple quantum well
N	Nitrogen
NIR	Near-infrared
NUV	Near ultraviolet
PEPD	Photo-excitation power dependent
PL	Photoluminescence
PSF	Phase-space filling
QCSE	Quantum confined Stark effect
QW	Quantum well
RT	Room temperature
Si	Silicon
SiC	Silicon carbide
SQW	Single quantum well
SRH	Shockley-Read-Hall
T	Temperature
TRPL	Time-resolved photoluminescence
UV	Ultraviolet

Résumé

Les diodes électroluminescentes bleues à base de puits quantiques (Ga,In)N/GaN ont fait l'objet de nombreuses recherches et sont maintenant extrêmement efficaces (leur rendement quantique externe approche 90%). Elles sont l'élément clé de l'éclairage à source solide qui est adopté de manière de plus en plus importante en raison de son efficacité. Toutefois, la fabrication de diodes électroluminescentes vertes ou émettant à plus grande longueur d'onde se heurte à de nombreux challenges. La première difficulté est liée à des propriétés intrinsèques de l'alliage (Ga,In)N. Cet alliage présente toujours un désordre atomique relativement important. De plus, de forts champs électriques internes existent le long de la direction 0001. Ils réduisent le recouvrement des fonctions d'ondes des électrons et des trous, ce qui peut entraîner un faible rendement de luminescence. Une autre difficulté est liée à la croissance des structures à puits quantiques (Ga,In)N/GaN. Les conditions de croissances optimales du (Ga,In)N et GaN sont très différentes. Par exemple, une température de croissance typique du (Ga,In)N par épitaxie en phase vapeur aux organométalliques est de 700°C, alors qu'elle est de 1000°C pour du GaN. Les paramètres de maille d'InN et GaN sont très différents (>10%), ce qui pose des problèmes de qualité cristalline liés à la forte contrainte élastique entre les alliages (Ga,In)N à forte teneur en In et GaN.

Le but de ce travail de thèse est de trouver les voies permettant l'amélioration des composants émetteurs de lumière à base de puits quantiques (Ga,In)N/GaN opérant du vert-jaune jusqu'au rouge. Pour ce faire, nous avons étudié des échantillons avec des designs spécifiques : i) des puits quantiques multiples épitaxiés selon la direction 0001 avec différentes compositions en In et épaisseurs de puits quantiques, ii) des puits quantiques multiples épitaxiés selon la direction 0001 avec des couches d'(Al,Ga)N de compensation de contrainte, iii) des puits quantiques simples épitaxiés selon la direction 0001 avec une composition et une épaisseur variable, avec ou sans couche d'(Al,Ga)N de compensation de contrainte, et iv) des puits quantiques multiples $In_xGa_{1-x}N/In_yGa_{1-y}N$ épitaxiés sur des couches tampons relaxés d'$In_yGa_{1-y}N$ selon la direction semi-polaire 11-22. Le couplage lumière-matière dans ces échantillons a été étudié par des mesures de spectroscopie de photoluminescence (en fonction de la puissance d'excitation, avec résolution temporelle, en fonction de la température). Dans ce type d'expérience,

l'échantillon est excité par des photons. Ce type d'excitation présente l'avantage de requérir des échantillons dont la structure est plus simple que des dispositifs émetteurs tels que des lasers ou des diodes électroluminescentes. De plus, l'excitation optique permet de s'affranchir des phénomènes liés à l'injection électrique des porteurs tels que des pertes via les électrodes et les couches de contacts ou une injection inhomogène dans toute la surface du dispositif.

Dans cette thèse, nous avons étudié le rendement quantique interne en fonction de la puissance d'excitation pour tous les échantillons. Le rendement quantique interne varie selon les contributions respectives de trois canaux de recombinaisons principaux : les recombinaisons non-radiatives de type Schockley-Read-Hall, les recombinaisons radiatives bande-à-bande, et les recombinaisons non-radiatives de type Auger.

A très faible excitation, le rendement quantique interne est gouverné principalement par les recombinaisons non radiatives de type Schockley-Read-Hall et les recombinaisons radiatives. Nous avons pu évaluer le rendement quantique interne à basse température à partir de mesures de temps de déclin de photoluminescence et en appliquant le modèle de Lotka-Volterra décrivant un comportement proie-prédateur des excitons. L'ensemble de nos échantillons épitaxiés selon la direction polaire émettant du vert au rouge a un rendement quantique interne compris entre 50 et 57%. Le fait d'insérer une couche d'(Al,Ga)N dans les structures à puits quantiques multiples améliore la qualité cristalline et le rendement quantique interne en dépit de l'augmentation du champ électrique interne.

Une réduction importante du rendement quantique interne est mesurée pour de fortes puissances d'excitation. En appliquant un modèle ABC à nos données expérimentales dans ce régime de forte excitation, nous avons pu montrer que les recombinaisons de type Schockley-Read-Hall ont tendance à saturer, que les recombinaisons radiatives diminuent et que les recombinaisons Auger sont déclenchées par l'intervention d'effets de remplissage de bande. Parmi ces trois mécanismes, nous avons démontré que l'effet Auger est dominant à fort niveau d'excitation. Il paraît surprenant d'observer un effet Auger dominant pour un matériau semi-conducteur à large bande interdite mais ceci est en fait lié à l'accumulation d'une forte densité de porteurs dans les puits quantiques. En effet, la présence d'un fort champ électrique interne dans les puits quantiques a pour conséquence une durée de vie radiative des excitons très longue. Ceci

induit une densité de porteurs élevée dans les puits quantiques puisqu'en régime stationnaire d'excitation la densité de porteurs est donnée par le taux de génération multiplié par la durée de vie radiative si l'on néglige les phénomènes non radiatifs. De plus, les fluctuations de potentiel de l'alliage (Ga,In)N produit des centres de localisation dans lesquels le porteurs vont également s'accumuler. Ces deux effets vont donc avoir tendance à augmenter la densité de porteurs et donc favoriser les processus de recombinaison non-radiatifs de type Auger.

Une manière d'éviter les conséquences néfastes d'un fort champ électrique interne est d'utiliser des orientations cristallines avec l'axe 0001 fortement incliné par rapport à la direction de croissance. C'est le cas de la direction 11-22, selon laquelle nous avons épitaxié des échantillons émettant dans le bleu et dans le rouge. La durée de vie radiative est diminuée de plusieurs ordres de grandeur dans le cas des puits quantiques épitaxiés selon l'axe 11-22 comparée aux échantillons standards pour une longueur d'émission identique. Une conséquence bénéfique de ceci est que le seuil à partir duquel les effets Auger deviennent dominants est décalé à des densités d'excitation 200 fois plus élevées pour l'échantillon émettant dans le rouge. Le processus de recombinaison est modifié significativement puisque la photoluminescence résolue en temps indique que l'on passe d'un déclin composé de deux composantes pour l'orientation polaire à un temps de déclin mono-exponentiel pour l'orientation 11-22.

Ces résultats et leur analyse sont reportés en détails au cours des cinq chapitres de cette thèse organisée selon les chapitres suivants:

- Le chapitre I introduit quelques informations générales sur les nitrures d'éléments III cristallisant dans la phase wurtzite. En particulier les phénomènes de polarisation spontanée et piézoélectrique à l'origine des champs électriques internes dans les hétérostructures à base de nitrures sont décrits. Les matériaux AlN, GaN et InN ont des paramètres de maille cristalline très différents, ce qui induit de fortes contraintes dans les hétérostructures qui peuvent être à l'origine de défauts. D'autre part la déformation de la maille cristalline induit également de fortes polarisations piézoélectriques. Les propriétés optiques des hétérostructures sont alors affectées par la présence du champ électrique interne causant un effet Stark confiné quantique. Les mécanismes décrivant les différents processus de recombinaison et leur impact sur le rendement quantique interne sont discutés.

- Dans le chapitre II, nous étudions la dynamique du déclin de photoluminescence de trois échantillons émettant dans le jaune épitaxiés selon l'orientation polaire pour lesquels le couple (composition en In, épaisseur de puits quantique) varie. Le but est d'évaluer l'impact du champ électrique interne et du désordre d'alliage sur les propriétés optiques tout en ayant une longueur d'onde d'émission fixée. Pour cela, nous avons mené des expériences de photoluminescence résolue en temps et de photoluminescence avec excitation continue pour des températures variant de 8K à température ambiante. Pour tous les échantillons, l'intensité de photoluminescence décroit lorsque la température augmente. La chute d'intensité est activée thermiquement avec des températures d'activation élevées mettant en évidence des processus de recombinaison non-radiatifs efficaces. Les expériences de photoluminescence résolue en temps permettent de mettre en évidence le désordre d'alliage dans nos échantillons d'après l'observation d'une cinétique de recombinaison mettant en jeu deux processus: un premier avec un temps de déclin long et un second avec un temps de déclin court. Finalement, nous concluons qu'une structure à puits quantique comportant une forte composition en In et une faible épaisseur de puits quantiques est obligatoire pour obtenir une émission optimale dans le jaune.

- Dans le chapitre III, le rendement quantique interne d'une série de puits quantiques polaires est étudié. Une couche de compensation de contrainte d'$Al_{0.2}Ga_{0.8}N$ d'épaisseur variable est insérée et la composition en In est également modifiée de manière à viser une émission dans le jaune-rouge. Les effets principaux de l'insertion de la couche d'$Al_{0.2}Ga_{0.8}N$ est une amélioration de la qualité cristalline et une augmentation du champ électrique interne. Ce dernier effet induit un décalage vers le rouge de l'énergie d'émission des puits quantiques (Ga,In)N et aussi une diminution du taux de recombinaison radiative. Les expériences de photoluminescence résolue en temps montrent l'existence de deux régimes de recombinaison avec une cinétique rapide ou plus lente. La proportion entre ces deux régimes varie avec l'épaisseur d'(Al,Ga)N. En utilisant, le modèle proie-prédateur décrivant la recombinaison d'excitons dans un milieu inhomogène, nous avons déterminé le rendement quantique interne à basse température. Nous trouvons que le rendement quantique interne augmente avec l'épaisseur de l'(Al,Ga)N, en accord avec les observations concernant la photoluminescence avec une excitation continue. Des expériences de photoluminescence en fonction de la puissance d'excitation montrent que l'effet Auger devient le mécanisme de recombinaison non-radiative dominant à forte densité d'excitation. L'insertion d'une couche d'(Al,Ga)N permet de réduire le coefficient

de recombinaison de type Schockley-Read-Hall, mais en contrepartie l'apparition de phénomènes de recombinaison Auger intervient à plus faible densité d'excitation que pour des échantillons sans (Al,Ga)N.

- Le chapitre IV est dédié à l'étude des propriétés optiques d'une série complète de simples puits quantiques polaires (Ga,In)N avec une longueur d'onde d'émission variant du bleu au rouge. Le but est d'obtenir une meilleure compréhension des phénomènes de recombinaison mis en jeu sur une gamme de longueur d'onde étendue. L'avantage d'avoir un simple puits quantique est que cela permet de connaître de manière plus précise la densité de porteurs présents dans le puits quantique. La série comporte des échantillons avec des compositions en In et des épaisseurs de puits quantiques variables. La structure de certains échantillons inclut également une couche intercalaire d'(Al,Ga)N. Les expériences de photoluminescence conduites sur ces échantillons montrent des comportements globaux similaires aux puits quantiques multiples. Par exemple la durée de vie radiative augmente lorsque la longueur d'émission du puits quantique augmente du fait de l'effet Stark confiné quantique. Une différence notable est que l'effet Auger devient dominant pour des puissances d'excitation plus faibles que pour des puits quantiques multiples. Nous mesurons que, dans des conditions de forte excitation, c'est-à-dire dans une gamme d'excitation pour laquelle l'effet Auger domine, la variation du rendement quantique interne (IQE) avec la puissance d'excitation est décrite par une loi de puissance indépendante de la structure de l'échantillon: $IQE=IQE_{max}-alogP$, où a vaut approximativement 1/3. Un travail théorique est nécessaire afin d'expliquer quantitativement cette observation.

- L'objectif du chapitre V est de parvenir à décorréler les influences de l'effet Stark confiné quantique et de la localisation sur le seuil d'apparition de l'effet Auger via l'étude des propriétés de photoluminescence de puits quantique (Ga,In)N semi-polaires (11-22). Un échantillon composé d'un puits quantique multiple $In_xGa_{1-x}N/GaN$ émettant dans le bleu et un échantillon $In_xGa_{1-x}N/In_yGa_{1-y}N$ épitaxié sur une couche relaxée d'$In_yGa_{1-y}N$ émettant dans le rouge sont étudiés. Du fait de la présence de la couche d'$In_yGa_{1-y}N$ relaxée dans le deuxième échantillon, la composition en In des puits quantiques est beaucoup plus importante. Ceci explique la forte différence de longueur d'onde d'émission entre les deux échantillons.

Les études de photoluminescence en fonction de la température et de photoluminescence résolues en temps montrent que l'échantillon émettant dans le rouge présente une forte

localisation des porteurs que l'on peut relier à la forte composition en In des puits quantiques de cet échantillon. Les temps de déclin de photoluminescence sont des ordres de grandeurs plus faibles que pour les échantillons polaires, ce qui montre le faible impact de l'effet Stark confiné quantique sur les échantillons semi-polaires. En conséquence, le seuil à partir duquel le rendement quantique interne diminue est décalé à des densités d'excitation beaucoup plus élevées.

En résumé, nous avons trouvé que l'influence combinée de l'effet Stark confiné quantique et de la localisation des porteurs augmente la densité des excitons photo-créés dans les puits quantiques, ce qui a pour conséquence de favoriser les processus Auger qui deviennent le mécanisme de recombinaison dominant à forte densité d'excitation. L'effet Auger intervient particulièrement rapidement dans le cas de structures polaires émettant dans le rouge, car la durée de vie radiative des porteurs est particulièrement élevée pour ce type d'échantillons du fait de l'effet Stark confiné quantique. Pour des échantillons émettant à grande longueur d'onde à base de puits quantiques (Ga,In)N orientés selon l'axe polaire, le rendement quantique interne dépend de la qualité cristalline (principalement reliée à la composition en In) et de l'impact de l'effet Stark confiné quantique. Notre étude montre que pour obtenir une émission de lumière efficace dans le jaune, une forte composition en In et des puits quantique de (Ga,In)N fins sont nécessaires pour éviter les effets néfastes de l'effet Stark confiné quantique. Ceci n'est pas forcément possible à mettre en œuvre du fait des contraintes liées à l'épitaxie de ce type d'échantillons. L'utilisation d'orientations semi-polaires permet de s'affranchir des problèmes liés à l'accumulation de fortes densités de porteurs et donc pourraient être idéales pour l'émission à grande longueur d'onde pourvue que l'on parvienne à développer des couches de (Ga,In)N relaxées de très bonne qualité cristalline.

INTRODUCTION

During the recent years, optoelectronic devices based on wurtzite III-Nitride, including (Al,Ga,In)-N, have been subject of a great number of studies, in correlation with their potential applications. The interest of nitride materials is linked to the large range of their band-gap energies which scale from deep ultraviolet (UV) to near-infrared (NIR),[1] see Fig. 1. In addition, the fundamental bandgaps of nitride materials are direct in reciprocal space making the coupling of the light with the electronic states in the matter very efficient. Thanks to these direct bandgap configurations, and to their values, the III-nitride semiconductors have thus many applications for the solid-state lighting, such as light emitting diodes (LEDs), laser diodes (LDs), photodetectors.

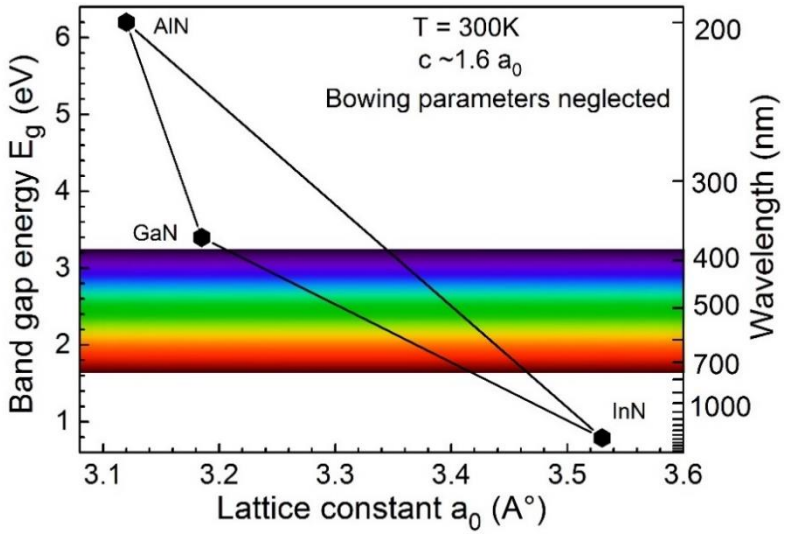

Figure 1. The bandgap energies of the wurtzite AlN, GaN, InN plotted versus their in-plane lattice constants at room temperature.[1]

The energy bandgap of InGaN/GaN quantum wells (QWs) can cover the whole range of the visible light thanks to the indium composition-dependence, well-width-dependence of their transition energy.[2] InGaN-based blue LEDs can have very high external quantum efficiency (EQE) up to 90%.[3,4] However, as seen in Fig. 2, the EQE of the III-Nitride LEDs reduces dramatically when the emission wavelength goes toward the red region of the visible light spectrum.[5] High efficiency red LEDs are obtained using phosphide-based materials.[6] But unfortunately, the EQE of this kind of materials also strongly reduces at green region. The lack of a perfect covering of the visible light spectrum using one given material (and thus the lack of a single technology) led us *to focus*

on the investigation of the optical properties of InGaN/GaN quantum wells (QWs) optimized for efficient green-yellow and red-light emissions.

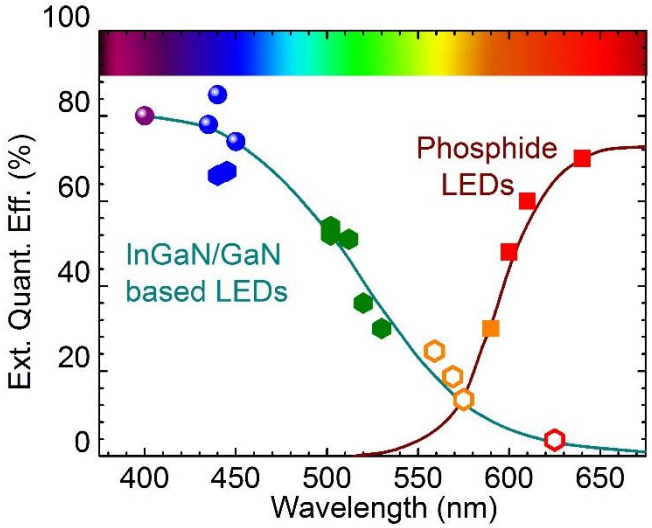

Figure 2. The maximum of external quantum efficiency (EQE) of nitride and phosphide LEDs.[5]

The external quantum efficiency is determined by following equation:

$$EQE = \eta_{injection}\, \eta_{extration}\, IQE \qquad (1)$$

where $\eta_{injection}$ = Injection efficiency

$\eta_{extration}$ = Extraction efficiency

IQE = internal quantum efficiency

The green-yellow (Ga,In)N-based LEDs that are commercialized are dominantly grown by metal organic chemical vapor deposition (MOCVD). The EQE at 20 mA current injection of about 13.4% (@562 nm) was published for LEDs grown on semi-polar (11-22) bulk substrates[7] and EQE of 24.7% (@559 nm) and 13.3% (@576 nm) were published for LEDs grown on c-plane sapphire substrates.[8] A direct comparison of EQE remains difficult because the injection and extraction efficiencies are not known from these publications. Fortunately, the IQE can be calculated in terms of the proportion of the radiative recombination rate relatively to the total recombination rate[1]. The later can be easily measured; and it is usually obtained by performing time-resolved photoluminescence (TRPL) experiments. Therefore, in this study, *we decided to investigate the IQE of InGaN/GaN QW structures by means of photoluminescence (PL) measurements.* We do not forget that electrical injection and optical one does not stimulate exactly the same recombination process and that a company wishing to sell LEDs should include in its catalogue the performances obtained in the context of an electrical injection. However optical injection is obviously cheaper in terms of number of steps of the process and it is

very much adapted to research laboratories like the one where I made this work, when one does not benefit of funding in amounts comparable to those of money-making companies. The experimental trends are *mutatis mutandis* identical and the mismatch between the results obtained in case of an electrical injection and an optical one are tiny enough to permit to validate our conclusions.

Figure 3 reports the evolution of the IQE versus injection current density for polar and semi-polar oriented blue-emitting InGaN LEDs.[9] The IQE slightly increases at low excitation range for both cases of polar and semi-polar samples. When increasing the injection density, the IQE dramatically reduces after passing through a maximum value. This phenomenon is well known in the literature as the "efficiency droop" in the InGaN-based light emitting devices. High power spontaneous emission is difficult to achieve whatever the emission wavelength is, in correlation with the onset of droop that limits the IQE under either photo-injection or electrical one.[9] To enhance the IQE, it requires to elucidate the origins of droop efficiency and to eventually cure them. After long standing debates in the literature,[10-13] Auger non-radiative recombination has been demonstrated to be the principal mechanism that contribute to the reduction of IQE under high excitation condition in the InGaN-based blue light emitters.[14-16]

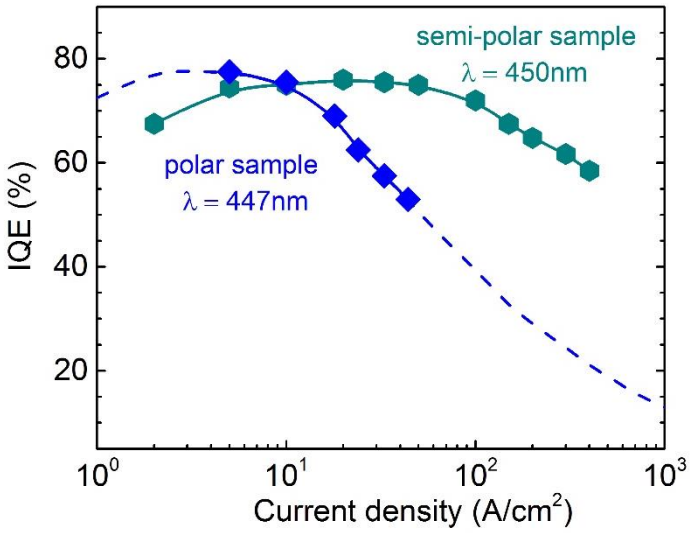

Figure 3. The internal quantum efficiency of the blue semi-polar and polar InGaN-based LEDs as a function of the injection current density (reproduced from Ref. 9).

In Fig. 3 is shown the impact of quantum confined Stark effect (QCSE) for onseting the droop at lower value of current density in case of the polar sample (strong QCSE) compared with higher injection values for growth along a semi-polar orientation (weak QCSE) in structures with identical IQEs. This result relates the importance of the QCSE in the InGaN

QWs. This electric field pushes electron and hole to opposite sides of the hetero-interfaces and hence causes a reduction of their overlap wave-functions. This reduces the radiative recombination rate and it may also promote Auger non-radiative recombination via the electron-electron and hole-hole repulsions.[17] The InGaN being residually n-type the electron-electron repulsion dominates and the escape of one electron away from the QW region is favoured leading to nnp Auger type non-radiative recombination.

As we mentioned earlier, our confining material is a ternary alloy: InGaN. Differences of relative sizes of indium, gallium, and nitrogen atoms combined with the difference of Ga-N and In-N bond length, leading at the end to a randomly distribution of gallium and indium atoms in the InGaN layer. This induces fluctuations of indium composition in complement to the fluctuations of InGaN quantum well thickness. Consequently, carriers are also trapped into localized potential minima.[18-21] The carrier localization prevents carriers to migrate toward non-radiative recombination centers and hence improves the IQE at low excitation level. However, it also leads to a more efficient non-radiative Auger recombination under high excitation condition.[22] So the conditions of occurrence of the different non-radiative recombination mechanisms (Shockley-Read-Hall and Auger) are thus complex functions of joint contributions of the internal electric field and of the localization of carriers to interfaces and to indium rich regions. Therefore, in the end of this thesis, *we will investigate impacts of QCSE and carrier localization on IQE by means of PL measurements for a broad range of visible light: from the blue to the red and we will tentatively contribute to disentangle their contributions.*

All results of this studies will be reported in five chapters organized in the following structure:

- Chapter I introduces some general information about the wurtzite III-Nitride semiconductors. After quoting the departure of the crystalline parameters from their ideal values, the origin of the spontaneous polarization field in the wurtzite nitride materials is described. As the AlN, GaN, and InN have different lattice constants, and they differ from the lattice parameter of the substrate, the lattice mismatch between different layers is more or less compensated during the growth of the heterostructures, thus creating built-in strain fields. These strain-fields not only create dislocations in the whole structure but also produce a piezoelectric polarization complementary to the spontaneous polarization one. The continuity of the total polarization is broken at hetero-interfaces, which according to Maxwell's equations produces an electric field into each of the different layers assembled

to form the heterostructure. Under these conditions, the optical properties of semiconductors are modified due to the QCSE. Then, the mechanisms of different recombination channels are discussed to show how they impact the value of the IQE.

- In chapter II, we study the dynamics of the photoluminescence (PL) decay for three yellow light emitting samples grown along the polar orientation for which the varying quantity is the pair (indium composition, quantum well thickness) that is made to vary in order to investigate how big are the impacts of the internal electric field and of the alloy disorder effect on their optical properties. To do so, TRPL and continuous wavelength PL (CWPL) spectroscopies are carried out from 8 K to room temperature (300 K) on all these three samples. The temperature dependent PL measurement always indicates a collapse of the PL intensity with increasing T. These collapses are ruled by large values of activation temperature as an evidence of efficient non-radiative recombination rates when increasing temperature. From the TRPL spectroscopy, we find the evidence of an alloy disorder in our samples according to the observation two-mode recombination kinetics: a long and a short decay times with temperature. Finally, we find that the prescription of simultaneous high indium composition and thin QW is mandatory - as well as optimized growth conditions - for the optimization of the efficiency of yellow light emission in heterostructures based on InGaN/GaN QWs.
- In chapter III, the light-matter interaction internal quantum efficiency is examined using a series of polar (In,Ga)N multiple quantum well (MQW) modified by adding a strain-compensating $Al_{0.2}Ga_{0.8}N$ interlayer and by changing the indium composition. In such structures, the thicknesses of the $Al_{0.2}Ga_{0.8}N$ layers are calculated to compensate the elastic strain and to improve the material quality. Inserting such $Al_{0.2}Ga_{0.8}N$ layers modifies the potential drop near the QW layer and increases the electric field in the InGaN layer. This produces a red-shift of the emission energy thanks to this increasing the internal electric field inside the InGaN QW and it also decreases the recombination rate. The low photo-excitation density TRPL spectroscopy shows the existence of two different recombination regimes with fast and slow kinetics at proportions varying with AlGaN thickness. Then, by using the model developed for samples of inhomogeneous quality, the IQE is determined and we find its value to increase with increasing thickness of AlGaN layer, in agreement with the evolution of the CWPL intensity in the whole set of samples. Then, power dependent measurements are carried out to calibrate the importance of Auger recombination in the high excitation range and an ABC model is used to estimate the

contribution of difference recombination channels on the evolution of the IQE. The Auger effect is demonstrated as the dominating non-radiative recombination channel at high excitation regime. Intercalating an AlGaN strain-compensating layer reduces the coefficient of the SRH non-radiative recombination rates but it also triggers the onset of Auger recombination at lower threshold power density.

- To go towards a better understanding and to get the whole information regarding the impact of different recombination channels, chapter IV reports the optical properties of a complete series of single quantum well (SQW) polar samples with emission wavelengths ranging from blue to red. Designs of this series samples are chosen to be varied by changing the indium composition, the well thickness, and adding AlGaN interlayer to pursue with the examination of the influence of carrier localization and with the impact of QCSE, respectively. The trends of the photoluminescence measurements measured of the series of the MQWs samples are reproduced for this series of samples. Similar results are found: the decay times increase with increasing of the emission wavelength from the blue-light emitting sample to the red-light emitting sample thanks to the increase of the QCSE. Moreover, **at a given wavelength**, the onset of Auger effect in **SQW** samples occurs **at lower value** of the threshold power density than in **MQW** samples. The Auger effect is also found to be the main reason of reduction of the IQE at high excitation condition. We find that under condition of efficient Auger recombination, the variation of the IQE with photo-excitation density is ruled by a universal power law independent of the design: IQE = IQE_{MAX} – a $\log_{10}P$ where a is approximately 1/3. This observation will require to be interpreted by theorists.
- To disentangle the influences of the QCSE and of the localization effect on the photo-excitation threshold for the reduction of the IQE at high excitation level, details of optical properties of semi-polar samples are reported in chapter V. A blue InGaN/GaN QW grown on a (11-22) GaN buffer layers and a red InGaN/InGaN QW sample grown on a (11-22) InGaN buffer layers to get high efficiency are studied. The In composition of the InGaN/InGaN sample is estimated higher than that of the InGaN/GaN sample, although they are grown under similar growth conditions. Investigation of the temperature-dependent PL and the TRPL measurements give evidence of strong localization in the red-samples which is correlated to strong fluctuations of indium composition in In-rich InGaN/InGaN QWs. In addition, the small values of the decay times obtained by using the TRPL spectroscopy measurement indicate a weak impact of the QCSE on the carrier

recombination of these two samples. Then, at a given emission wavelength, the threshold for reduction of the IQE in the semi-polar samples is found more than 200 times higher than in the polar-oriented samples.

In summary, we found that the combined influences of QCSE and of carrier localization increase the carrier density that promotes Auger processes which become the dominant recombination channel at high excitation levels. We believe that the QCSE plays a more important role than localization phenomena do. Auger effect occurs very rapidly under high injection regime, in case of red-light emitting structures grown along the polar orientation. This is in straightforward correlation with the huge QCSE which reduces the recombination rate and increases the standing time of carriers in the QWs. In polar-oriented long-wavelength light emitters based on InGaN/GaN QW, there is a trade-off between crystalline quality, relating to the In composition, and the impact of QCSE, correlating with the width of the QW. Our study shows that to grow high efficiency yellow emission along the polar orientation, it requires high In composition and thin QW to get rid of QCSE. The QCSE bottlenecks the realization of yellow-red light emitting devices based on nitrides grown along the polar direction. To enhance the IQE, and the injection density beyond which Auger effect dominates the recombination rate, it is mandatory to reduce the amount carriers localized by the electric field at hetero-interfaces and thus samples grown along semi-polar orientation are very much welcome. However, high indium contents are required, which shifts the difficulties.

References

1. E. F. Schubert, Light-Emitting Diode, Cambridge University Press, (2003)
2. B. Damilano and B. Gil, J. Phys. D: Appl. Phys. **48**, 403001 (2015)
3. Y. Narukawa, M. Ichikawa, D. Sanga, M. Sano, and T. Mukai, J. Phys. D, Appl. Phys. **43**, 354002 (2010)
4. Christophe A. Hurni, Appl. Phys. Lett. **106**, 031101 (2015)
5. M. Auf der Maur, A. Pecchia, G. Penazzi, W. Rodrigues, and A. Di Carlo, Phys. Rev. Lett. **116**, 027401 (2016)

6. M. R. Krames, M. Ochiai-Holcomb, G. E. Höfler, C. Carter-Coman, E. I. Chen, I.-H. Tan, P. Grillot, N. F. Gardner, H. C. Chui, J.-W. Huang, S. A. Stockman, F. A. Kish, M. G. Craford, T. S. Tan, C. P. Kocot, M. Hueschen, J. Posselt, B. Loh, G. Sasser, and D. Collins, Applied Physics Letters **75**, 2365 (1999)

7. H. Sato, R.B. Chung, H. Hirasawa, N. Fellows, H. Masui, F. Wu, et al. Appl. Phys. Lett. **92**, 221110 (2008)

8. S. Saito, R. Hashimoto, J. Hwang, S. Nunoue. Appl. Phys. Express. **6**, 111004 (2013)

9. R. Nakamura, and M. R. Krames, Proc. of the IEEE **101**, 2211 (2013)

10. Y. C. Shen, G. O. Mueller, S. Watanabe, N. F. Gardner, A. Munkholm, and M. R. Krames, Appl. Phys. Lett. **91**, 141101 (2007)

11. G. Verzellesi, D. Saguatti, M. Meneghini, F. Bertazzi, M. Goano, G. Meneghesso, and E. Zanoni, J. Appl. Phys. **114**, 071101 (2013)

12. U. Ozgur, H. Liu, X. Li, X. Ni, and H. Morkoc, Proc. of the IEEE **98**, 1180 (2010)

13. J. Iveland, L. Martinelli, J. Peretti, J. S. Speck, and C. Weisbuch, Phys. Rev. Lett. **110**, 177406 (2013)

14. D. A. Zakheim, A. S. Pavluchenko, D. A. Bauman, K. A. Bulashevich, O. V. Khokhlev, and S. Yu. Karpov, Phys. Status Solidi A **209**, 456 (2012)

15. B. Galler, P. Drechsel, R. Monnard, P. Rode, P. Stauss, S. Froehlich, W. Bergbauer, M. Binder, M. Sabathil, B. Hahn, and J. Wagner, Appl. Phys. Lett. **101**, 131111 (2012)

16. M. J. Davies, P. Dawson, S. Hammersley, T. Zhu, M. J. Kappers, C. J. Humphreys, and R. A. Oliver, Appl. Phys. Lett. **108**, 252101 (2016)

17. R. Vaxenburg, E. Lifshitz, and Al. L. Efros, Appl. Phys. Lett. **102**, 031120 (2013)

18. H. Jeong, H. J. Jeong, H. M. Oh, C.-H. Hong, E.-K.Suh, G. Lerondel and M. S. Jeong, Sci Rep **5**, 9373 (2015)

19. D. Watson-Parris, M. J. Godfrey, P. Dawson, R. A. Oliver, M. J. Galtrey, M. J. Kappers, and C. J. Humphreys, Phys. Rev. B **83**, 115321 (2011)

20. J. H. Na, R.A. Taylor, Kwan H. Lee, T. Wang, A. Tahraoui, P. Parbrook, A. Mark Fox, Sam N. Yi, Young S. Park, Jae W. Choi, and Jung S. Lee, Appl. Phys. Lett. **89**, 253120 (2006)

21. Z. Li, J. Kang, B. W. Wang, H. Li, Y. H. Weng, Y.-C. Lee, Z. Liu, X. Yi, Z. C. Feng, and G. Wang, J. Appl. Phys. **115**, 083112 (2014)

22. C.-K. Wu, C.-K. Li, and Y.R. Wu, J. Comput. Electron **14**, 416 (2015)

CHAPTER I

GENERAL PROPERTIES OF WURTZITE III-NITRIDES

In this chapter, some general structure properties and optical characteristics of the most common wurtzite III-Nitride compounds for solid states lighting: AlN, GaN, and InN and their alloys are introduced. In the wurtzite crystals, the presence of ionic charges shifts the atomic positions slightly from their ideal structures due to the long-range Coulomb interaction. The combination of the ionicity of the chemical bonds and the deformation of the bonding tetrahedron of the hexagonal crystal field affects the sign and magnitude of the spontaneous polarization in the wurtzite nitrides.

The lattice mismatch between AlN, GaN, InN, their alloys and common substrates (sapphire, SiC, Si) induces a built-in strain field in the whole structures. This generally induces the formation of dislocations and also a piezoelectric polarization across the crystal. The sum of the spontaneous polarization and the piezoelectric polarization creates two oppositive charge-planes at both sides of the wurtzite layers hence causing an internal electric field inside the layers. The consequences of this electric field are *i)* modification of the energies of electron and hole states at the origin of the red-shift of the band to band transition energy and *ii)* reduction of electron and hole wavefunction overlap. Both the high defect density and strong internal electric field negatively impact on the photoluminescence intensity of the materials via different recombination channels.

1.1. Crystalline structure

1.1.1. Crystalline structure

The wurtzite group III-nitrides are semiconductor compounds which associate nitrogen atoms (nitrogen belongs to group V of Mendeleev's table of the chemical elements) with metallic elements of the group III column; namely Al, Ga, In atoms. In this structure, each atom is coordinated by four atoms of different kind that are located at the corners of a trigonal pyramid, as illustrated in Fig. 1.1. Thus, each group-III atom (yellow sphere) is bound to four nitrogen atoms (grey spheres) and each N-atom is bound to four group-III elements.

For binary compounds, these four atoms are chemically identical while in cases of ternary, or quaternary alloys the nature of the neighbors of the nitrogen atom varies. Local fluctuations of the alloy composition from the average value are always found which lead the real properties of an alloy to depart from a statistical averaging of the properties of the binaries. For example, the composition dependence of the bandgap of an alloy is not a weighted value of the bandgap of the binary compounds: local fluctuations of the chemical composition lead to the formation of some disorder that introduces a nonlinear dependence of this bandgap. There is a bowed variation with the composition. The value of this bowing parameter may be composition-dependent, but it is always a positive quantity in nitrides.

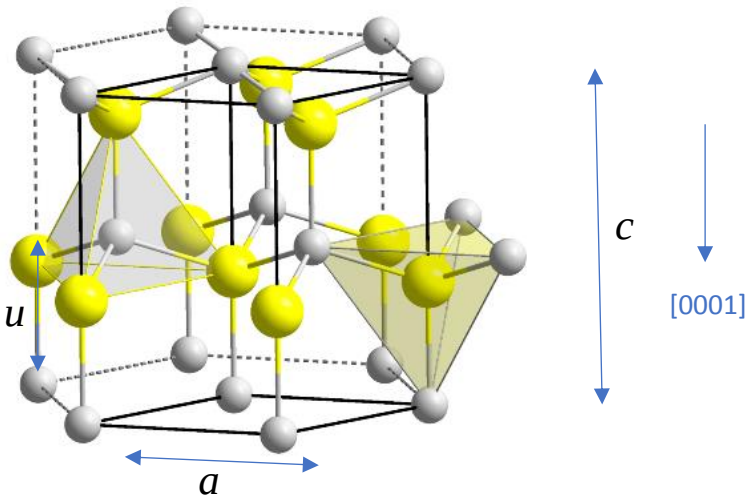

Figure 1.1. Crystalline structure of the wurtzite III-nitride compounds and its primitive unit cell, in which the yellow spheres represent for the group III-atoms (Al, Ga, In) and the grey spheres account for the nitrogen atoms.[1]

The space group of the wurtzite nitride crystals is C_{6v}^4. This structure is based on two inter-penetrating hexagonal-close-packed sub-lattices (ABABAB stacking) shifted from each other by a quantity that equals 3c/8. The structure is defined by three parameters: a unit cell height *c*, an edge length of the basal plane hexagonal *a*, and an internal parameter *u* that represents for the anion-cation bond length along the *c-direction*. In case of a stacking of atoms that are treated in terms of rigid spheres, geometrical crystallography indicates that the c/a ratio is $\sqrt{\frac{8}{3}}$ = 1.633, and u = 3/8 = 0.375, respectively.[2] We remark that these parameters are in relationship: $\frac{c}{a}.\sqrt{u} = 1$.

In the real world, the atoms cannot be approximated in terms of rigid spheres: they are species described by quantum mechanics and their properties are changed when

assembled to form molecules or crystal by interpenetrations of their electronic wavefunctions. This leads the values of c/a and u to slightly depart from their ideal values. However, some trends are roughly kept: A. Belabbes et al.[3] indicate for instance that, the *u* parameter increases if the *c/a* ratio decreases to keep the four tetrahedral distances nearly constant and then this implies a distortion of tetrahedral angles.[4]

1.1.2. Stability of the Wurtzite crystals

In the wurtzite structures, chemical bonds for a given atom with four nearest neighbors are formed by the hybridization of its sp^3 orbitals with four specific sp^3 orbitals of its four nearest neighbor atoms that oriented in the adapted directions, see Fig. 1.2(a). According to Bloch's theorem, eight valence electrons are shared through the crystal by each atomic pair. These atoms have different electronegativities. Then, the difference between the values of the screened nuclear charges of different atoms creates an asymmetry of the electronic distribution. This produces an electrostatic dipole along each orbital.

In the case of the wurtzite stacking as represented in Fig. 1.2(b) the anion-cation bond length along the *c-direction* is:

$$b = cu \tag{1.1}$$

The anion-cation bond lengths in the three other directions are:

$$b_1 = \sqrt{\frac{a^2}{3} + (1 - u^2)c^2} \tag{1.2}$$

These bonding lengths lead to formation of a trigonal pyramid with two kinds of "nearest neighbors" (coloured in white and green in Fig. 1.2(b). The unequal contributions of the four chemical bonds result in a polarization along the *c-direction*.[5] The presence of this anisotropic ionic charge, shifts the atomic positions from the ideal wurtzite structure. This simple description has however to be improved by taking into account the influences of second neighbors, third neighbors, *etc.* At the end, it can be demonstrated that the long-range Coulomb interaction is the primary cause of deviations of the lattice parameters from their ideal values, in the wurtzite crystals.[6,7]

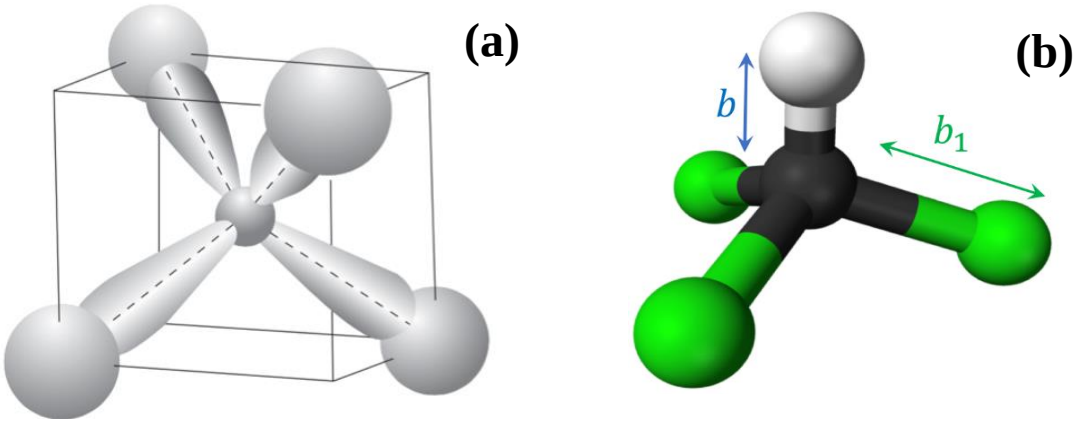

Figure 1.2. (a) The chemical bonds for a regular tetrahedron, (b) the tetrahedron form in wurtzite crystals.

As shown in Table I.1, the crystalline parameters of the wurtzite AlN, GaN, and InN compounds slightly depart from the ideal values.[4, 8] The smaller values of the ratio *c/a* compared to the ideal value (1.633) show that there is a compression along the hexagonal axis of each individual lattices. The bond lengths and the angles between bonds inside each pyramid are modified, as well as the parameter *u*. This gives rise to a dipole away from the center of each pyramid whose magnitude depends on the ionicity of the chemical bonds, and deviation of the parameter *u* from its ideal value.[2]

Table I.1: Structural parameters of hexagonal AlN, GaN, and InN crystals[4]

Material	c (A°)	a (A°)	u	c/a	$\frac{c}{a}.\sqrt{u}$
AlN	4.980	3.110	0.382	1.610	0.995
GaN	5.185	3.188	0.377	1.626	0.998
InN	5.708	3.539	0.379	1.613	0.993

1.2. Lattice mismatch and dislocations

AlN, GaN, InN compounds and their alloys are the subject of many studies due to their unique property of being able to emit light from the deep ultraviolet (UV) region to the near-infrared (NIR) one, as indicated in Fig. 1.3. However, large differences of their lattice constants can lead to severe difficulties for growing high quality heterostructures. The lack of low-cost lattice matched substrates has also long been preventing the growth of high quality material. Finding an experimental growth protocol to overcome this drawback has been tantalizing researchers during decades until it was solved by the 2014 Nobel

Prizes Akasaki, Amano, Nakamura in the mid-eighties. Still, the different III-nitrides are strongly lattice-mismatched to each other.

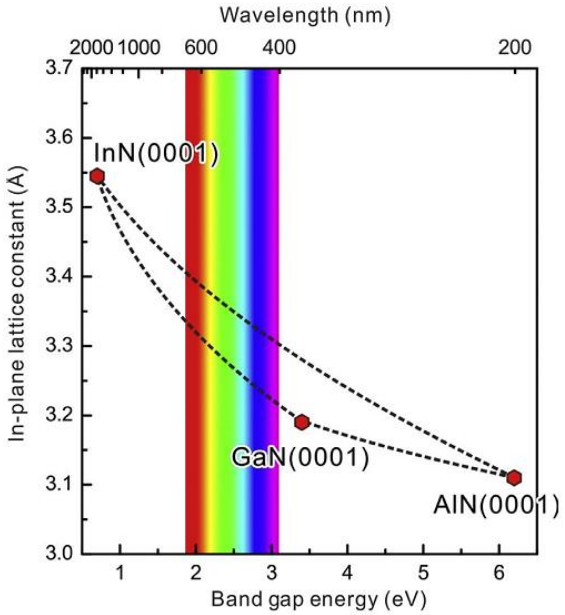

Figure 1.3: The plot of the in-plane lattice constants and bandgaps of the wurtzite AlN, GaN, and InN compounds and their alloys.[9]

Now let us consider the growth of an epitaxial layer with an in-plane lattice constant of a_l on a substrate that has an in-plane lattice constant of a_s. As described in Fig. 1.4, if $a_l = a_s$, then we have lattice-matching between the epilayer and the growth substrate. This is not the case we faced during our PhD as all our samples were grown on sapphire substrates. When a_l is larger or smaller than a_s, at initial stage of the growth process, the lattice of the grown layer is coherently strained to match the in-plane lattice parameter of the substrate. The volume density of elastic energy stored in the strained layer is given by[4]

$$W = \frac{1}{2} C_{ij} \varepsilon_i \varepsilon_j \qquad (1.3)$$

where C_{ij} represent the elastic constants, and ε_i is the strain component.

When the epitaxial layer exceeds a critical thickness, it becomes favorable to relax the stored elastic energy by the formation of extended defects such as dislocations. Note also, that the strain energy can also be relaxed by the formation of 3D islands.

If the grown layer is thin enough to keep a coherent state on the substrate, then the in-plane lattice constant of this thin layer is equal to the in-plane lattice constant of the substrate. This process is called pseudomorphic. If the value of the unstrained lattice

constant of the grown layer is larger than the lattice constant of the substrate, this layer experiences a compression in its growth plane and it is stretched in the growth direction. Alternatively, when the value of the lattice constant of the unstrained grown layer is smaller than the lattice constant of the substrate, the epilayer is stretched in its growth plane and compressed along the growth direction.

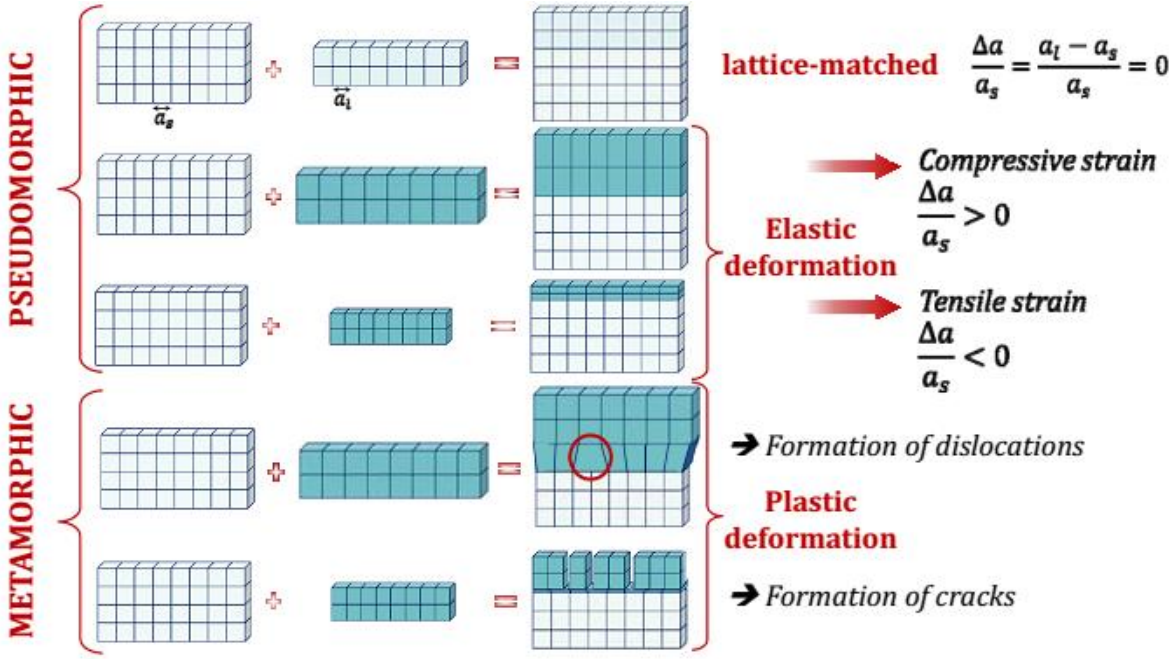

Figure 1.4: Schematic diagram of pseudomorphic growth and metamorphic growth.[10]

If the thickness of the grown layer is larger exceeds a critical value, the strain energy stored in the epilayer can relaxed by the creation of dislocations or cracks.

The final strain state of the layer will depend on the lattice mismatch with the substrate, the layer thickness and the relaxation processes involved during the growth.

1.3. Polarizations, internal electric field and quantum confined Stark effect

1.3.1. Spontaneous polarization

As reported in Fig. 1.5, in group wurtzitic III-nitride semiconductors, the atomic stacking leads to a non-overlapping of the center of gravity of positive charges and negative charges along the *c-direction*. This creates a spontaneous polarization (P_{sp}) along the *c-direction*.[4] It has been computed (and later deduced from experiments) that the spontaneous polarization, along the *c-axis* takes very large values for the III-nitride materials, as listed in the Table I.2.[3,4]

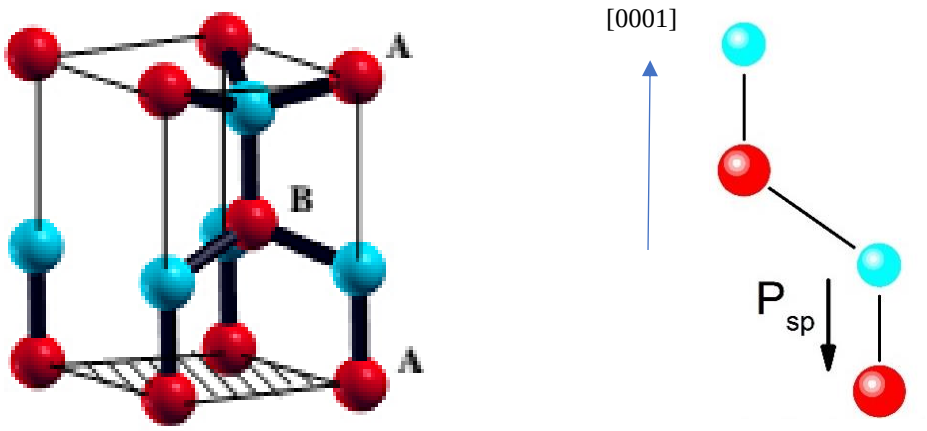

Figure 1.5: The unit cell with the ABAB… stacking of the hexagonal crystalline structures. The bonding chains along the [0001] direction of the hexagonal crystalline.[6]

The negative values of spontaneous polarization found for the wurtzite nitride crystals indicate that the electric dipole is oriented along to the -*c* direction (the $[000\bar{1}]$ direction). It is important to remind that the c-direction or [0001] direction is defined as the direction from the III-metal atoms toward the N-atom (along the polar axis). Belabbes et al.[3] demonstrated that the magnitude and the sign of the spontaneous polarization relates to the combinations of the ionicity of the chemical bonds and the deformation of the bonding tetrahedron of the hexagonal crystal field and it is of quantum origin. Large deviations of ratio c/a and of the length of u from their ideal values correspond to high polarization fields. For the group-III wurtzite nitride crystals the values of the ratio c/a are smaller than 1.633 and the value of the parameter u are larger than 0.375.[3, 8]

Table I.2. Deviations of the values of ratio c/a and of the *u* parameter from their ideal values. These values are taken from the calculations- Ref. 3 and from the experiments- Ref. 4

Material	c/a – 1.633		u – 0.375		Psp (C/m^2)	
	Ref. 3	Ref. 4	Ref. 3	Ref. 4	Ref. 3	Ref. 4
AlN	-0.0316	-0.0230	0.0049	0.0070	-0.0400	-0.0898
GaN	-0.0037	-0.0070	0.0006	0.0020	-0.0180	-0.0339
InN	-0.0167	-0.0200	0.0025	0.0040	-0.0110	-0.0413

1.3.2. Piezoelectric polarization

The combination of lattice-mismatch and different thermal expansion coefficients of the substrate and epilayers induces strains (stresses) in the epitaxial layers. Depending whether the lattice parameters of the epilayer are larger or smaller than the values of the substrate, the strains (stresses) can be compressive or tensile ones. In wurtzite crystals (the case of C_{6v} symmetry), the stress-strain relations are expressed by a 6x6 matrix:[11]

$$\begin{pmatrix}\sigma_{xx}\\ \sigma_{yy}\\ \sigma_{zz}\\ \sigma_{xy}\\ \sigma_{yz}\\ \sigma_{zx}\end{pmatrix} = \begin{pmatrix} C_{11} & C_{12} & C_{13} & 0 & 0 & 0\\ C_{12} & C_{11} & C_{13} & 0 & 0 & 0\\ C_{13} & C_{13} & C_{33} & 0 & 0 & 0\\ 0 & 0 & 0 & C_{44} & 0 & 0\\ 0 & 0 & 0 & 0 & C_{44} & 0\\ 0 & 0 & 0 & 0 & 0 & C_{66}\end{pmatrix} \begin{pmatrix}\varepsilon_{xx}\\ \varepsilon_{yy}\\ \varepsilon_{zz}\\ 2\varepsilon_{xy}\\ 2\varepsilon_{yz}\\ 2\varepsilon_{zx}\end{pmatrix} \quad (1.4)$$

where σ_{ij}, C_{ij}, and ε_{ij} are the stress elements, the elastic constants, and the strain elements.

If the hexagonal wurtzite crystal is strained in the (0001) plane and is free along the [0001] direction, the stress components are $\sigma_{xx} \neq 0$, $\sigma_{yy} \neq 0$, $\sigma_{zz} = 0$ and $\sigma_{xy} = \sigma_{yz} = \sigma_{zx} = 0$. Therefore, we have only three non-vanishing strain elements:

$$\varepsilon_{xx} = \frac{a - a_0}{a_0}, \quad \varepsilon_{yy} = \frac{b - a_0}{a_0}, \quad (1.5)$$

$$\varepsilon_{zz} = \frac{c - c_0}{c_0} = -\frac{C_{13}}{C_{33}}(\varepsilon_{xx} + \varepsilon_{yy}) \quad (1.6)$$

where a_0 and c_0 are the lattice constants of the unstrained crystal; a, b, c are the lattice constants of the strained crystal.

If the wurtzite crystal is biaxially strained in the (0001) plane, then the values of the lattice constants *a* and *b* are identical. In the case of a pseudomorphic growth, the lattice parameters *a* and *b* equal to the lattice constant of the substrate material a_{sub}. Then the strain elements are given by:

$$\varepsilon_{xx} = \varepsilon_{yy} = \frac{a_{sub} - a_0}{a_0}, \quad \varepsilon_{zz} = -\frac{2C_{13}}{C_{33}}\varepsilon_{xx} \quad (1.7)$$

Under strains, the ions slightly move from their ideal positions. Therefore, electronic charges are rearranged and accumulate toward opposite sides. Hence this creates a piezoelectric polarization across the crystal. The processes are illustrated in Fig. 1.6. The compressive strain results a piezoelectric polarization along the +*c* direction and the tensile strain results a piezoelectric polarization along the opposite direction (-*c* direction).

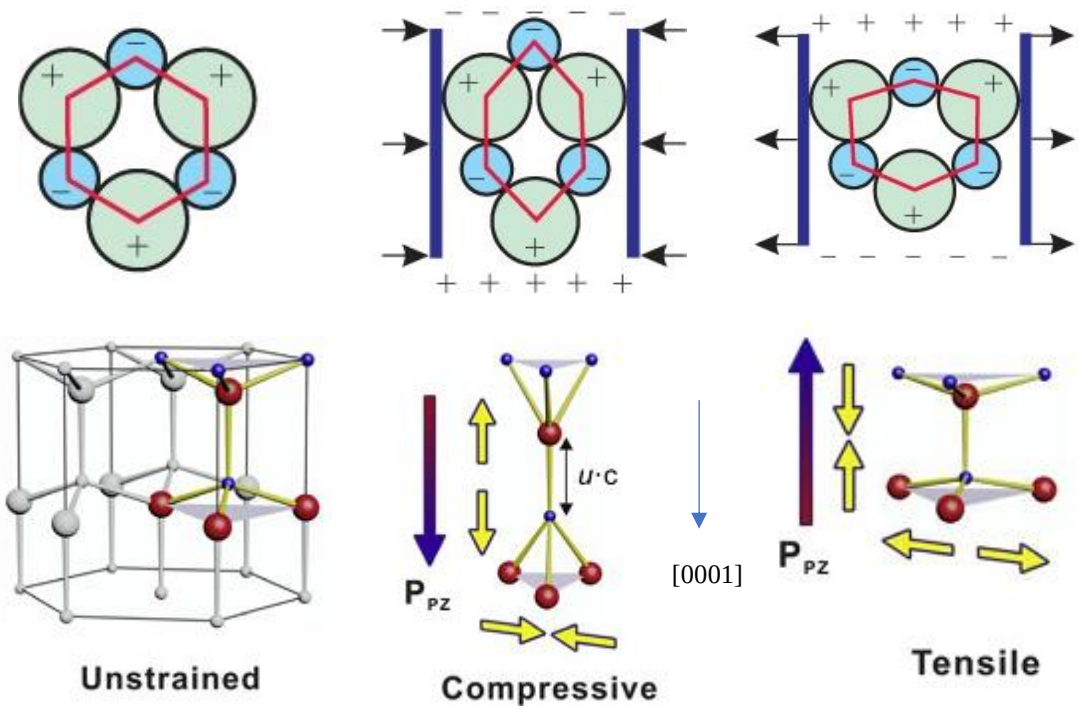

Figure 1.6: Piezoelectric polarization field in III-nitride wurtzitic crystals: the piezoelectric polarization is zero in the unstrained crystal; the piezoelectric polarization has opposite orientations under compressive and tensile strains.[9]

In the case of the strained wurtzite structure, the relation of piezoelectric polarization and the strain is determined by[4,12]

$$\begin{pmatrix} P_x \\ P_y \\ P_z \end{pmatrix} = \begin{pmatrix} 0 & 0 & 0 & 0 & 2e_{15} & 0 \\ 0 & 0 & 0 & 2e_{15} & 0 & 0 \\ e_{31} & e_{31} & e_{33} & 0 & 0 & 0 \end{pmatrix} \begin{pmatrix} \varepsilon_{xx} \\ \varepsilon_{yy} \\ \varepsilon_{zz} \\ \varepsilon_{yz} \\ \varepsilon_{zx} \\ \varepsilon_{xy} \end{pmatrix} \tag{1.8}$$

where P_i represent the components of the piezoelectric polarizations, e_{ij} and ε_{ij} are the components of the piezoelectric tensor, the strain tensor components.

In the case of a growth along the polar direction, the values of the components of the built-in strain are:

$$\varepsilon_{yz} = \varepsilon_{zx} = \varepsilon_{xy} = 0 \tag{1.9}$$

and ε_{xx}, ε_{yy}, and ε_{zz} as determined earlier by Eq. (1.7)

Then, the piezoelectric polarization for strained III-nitride epitaxial layers is given by:

$$P_z = e_{31}\varepsilon_{xx} + e_{31}\varepsilon_{yy} + e_{33}\varepsilon_{zz} \tag{1.10}$$

$$P_z = 2\left(e_{31} - \frac{C_{13}}{C_{33}}\right)\varepsilon_{xx} \qquad (1.11)$$

where the values of the components of the piezoelectric tensor are listed in the Table I.3.

Table I.3. Values of the components of the piezoelectric tensor for wurtzite AlN, GaN, and InN[4]

Material	e_{13} (Cm^{-2})	e_{33} (Cm^{-2})	e_{15} (Cm^{-2})
AlN	-0.533	-0.623	-0.351
GaN	-0.338	-0.372	-0.167
InN	-0.413	-0.454	-0.112

1.3.3. Internal electric field

As mentioned earlier, in the wurtzite crystals, the spontaneous polarization is oriented along the -*c* direction. The direction of the piezoelectric polarization depends on the strain field. It has the -*c* direction in case of AlGaN layers that are tensily strained on GaN layers while it has +*c* direction in the case of InGaN layers that are compressively strained on GaN layers, as shown in Fig. 1.7.[13] The total polarization is the sum of the spontaneous polarization and the piezo-polarization given as: $P = P_{sp} + P_{pz}$ also oriented along the *c-direction.*

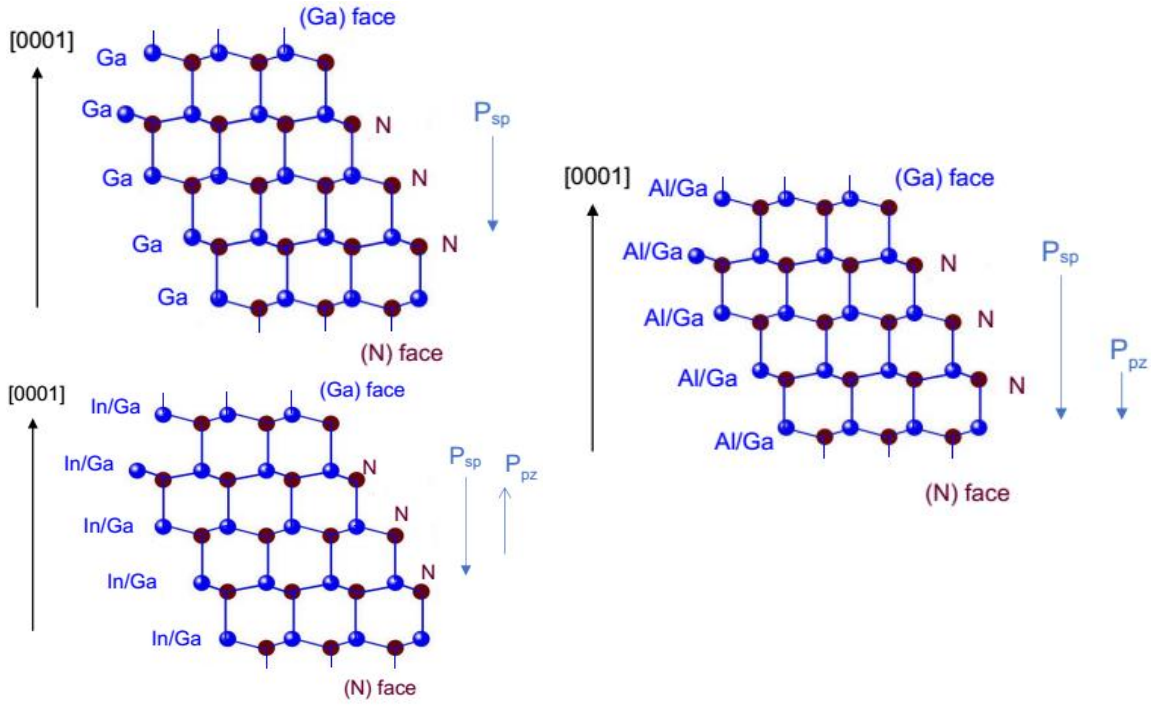

Figure 1.7**:** The polarizations of GaN layer, and of AlGaN and InGaN coherently strained to GaN.[4, 13]

The polarization field forms two charge planes at both sides of the wurtzite layer: one has a positive charge and the other one has a negative charge Fig. 1.8. The densities of charges at interfaces are determined by[4, 14]

$$\sigma = \vec{P} \,.\, \vec{n} \tag{1.12}$$

where $\vec{n}$ is the unity vector normal of the semiconductor surfaces

The difference of charge densities at the interfaces results in an internal electric field inside the layer. To determine the value of this electric field E, let us start by a simple structure as a thin InGaN layer embedded into two thick layers of GaN (InGaN/GaN single quantum well), as shown in Fig. 1.8. The P_W, P_B, L_W, and L_B are labeled as total polarizations, thicknesses of the InGaN and the GaN layers, respectively. Then, the surface charge density is written as:

$$\sigma_{W-B} = \left[\vec{P}_W - \vec{P}_B\right] . \vec{n} \tag{1.13}$$

The conservation of the electric displacement vector $\vec{D}$ through the interface leads to:

$$\left[\vec{D}_W - \vec{D}_B\right] . \vec{n} = \left[\epsilon_W \vec{E}_W - \epsilon_B \vec{E}_B\right] . \vec{n} = \left[\vec{P}_B - \vec{P}_W\right] . \vec{n} \tag{1.14}$$

In which the electric field $\vec{E}$ relates to the displacement vector $\vec{D}$ by $\overrightarrow{D_i} = \epsilon_i \vec{E}_i$; ϵ_i is the dielectric constant of the material.

To calculate the electric field, it is generally assumed that there is no potential drop through the whole heterostructure, this can be written as:

$$\vec{E}_W \,.\vec{n}\, L_W + \vec{E}_B \,.\vec{n}\, L_B = 0 \tag{1.15}$$

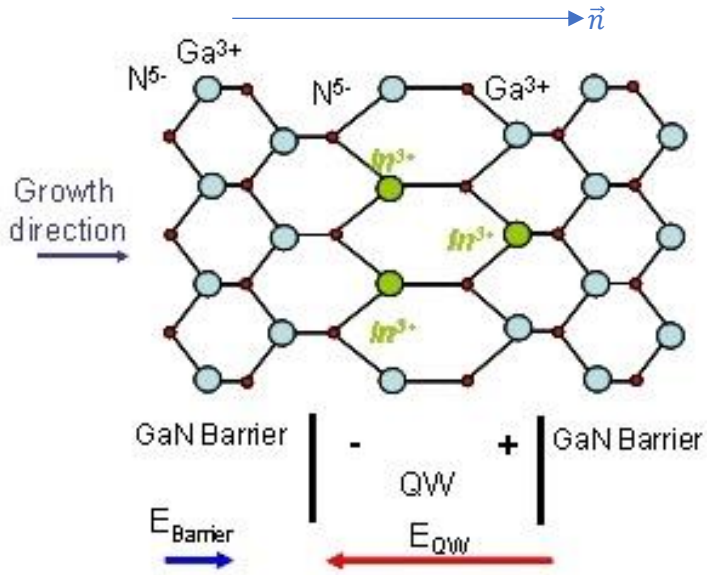

Figure 1.8**:** The internal electric field in a InGaN/GaN heterostructure.[15]

After combining the Eq. 1.14 and Eq. 1.15, the internal electric fields are given by:

$$\vec{E}_W \,.\vec{n} = \frac{L_B}{\epsilon_W L_B + \epsilon_B L_W} \left[\vec{P}_B - \vec{P}_W \right] . \vec{n} \quad (1.16)$$

$$\vec{E}_B \,.\vec{n} = -\frac{L_W}{\epsilon_W L_B + \epsilon_B L_W} \left[\vec{P}_B - \vec{P}_W \right] . \vec{n} \quad (1.17)$$

These equations show that the values of the internal electric fields not only depend on the strength of the polarization but also depend on the thickness of the different layers. In addition, the values of the internal electric fields vary with the orientations of the crystal. This electric field has the highest value if the structure is grown along the *c-direction* (the [0001] direction). In this case, the crystals are called polar oriented structures. The electric field vanishes in the direction perpendicular to the *c-direction*. Then, the crystals are called non-polar oriented structures. For other cases, the crystals are called semi-polar oriented structures.

If we assume that the structures are grown along the c-direction (or semi-polar-direction) and the strain field is constant, the internal electric field can be approximated by a linear (or sub-linear) relationship with alloy composition.[16]

1.3.4. Quantum confined Stark effect

In the absence of the internal electric field (square well), both the electron and hole wave-functions have a maximum located at the center of well layer, as illustrated in Fig. 1.9. It leads to a large overlapping of wavefunctions and to a good oscillator strength for band to band recombination processes with an energy that is expressed by:

$$E = E_g + E_e + E_h - E_b \quad (1.18)$$

where E_g is the bandgap of quantum well material; E_e and E_h are the confinement energies of electron and hole, respectively, and E_b is the exciton binding energy.

When the internal electric field is considered, the band structure is modified and in particular a triangular well potential appears. In this case, the electron states are shifted to lower energies, while hole states are shifted to higher energies. The band to band transition energy of the heterostructure is modified by a potential drop (about eL_wF_w) and can be determined by:

$$E = E_g + E_e + E_h - E_b - eL_wF_w \quad (1.19)$$

in which e, L_w, and F_w are the elemental charge, the QW width, and the electric field value in the QW layer.

The presence of the internal electric field induces a red-shift of the PL energy transitions in heterostructures, such as InGaN/GaN, GaN/AlGaN grown along the polar orientation. The red-shift increases with the the thickness of the QW and with the internal electric field. This is a manifestation of the quantum confined Stark effect (QCSE).

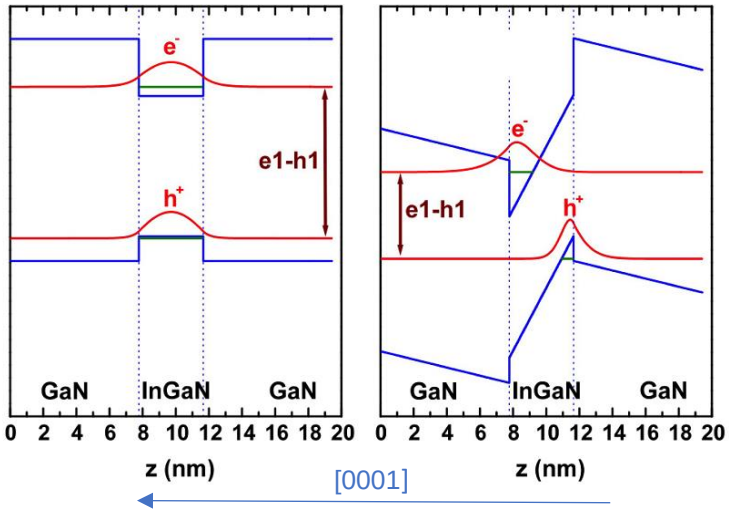

Figure 1.9. Schematic diagram impact of Quantum Confined Stark effect.[4]

Under the impact of the internal electric field, the electron and hole are pulled apart to opposite sides of the interfaces; hence the overlap of their wave-functions is reduced. This directly affects the radiative decay time of carriers in the two dimensional (2D) heterostructures. Using a 2D trial function, the radiative decay time of carriers in a quantum well is proportional to the invert of the integrated overlap of the envelop functions of the confined electron and hole :[1]

$$\tau_R \approx \frac{1}{|\int \chi_e(x)\chi_h(x)dx|^2} \qquad (1.20)$$

where λ is the in-plane Bohr radius; χ_e and χ_h are the envelop functions of the confined electron and hole.

As reported in Fig. 1.10(a) for the case of GaN/AlGaN QW, both increasing the Al content and increasing the QW width reduce the overlap of the wave-functions of electron and hole. Consequently, this induces an increase of the PL decay time of the carriers and reduces the PL intensity. It is found that the decay time increases very fast with increasing QW width, as indicated in Fig. 1.10(b), when the QW width increases from 3 monolayers (MLs) to 15 MLs. This is another manifestation of the QCSE.

In polar-oriented structures, the QCSE induces a red-shift of the PL transition energies and an increase of the radiative PL decay times.

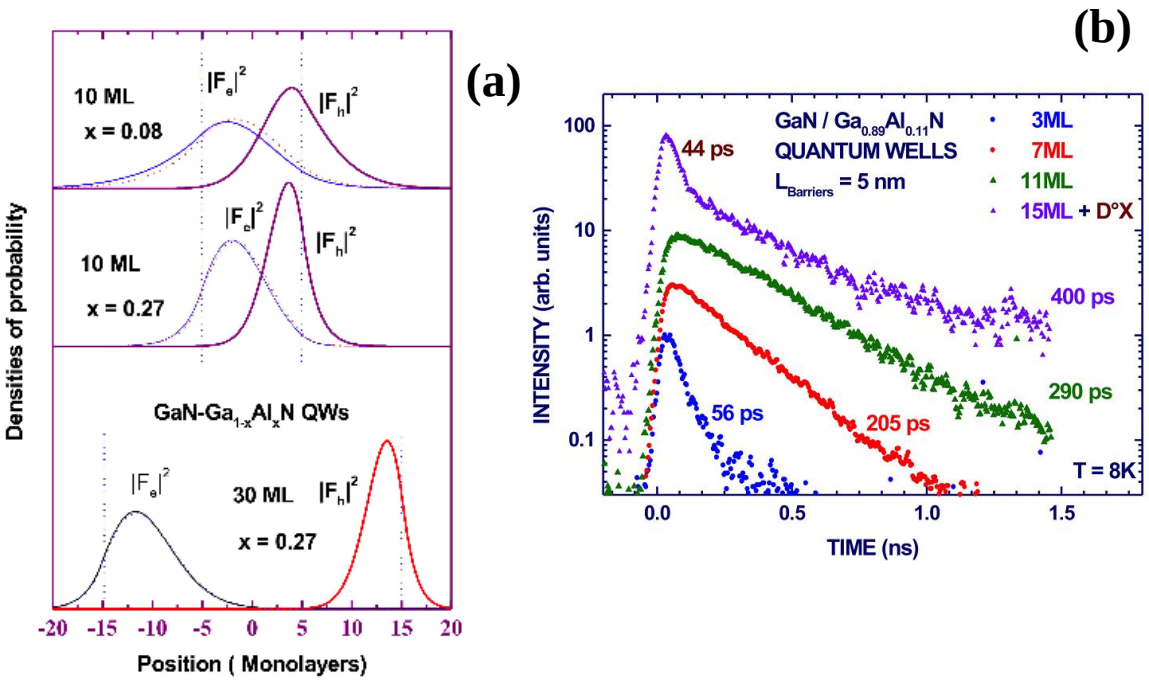

Figure 1.10: (a) Overlap of electron and hole wavefunctions with changing of the alloy composition and QW width in case of GaN/AlGaN QWs.[4] (b) Evolution of the photoluminescence decay time when the GaN QW thickness increases from 3 monolayers to 15 monolayers.[4]

1.4. Recombination processes and internal quantum efficiency

We describe in this section the main recombination processes that occur in photoexcited semiconductors. When semiconductor materials are excited by photons with an energy larger than their bandgap, highly energetic electron-hole pairs are generated. Then, the electron-hole pairs relax their energy and then can either recombine radiatively to produce light or they can recombine non-radiatively. The internal quantum efficiency (IQE) is defined as the proportion of the radiative recombination rate to the generation rate of photoexcited carriers.

Figure 1.11 reports three basic recombination processes that are usually considered in a semiconductor: i) the Shockley-Read-Hall non-radiative recombination; ii) the band-to-band radiative recombination; iii) the Auger non-radiative recombination. The competition of radiative and non-radiative recombination processes directly impacts the IQE. The details of these processes are discussed in the following.

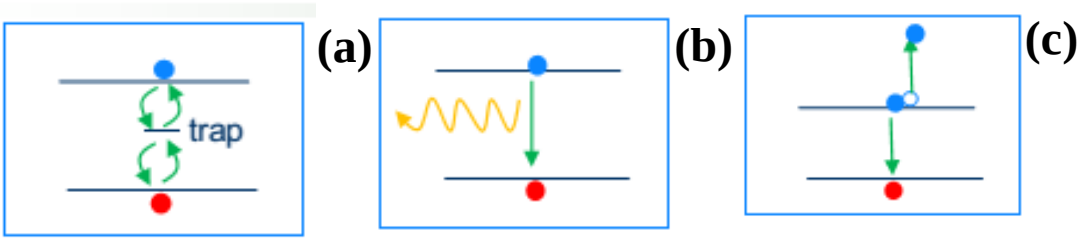

Figure 1.11: (a) The Shockley-Read-Hall non-radiative recombination; (b) the band-to-band radiative recombination; (c) the nnp-Auger non-radiative recombination.

1.4.1. The Shockley-Read-Hall non-radiative recombination

The Shockley-Read-Hall (SRH) process is a non-radiative recombination implying defects. In this process, electrons are captured by trap states at which they recombine with holes in the valence band. When electron and hole recombine, their energy is released to phonon vibration of the lattice instead of producing visible light.

The SRH non-radiative recombination rates for electron and hole through trap states located at energy E_t with concentration N_t are expressed as:

$$R_{SRH}(n) = R_{SRH}(p) = \frac{p_0\Delta n + n_0\Delta p + \Delta n\Delta p}{\tau_{p0}(n_0+\Delta n + n_1) + \tau_{n0}(p_0+\Delta p + p_1)} \quad (1.21)$$

The parameters in the Eq. (1.21) are defined as follows:

- n_0 and Δn are equilibrium electron and the excess electron densities
- p_0 and Δp are equilibrium hole and the excess hole densities
  in which $n_0p_0 = n_i^2$; n_i is the intrinsic carrier density
- τ_{p0} and τ_{n0} are the minority hole lifetime for an n-type semiconductor and the minority electron lifetime for a p-type semiconductor expressed by

  $$\tau_{p0} = \frac{1}{\sigma_p \vartheta_{th} N_t} \quad (1.22)$$

  $$\tau_{n0} = \frac{1}{\sigma_n \vartheta_{th} N_t} \quad (1.23)$$

  In which σ_p, and σ_n are the hole and the electron capture cross section; υ_{th} is the thermal velocity of electron and hole.
- n_1 and p_1 are the electron and hole densities if the Fermi energy E_f is located at the trap level. These quantities are given by:

  $$n_1 = n_0 \exp\left(\frac{E_t - E_f}{k_B T}\right) \quad (1.24)$$

  $$p_1 = p_0 \exp\left(\frac{E_f - E_t}{k_B T}\right) \quad (1.25)$$

The non-radiative SRH lifetime of excess electron and of excess hole are determined by:

$$\tau_{SRH} = \frac{\Delta n}{R_{SRH}(n)} = \frac{\Delta p}{R_{SRH}(p)} = \frac{\tau_{p0}(n_0+\Delta n + n_1)}{(n_0+ p_0+\Delta n)} + \frac{\tau_{n0}(p_0+\Delta p + p_1)}{(n_0+ p_0+\Delta p)} \quad (1.26)$$

Under low injection conditions $\Delta n << n_0$ and $\Delta p << p_0$, the non-radiative SRH lifetime of excess carrier is given by

$$\tau_{SRH(low)} = \frac{\tau_{p0}(n_0 + n_1)}{(n_0+ p_0)} + \frac{\tau_{n0}(p_0 + p_1)}{(n_0+ p_0)} \quad (1.27)$$

For the case of ***n-type*** semiconductor, $n_0 » n_1$, p_0 and p_1 then

$$\tau_{SRH(low)} = \tau_{p0} = \frac{1}{\sigma_p \vartheta_{th} N_t} \quad (1.28)$$

For the case of ***p-type*** semiconductor, $p_0 >> p_1$, n_0 and n_1 then

$$\tau_{SRH(low)} = \tau_{n0} = \frac{1}{\sigma_n \vartheta_{th} N_t} \quad (1.29)$$

The Eq. (1.28) and Eq. (1.29) indicate that in doped-semiconductors, the SRH lifetime of excess carrier is dominated by the minority carrier lifetime, at low injection level. These equations also show that the SRH lifetime of excess carriers is limited by the capture rate of minority carriers. This parameter is related to the quality of the structures. A high-quality structure with small defects density has a long minority carrier lifetime and therefore a low non-radiative SRH recombination rate.

Under high injection conditions $\Delta n = \Delta p >> n_0$, p_0, n_1, and p_1, the non-radiative SRH lifetime of excess carriers in the Eq. (25) can be given by

$$\tau_{SRH(high)} = \tau_{p0} + \tau_{n0} \quad (1.30)$$

The Eq. (1.30) shows that at high injection level, SRH lifetime of excess carriers is limited by the sum of the lifetimes of minority carriers.

1.4.2. The band-to-band radiative recombination

The diagram of the band-to-band radiative recombination in bulk is schematized in Fig. 1.12. The rate of the radiative recombination of electron and hole to produce photon is proportional to the density of electrons in the conduction band and the density of holes in the valence band. Therefore, the radiative recombination rate can be written as

$$R_{rad} = B(n_0 + \Delta n)(p_0 + \Delta p) = Bn_0p_0 + B(p_0\Delta n + n_0\Delta p + \Delta n\Delta p) \quad (1.31)$$

$$R_{rad} = R_0 + R_{excess} \quad (1.32)$$

In which:

- the constant B is the radiative (bimolecular) recombination coefficient.
- $G_0 = R_0 = \mathrm{Bn_0p_0}$ are the generation rate and recombination rate of carrier at thermal equilibrium
- $R_{excess} = B(p_0\Delta n + n_0\Delta p + \Delta n\Delta p)$ is the recombination rate resulting from photon excitation

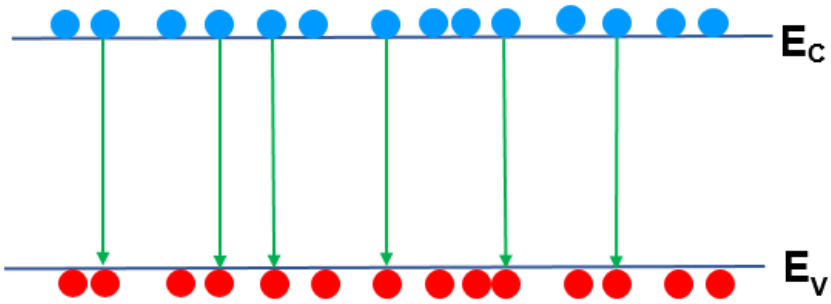

Figure 1.12: Diagram of the band-to-band radiative recombination.[17]

The time dependence of the carrier density can be determined by:

$$\frac{d\Delta n(t)}{dt} = G - R_{rad} = (G_0 + G_{excess}) - (R_0 + R_{excess}) \quad (1.33)$$

$$\frac{d\Delta n(t)}{dt} = (G_0 + G_{excess}) - R_0 - B(p_0\Delta n + n_0\Delta p + \Delta n\Delta p) \quad (1.34)$$

It is accepted that under the steady-state, electron and hole are generated and annihilated in pairs. It means that the densities of excess electrons and holes are always equal

$$\Delta n(t) = \Delta p(t) \quad (1.35)$$

At the time t = 0 and at the thermal equilibrium: $G_{excess} = 0$ and $G_0 = R_0$, then the Eq. (1.34) can be rewritten as

$$\frac{d\Delta n(t)}{dt} = -B(p_0 + n_0 + \Delta n)\,\Delta n(t) \quad (1.36)$$

Under low excitation condition, n_0 and p_0 » Δn, the Eq. (1.36) becomes

$$\frac{d\Delta n(t)}{dt} = -B(p_0 + n_0)\,\Delta n(t) \quad (1.37)$$

Solving the Eq. (1.37) gives

$$\Delta n(t) = \Delta n(0)\exp(-B(p_0 + n_0)t) = \Delta n(0)\exp(-t/\tau) \quad (1.38)$$

In which τ is defined as the radiative carrier life time that is given by

$$\tau_{rad} = -\frac{1}{B(p_0 + n_0)} \quad (1.39)$$

1.4.3. Auger non-radiative recombination

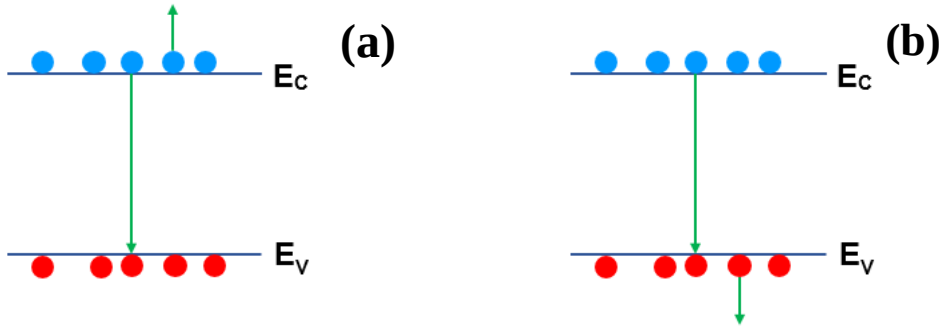

Figure 1.13: Diagram of the band-to-band Auger non-radiative recombination: (a) the nnp Auger process, (b) the npp Auger process

The mechanism of the basic Auger non-radiative recombination: nnp-Auger process and npp-Auger process are reported in Fig. 1.13. These processes occur under condition of carrier collisions. The nnp (npp) -Auger recombination happens when electron-hole pairs recombine and the corresponding energy is transferred to another electron (hole). The rate of this recombination process under non-equilibrium conditions can be expressed as

$$R_{Auger} = C_n(\mathrm{n_0} + \Delta\mathrm{n})^2(\mathrm{p_0} + \Delta\mathrm{p}) + C_p(\mathrm{n_0} + \Delta\mathrm{n})(p_0 + \Delta\mathrm{p})^2 \quad (1.40)$$

where C_n and C_p are the nnp-Auger recombination coefficient and the npp-Auger recombination coefficient.

The Auger non-radiative recombination processes have been demonstrated to be the dominating recombination channel at high injection level. This causes the reduction of the internal quantum efficiency with increasing the injection carrier density.

1.4.4. Internal quantum efficiency

The internal quantum efficiency (IQE) is determined by the proportion of the radiative recombination rate to the generation rate of carrier in semiconductors. The generation rate is equal to the total recombination rates including radiative and non-radiative recombination channels. Then the IQE can be calculated by

$$IQE = \frac{R_{rad}}{R_{rad} + R_{non-rad}} = \frac{R_{rad}}{R_{rad} + R_{SRH} + R_{Auger}} \quad (1.41)$$

To get efficient light-emitting devices, it is important to maximize the IQE. The value of IQE directly relates to the crystalline quality of the structure, under low photo-excitation conditions, that is to say when non-radiative Auger recombination processes are negligible, high-quality structure has high value of IQE thanks to small SRH non-radiative

recombination rate and high radiative recombination rate. Therefore, improving the crystalline quality is the first key to enhance value of the IQE.

Under high excitation condition, the Auger recombination process plays an important role in the evolution of the IQE with excitation carrier density. As discussed above, the Auger recombination rate is proportional to the cubic of the carrier density. Therefore, this term dramatically increases, at high injection level.

1.5. Phase space filling effects

In a QW, the motions of carriers (electron and hole) are quantized along the z-direction, and these carriers only move freely along the x and y directions. The kinetic energies of electron and hole are quantized along the z-direction, as indicated in Fig. 1.14(a). The 2-dimentions (2D) density of states at a given quantized energy E_n depends on the number of different wave vector k_z states at that energy,[18] and it exhibits discontinuities for different quantized energy E_n, see Fig. 1.14(b).

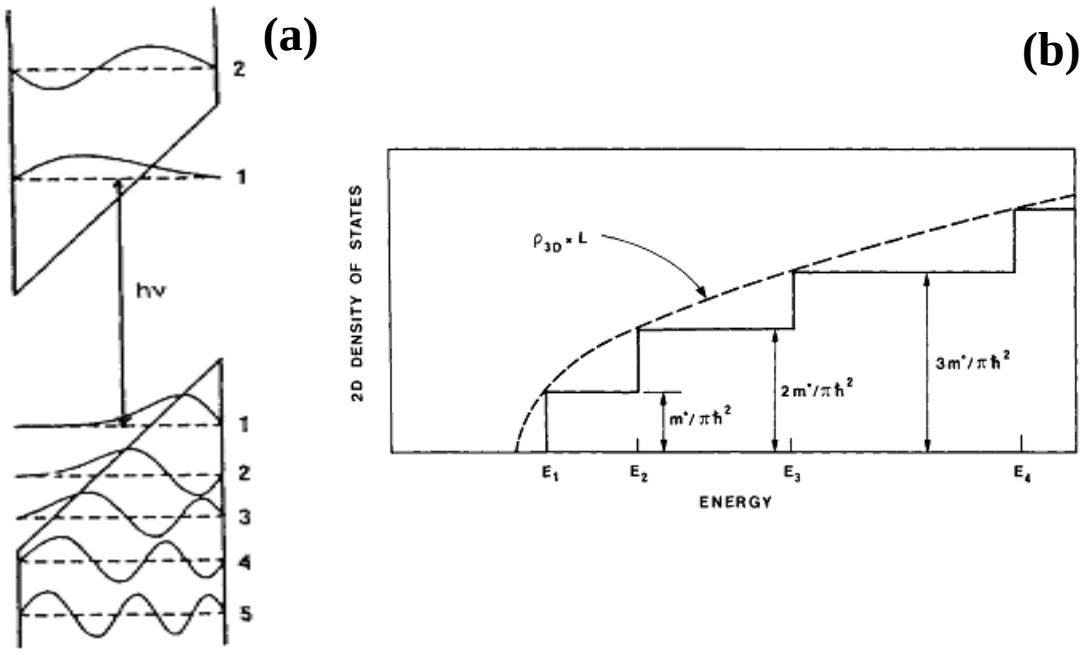

Figure 1.14 (a) Quantization energies of electron and hole and their wavefunctions in a quantum well with triangular potential. (b) 2D density of states in comparison with the density of sates of 3D case.[17]

When electron-hole pairs are injected in the QW, states at the lowest energy of conduction band and the highest energy of valence band are occupied first. If the injection carrier density goes further higher, all sates at low energy are occupied, then electrons and

holes can fill in states at higher energy. Under this condition, because of the Pauli exclusion principle, only states at higher energy are allowed to participate in the wave-functions of electron and hole corresponding to their motion in the x and y directions.[19-21] This phenomenon is called the phase-space filling (PSF) effect. This effect is a blocking mechanism in which the states are not changed, only the transitions are forbidden.[19] Under high injection carrier density, the PSF causes a reduction of the exciton binding energy[21] and a decrease of the oscillator strength due to the increase of the dielectric constant with carrier density.[20] Under this condition, interaction of electron-hole pairs with a third carrier (electron or hole) becomes highly probable and then it favors the Auger non-radiative recombination processes.

References

1. https://de.wikipedia.org/wiki/Zinksulfid
2. G. A. Jeffrey, G. S. Parry, and R. L. Mozz, J. Chem. Phys. **25**, 1024 (1956)
3. A. Belabbes, J. Furthmuller, and F. Bechstedt, Phys. Rev. B **87**, 035305 (2013)
4. B. Gil, "Physics of Wurtzite Nitrides and Oxides: Passport to Devices", Springer International Publishing AG, Springer Series in Material Science, Vol. **197**, Switzerland (2014)
5. F. Keffer and A. M. Portis, J. Chem. Phys. **27**, 675 (1957)
6. S. Datta, T. Saha-Dasgupta, and D. D. Sarma, J. Phys.: Condens. Matter **20**, 445217 (2008)
7. P. Lawaetz, Phys. Rev. B **5**, 4039 (1972);
8. F. Bernardini, V. Fiorentini, and D. Vanderbilt, Phys. Rev. B **56**, R10024 (1997)
9. III-Nitride Semiconductor Optoelectronics, edited by Z. Mi and C. Jagadish, Academic Press, Cambridge, 2017
10. N. Grandjean, Lecture on epitaxial growth in GaNex winter school, 2017
11. Group III-Nitride Semiconductors, edited by B. Gil, P316
12. T. Takeuchi, S. Sota, M. Katsuragawa, M. Komori, H. Takeuchi, H Amano and I. Akasaki, Jpn. J. Appl. Phys. **36**, L382 (1997)

13. E. T. Yu, X. Z. Dang, P. M. Asbeck, S. S. Lau, and G. J. Sullivan, J. Vac. Sci. Technol. B **17**, 1742 (1999)
14. D. Vanderbilt, R. D. King-Smith, Phys. Rev. B **48**, 4442 (1993)
15. http://www2.mpipmainz.mpg.de/groups/bonn/research/turchinovich_dmitry/ultrafast_photonics
16. Yoichi Kawakami, Low-dimensional nitride semiconductors edited by Bernard Gil, Oxford university press 2002, p235
17. E. Fred Schubert, Light Emitting Diodes, 2nd edition, Cambridge university press (2007)
18. C. Weisbuch, Quantum Semiconductors structures, Academic Press, 1991, P89
19. S. Schmitt-Rink, D. S. Chemla, and D. A. B. Miller, Phys. Rev. B **32**, 6601, (1985)
20. D. Huang, J.-Inn Chyi, and H. Morkog, Phys. Rev. B **42**, 5147 (1990)
21. P. Bigenwald, A. Kavokin, B. Gil and P. Lefebvre, Phys. Rev. B **61**, 15621 (2000)

CHAPTER II

InGaN/GaN QUANTUM WELLS FOR GREEN-YELLOW AND LONGER WAVELENGTH EMISSION

The highest efficiency InGaN-based light-emitting diodes (LEDs) has been found for the blue region of the visible light. The values of the external quantum efficiency (EQE) becomes lower and lower when the emission wavelengths shift toward green, then yellow and finally red regions. Red emission with high efficiency can be obtained by using phosphor-based materials. However, the efficiency of this kind of materials also strongly reduces in the yellow and green regions, the blue one being out of the capabilities of this technology for fundamental reasons (values of the bandgaps of phosphides). Figure 2.1 shows the reduction of the EQE for some of the different commercially used materials. The region of wavelength for the collapse of LEDs efficiencies whatever the technology is used is well-known as the "green-gap" technological problem.[1]

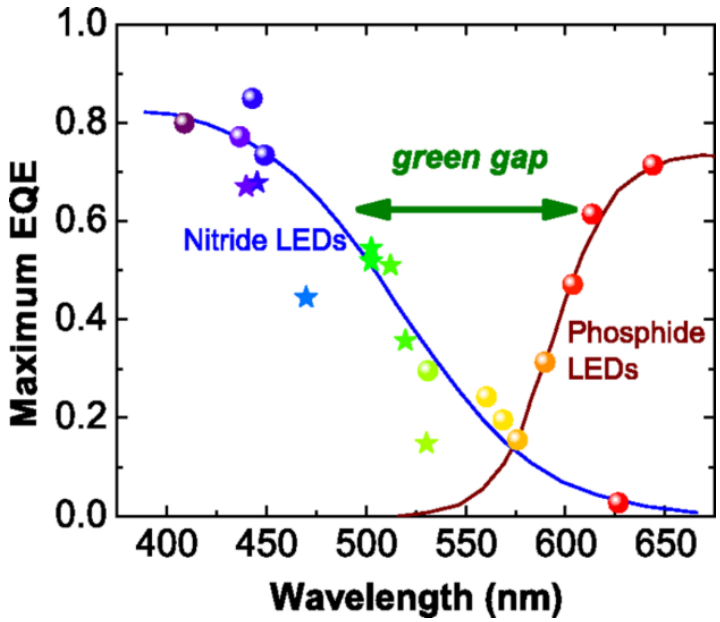

Figure 2.1. The maximum of external quantum efficiency (EQE) of nitride and phosphide LEDs.[1]

The ternary compound $In_xGa_{1-x}N$ can be interpreted in terms of a mixing of the two binary materials GaN and InN with respective bandgaps sitting in near-ultraviolet (NUV) and near-infrared (NIR), respectively. The bandgap of $In_xGa_{1-x}N$ alloy can be determined by using the composition dependence law:[2]

$$Eg(In_xGa_{1-x}N) = x\ Eg(InN) + (1-x)\ Eg(GaN) - b\ x\ (1-x) \quad (2.1)$$

where b is the bowing parameter which does not vanish because of the disordered distribution of Ga and In atoms in the metallic sub-lattices

Thus, the emission light of the (In,Ga)N alloy is continuously tunable and it can cover the whole range of wavelengths of visible light, as shown in Fig.2.2, by just changing the relative proportions of Ga and In. This offers a large range of potential applications for this material in the solid-state lighting. However, the growth of a high quality InGaN/GaN-based device faces many difficulties, especially for the green light and longer emission wavelength: as such structures require dealing with high indium content in the active region of the device. Growing such alloys with a high crystalline quality is really an issue.

2.1. Challenge of growth InGaN-based LEDs

The most common light emitting devices based on InGaN/GaN QWs are grown on a c-plane substrate. In such case the internal electric field in the QWs is higher compared to growths along other orientations.[3] This internal electric field induces a spatial separation of the electron and hole wave-functions, leading to a reduction of the light emission efficiency. This effect of the electric field in combination with a reduced crystalline quality for high indium composition are the main origins of the "green-gap".[1,4,5]

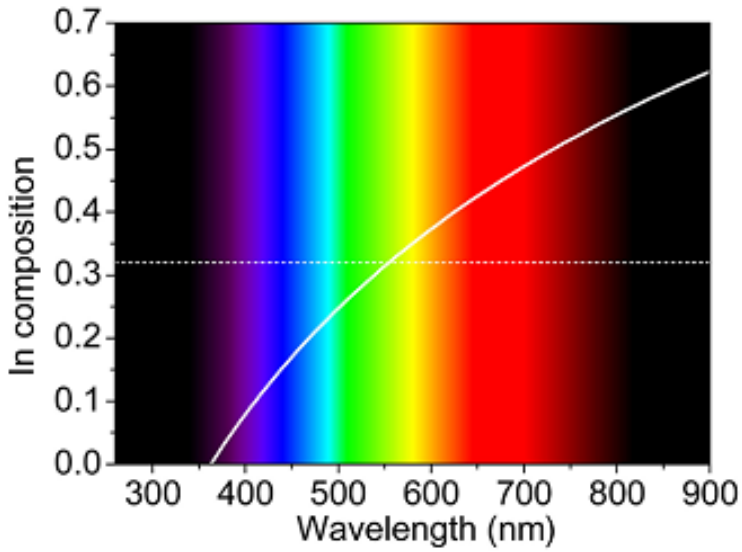

Figure 2.2. Correspondence between the indium content of $In_xGa_{1-x}N$ and the emission wavelength.[2]

In general, growing a green-yellow light emitting diode based InGaN/GaN QWs requires a higher indium composition than growing a blue does. This requires a reduction

of the growth temperature of the QW layers. This step leads to a lower crystalline quality due to defect formation (point defects, extended defects), and also in some cases of phase separation. It is also important to note that the lattice mismatch between GaN and InN is very large (>10%) which can be at the origin of plastic stress relaxation for high In InGaN layers grown on GaN. A high indium composition also increases the internal electric field inside the InGaN QWs in correlation with the contrast of spontaneous and piezoelectric polarizations across the different interfaces. This causes a reduction of the overlap of the wave-functions of the electron and hole and leads to low radiative recombination rates. Using lower-indium InGaN QW layers but very wide QW could be an alternate option. Unfortunately, the QCSE is then so strong that it causes for a given emission wavelength, a dramatic enhancement of the radiative decay time than using high indium content and thin well do. So, one has to juggle with the impact of both indium composition and thickness of the well layer together with growth challenges for selecting the best design for an efficient light emission.

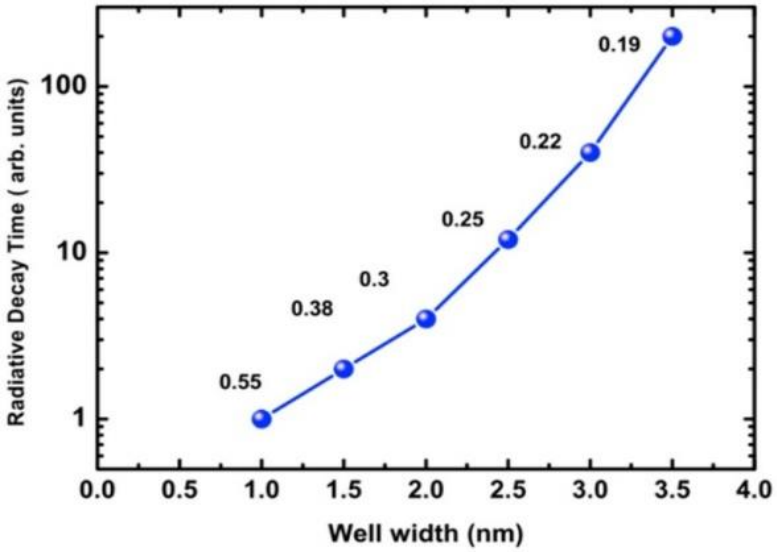

Figure 2.3. Calculated radiative decay times of InGaN/GaN quantum wells versus quantum well thickness and In composition for a green light emitting at 540 nm.[6,7]

Figure 2.3 shows the calculated radiative decay time of InGaN/GaN MQWs emitting at 540 nm versus different well widths and In compositions.[6,7] Shorter radiative decay times are computed for samples having high In content and thin quantum well. Then in this case, the radiative recombination rate is higher than in other ones and the light emission efficiency is enhanced (the impact of the QCSE is minimized). Therefore, the solution for high efficiency green-yellow light emitter structures based on indium-rich (In,Ga)N quantum well together with thin QWs. However, in indium-rich regions, the

relative sizes of nitrogen and indium generate huge inhomogeneous strain-fields which favour spinodal decompositions of InGaN, and leads to strong disorder in the quantum wells and rough interfaces with the barriers.[8-10]

2.2. Localization effect in the InGaN/GaN quantum wells

In the InGaN ternary alloy, the N-atoms and In-Ga-atoms form pyramids centered around the N atoms with randomly ordering of the In atoms and Ga-atoms in the crystal,[8] as illustrated in Fig. 2.4 (a).[11] Then, it induces distortions of the pyramid in the wurtzite structure. These distortions depend on the composition of the InGaN alloy, and are correlated in a quite complex manner with the difference in elastic constants of InN and GaN binary compounds.[8] Moreover, the strain energy at the scale of the whole structure modifies the equilibrium bond lengths between the first nearest-neighbor atoms. Therefore, it increases the distortion of the pyramid from the ideal structure, which results in strong immiscibility through the whole range of compositions of the (In,Ga)N alloys[12] and hence, it induces local fluctuations of the In composition, as shown in Fig. 2.4 (b).[1]

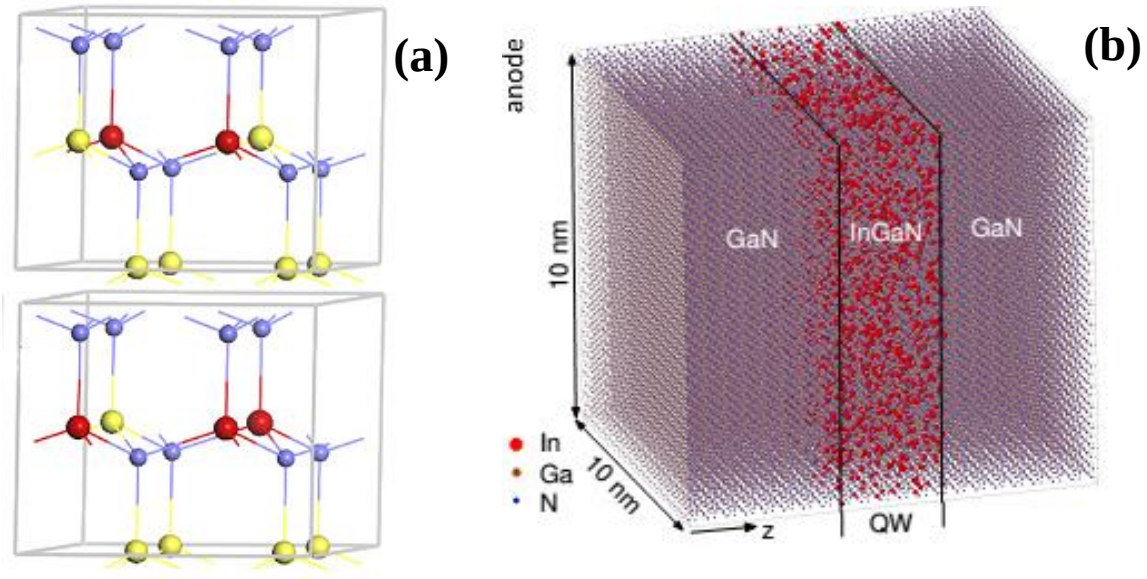

Figure 2.4: (a) Sketch of different In configurations in InGaN supercell geometry. The red, yellow and blue spheres are In, Ga, and N atoms, respectively.[11] (b) Random position of the In, Ga, and N atoms in InGaN/GaN quantum wells.[1]

The spatial fluctuations of the alloy composition induce carrier localization in InGaN/GaN hetorostructures,[13] which is amplified by the presence of the internal electric field, as illustrated in Fig. 2.5. The spontaneous polarization and the piezo-polarization create an internal electric field inside the InGaN QW. This electric field localizes the

electron and the holes to the opposite heterointerfaces. Another localization mechanism is explained by the fluctuations of the In composition and the fluctuation of the well width. The bandgap of the InN being smaller than that of the GaN compound, the regions that are richer in indium than the average value have a smaller bandgap, and this can induce a localization of the carriers. There also exist fluctuations of the well width near or at the heterointerfaces, that may also change the impact of the QCSE and then produces interfacial potentials minima susceptible to trap the carriers in wide well regions. The localization prevents carrier migrates towards the non-radiative recombination centers. Therefore, this effect helps to enhance the PL intensity of the InGaN/GaN quantum wells similarly to what can be observed for quantum dots in defective materials.

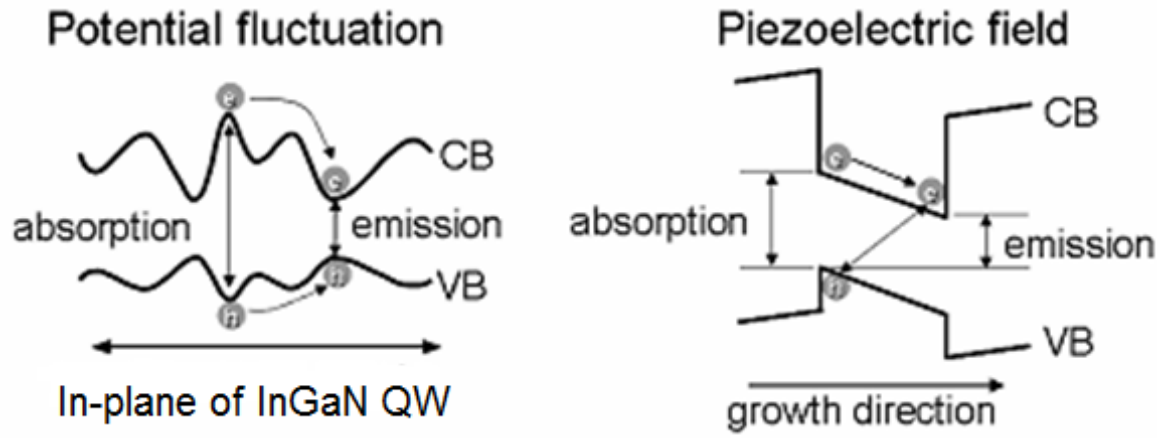

Figure 2.5. Two mechanisms of the localization effect in the InGaN/GaN heterostructures.[13]

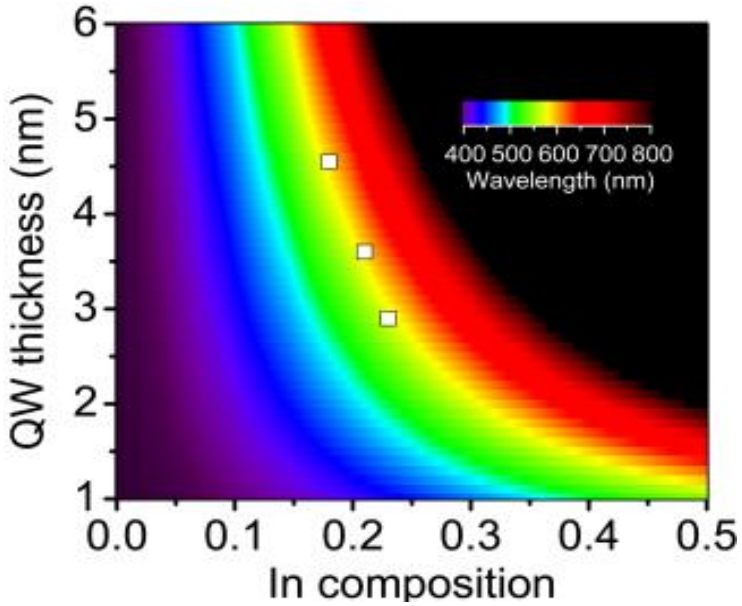

Figure 2.6. Three yellow light emitters InGaN/GaN QWs with different QW thickness and indium composition.[2]

The objectives of this chapter are on one hand to investigate how big the internal electric field and the alloy disorder impact the optical properties of the green-yellow light emitters based-InGaN/GaN QWs and on another hand to determine what is the optimized design. To do so, three yellow InGaN/GaN QW samples with different pairs of (x_{In}, L_W) were grown, as reported in Fig. 2.6. Then, temperature dependent time-resolved photoluminescence (TRPL) measurements are performed for all three samples. The experimental processes are discussed in the following.

2.3. Experimental procedures

The three yellow-emitting multiple quantum well (MQW) samples are grown by metal organic chemical vapor deposition (MOCVD). Each sample contains ten periods of an InGaN/GaN QW with the following indium composition and quantum well width (x_{In}, L_W): (0.23, 2.9 nm), (0.21, 3.6 nm), and (0.18, 4.2 nm), corresponding to samples G_1, G_2 and G_3, respectively. The details on the growth process of these samples can be found in the Refs. 14,15.

The temperature dependent TRPL is performed in the range of 8K-300K, to examine the PL dynamics of the three samples. The fundamental harmonic of a Tsunami Ti:Sapphire at 798 nm at a 82 MHz repetition rate passes through a pulse-picker to select an adapted repetition rate. Then, it passes through a frequency tripler crystal to generate an UV light at a wavelength of 266 nm of wavelength. The PL signal emitted by the sample is collected using a 30cm focal length spectrometer and a 150 groove/mm grating, connected with a Hamamatsu- C10910 streak camera.

2.4. Results and Discussion

Figure 2.7 shows the spectra obtained by time-resolved photoluminescence integrated over time (equivalent CW photoluminescence). Clearly, restricting the time integration over very long time leads to PL peaks always red-shifted compared with spectra obtained restricting the integration to short delays after the excitation pulse. This qualitatively indicates the existence of phase space filling effects together with carrier induced screening of the internal electric field at short delays after the excitation pulse **and** it brings the evidence of localisation of the carriers to fluctuations of the indium composition in the active part of the layers (the shape of the low energy wing of the PL is

not red-shifted when time passes). We cannot discriminate both effects at this stage but the spectral dependence of the recombination times will permit us to dominantly attribute the red-shift to localization phenomena.

The PL intensity $I_{(t)}$ varies exponentially as time passes following the excitation pulse, according to the decay law $I_{(t)} \sim \Gamma_{rad} \exp(-\Gamma t)$ where Γ, the measured recombination rate, is the sum of the radiative Γ_{rad} and the non-radiative contribution Γ_{nonrad}. The integration over time leads to the expression of the PL intensity for continuous excitation conditions as:

$$I_{CW} = I_0 \frac{\Gamma_{rad}}{\Gamma} \qquad (2.2)$$

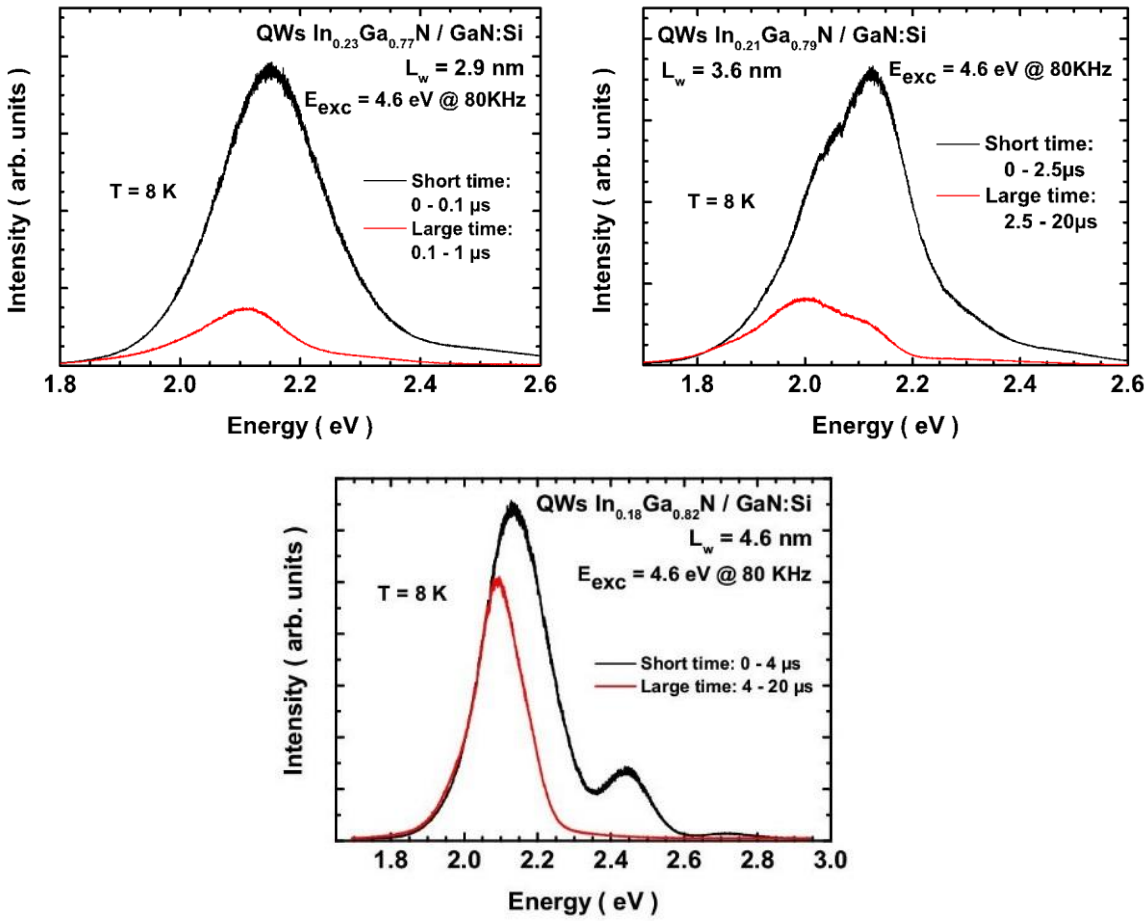

Figure 2.7. Low temperature (8K) CW photoluminescence spectra obtained by time-integrated time-resolved photoluminescence. The redshifts between the short-delay and long delay integrations are 42 meV, 126 meV and 44 meV for sample G_1, G_2 and G_3, respectively.

The radiative and non-radiative decay times are reciprocal quantities of the radiative and non-radiative recombination rates, respectively. The relationship between the PL intensity *I*, the non-radiative (τ_{nonrad}) and radiative (τ_{rad}) decay times is:

$$I(T) \sim \frac{\tau_{nonrad}(T)}{\tau_{nonrad}(T)+ \tau_{rad}(T)} \sim \frac{1}{1+ \frac{\tau_{rad}(T)}{\tau_{nonrad}(T)}} \quad (2.3)$$

Taking for the non- radiative decay time τ_{nonrad} the expression:

$$\tau_{nonrad}(T) \approx \tau_1 \exp(\frac{T_a}{T}) \quad (2.4)$$

Then, the relation of the radiative and non-radiative decay times can be written as:

$$\frac{\tau_{rad}(T)}{\tau_{nonrad}(T)} \approx A \exp(-\frac{T_a}{T}) \quad (2.5)$$

At low temperature, the non-radiative recombination channels are supposed to be inhibited:

$$\frac{\tau_{rad}(T)}{\tau_{nonrad}(T)} \rightarrow 0 \quad (2.6)$$

When the temperature increases up to room temperature the data have to be fitted by using the following equation:

$$I(T) \sim \frac{1}{1+A \exp(-\frac{Ta}{T})} \quad (2.7)$$

The values of A and Ta are gathered in Table II.1 after fitting the Arrhenius plots of Fig.2.8.

The large value of the activation temperature indicates the rapid decrease of the non-radiative decay time when the temperature increases.

Table II.1. Activation temperature deduced for our three samples.

Sample	G_1	G_2	G_3
Well width (nm)	2.9	3.6	4.6
Indium content	0.23	0.21	0.18
A	42.3	66.5	66.0
T_a (K)	333	408	313

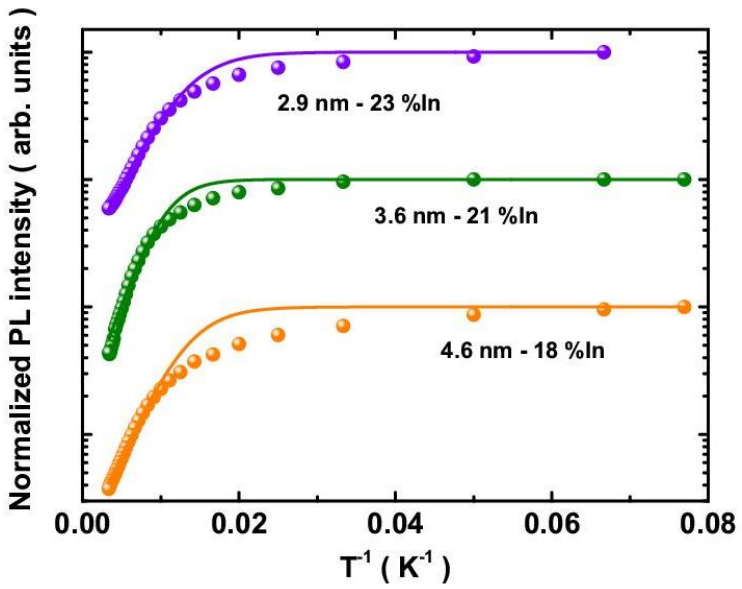

Figure 2.8. Arrhenius plots of the evolution of the normalized photoluminescence intensity versus temperature.

Figure 2.9(a) and Fig. 2.9(b) represent some decay times measured at 8 K and room temperature **on s**ample **G_1** (well width = 2.9 nm, indium content = 0.23). Obviously, the decay times are not mono-exponential, a probe of the alloy disorder.[16,17] We have fitted these decay times using two exponential functions. Second, the characteristic decay time decreases when increasing the lattice temperature as evidence of temperature dependent non-radiative recombination processes and in line with the evolution of the PL intensity with temperature.

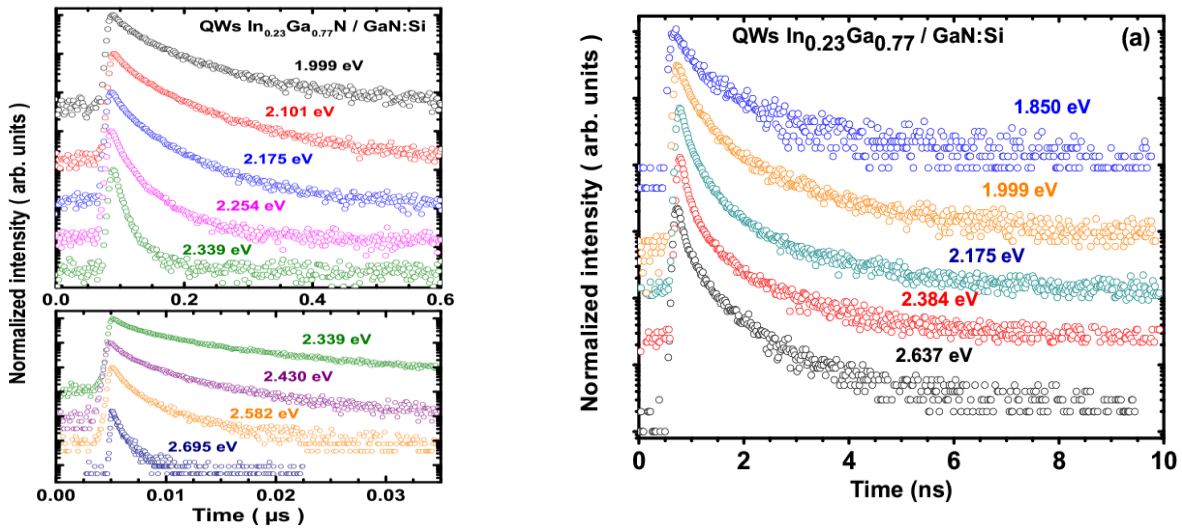

Figure 2.9. (a) Photoluminescence decay times measured for sample G_1 at 8K and (b) at 300K. The decay times are energy-dependent and decrease when increasing T.

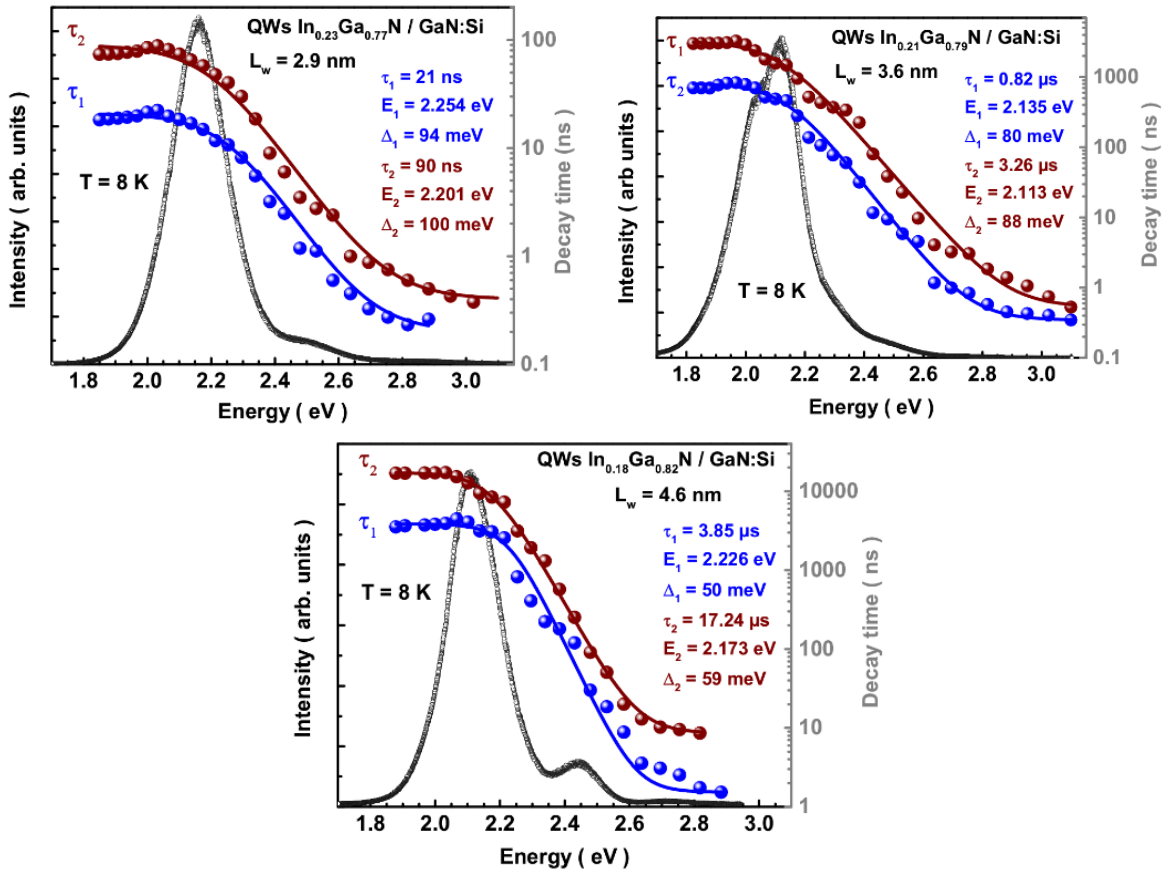

Figure 2.10. Spectral dependences of the decay times for the three samples, measured at 8K. The photoluminescence intensity is represented to help making the correlation between energy and intensity of the emitted light.

Figure 2.10 reports the spectral dependences of the decay times for the three samples. All decay times have been fitted using a function similar to the one introduced by Catherine Gourdon and Philippe Lavallard in Ref. 16:

$$\tau(E) = \frac{\tau_i}{1+\exp(\frac{E-E_i}{\Delta_i})} \qquad (2.7)$$

Many groups have previously obtained this spectral dependence[18-22]. Table II.2 summarizes the characteristics parameters of our decay times at 8 K. The average decay times drastically increase with increasing the well width, which is a clear manifestation of the QCSE. A ratio of about 4 is obtained between the long and short decay times for all the samples. This is not understood at the time of writing. The localization energy is interpreted through parameter Δ which increases with increasing indium content, as expected.

It is interesting to remark that value of parameter A scales between 42 and 66 although the value of the decay time that is measured at 8K and then interpreted in terms of the radiative decay time scales several decades from 21 ns up to about 17.2 μs. This evidences a correlation between the non-radiative characteristics time τ_{nonrad} and the radiative one τ_{0i} in the table above.

Table II.2. Characteristics parameters of our decay times at 8 K.

Sample	**G_1**	**G_2**	**G_3**
Well width (nm)	2.9	3.6	4.6
Indium content	0.23	0.21	0.18
E_{01} (eV)	2.254	2.135	2.226
Δ_{01} (meV)	94	80	50
τ_{01} (ns)	21	820	3850
E_{02} (eV)	2.201	2.113	2.173
Δ_{02} (meV)	100	88	59
τ_{02} (ns)	90	3260	17240
A	42.3	66.5	66.0

Finally, in the spirit of the idea initiated in the group of Professor Hangleiter at the technical university of Braunschweig,[4,25] we have plotted the decay times versus the product of the well width time the indium content in order to express the influence of the QCSE through the well width and chemical contrast.[4,25,26] The result is reported in Fig. 2.11 which obviously evidences a global correlation in the world wide published experiments. The whole set of data of Fig. 2.11 can also be approximately reproduced by our calculation. The curves correspond to calculations of the radiative lifetime for different indium compositions and QW thicknesses. Dotted lines are for a fixed quantum well width and a variable indium composition and solid lines for a fixed indium composition and a variable quantum well width. Note that for data points located inside the shaded area, the calculated photoluminescence wavelength is longer than 550 nm at 8K. *Our results indicate that the design to target is thin well width and high indium compositions.* The scattering of data is sometimes related to inconsistencies that we attribute from *bonafide* to erroneous determinations of the decay times (repetition rates of the excitation source too high).

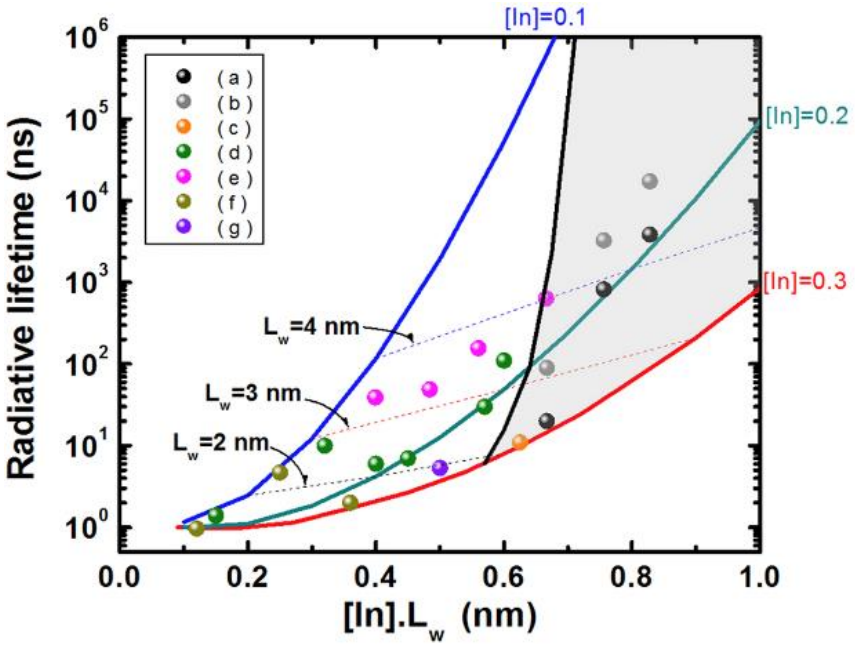

Figure 2.11. Evolution of the decay times for (Ga,In)N/GaN quantum wells as a function of the indium composition and the quantum well width. (a) and (b): this work; (c): ref. [17]; (d): ref. [18]; (e): ref. [19]; (f): ref. [20]; (g): ref. [21].

In summary, we have demonstrated during this work (that was my Master internship work), for all our yellow light emitting (Ga,In) N-based devices grown with difference of the well width and indium composition, the existence of very similar behaviors in terms of excitonic recombination dynamics. The TRPL spectra always exhibit a two-mode recombination kinetics with a long and a short decay times. From temperature-dependent photoluminescence spectra, we obtained large values of activation temperature that indicate the increase of the non-radiative recombination rate in indium-rich regions when the temperature increases. Plotting the decay times versus the product of the well width and the indium composition, we found significantly correlations. This product is found to be an excellent indicator of the device performance. This quality proves that the best design to achieve efficient yellow light emitters is high indium composition and thin well layer. Based on these results complementary samples have been grown with alternative designs and optimized crystalline qualities. They will be studied in the next chapters.

References

1. M. Auf der Maur, A. Pecchia, G. Penazzi, W. Rodrigues, and A. Di Carlo, Phys. Rev. Lett. **116**, 027401 (2016)
2. B. Damilano and B. Gil, J. Phys. D: Appl. Phys. **48**, 403001 (2015)
3. A. E. Romanov, T. J. Baker, S. Nakamura, and J. S. Speck, J. Appl. Phys. **100**, 023522 (2006)
4. T. Langer, A. Kruse, F.A. Ketzer, A. Schwiegel, L. Hoffmann, H. Jönen, H. Bremers, U. Rossow, and A. Hangleiter, Phys. Stat. Sol. C **8**, No. 7–8, 2170 (2011)
5. S. Nakamura: MRS Bull. **34**, 101(2009)
6. H. T. Ngo, D. Rosales, B. Gil, P. Valvin, B. Damilano, K. Lekhal, P. De Mierry, Proc. SPIE **9363**, 93630K-1 (2015)
7. D. M. Graham, P. Dawson, M. J. Godfrey, M. J. Kappers, P. M. F. J. Costa, M. E. Vickers, R. Datta, C. J. Humphreys, and E. J. Thrush, Phys. Stat. Sol. (c) **3**, 1970 (2006)
8. I. Ho, and G.B. Stringfellow, Appl. Phys. Lett. **69**, 2701 (1996)
9. T. Matsuoka, Appl. Phys. Lett. **71**, 105 (1997)
10. T. Matsuoka, H. Tanaka, T. Sasaki and A. Katsui, "Institute of Physics Conference" **106**, 141 (1990)
11. S. Zhang, J.-j. Shi, M. Zhang, M. Yang, and Jia Li, J. Phys. D: Appl. Phys. **44**, 495304 (2011)
12. A. Wakahara, T. Tokuda, X.-Z. Dang, S. Noda, and A. Sasaki, Appl. Phys. Lett. **71**, 906 (1997)
13. Y. Kawakami, A. Kaneta, and M. Funato, Materials Science Forum. **590**, 249 (2008)
14. B. Damilano, H. Kim-Chauveau, E. Frayssinet, J. Brault, S. Hussain, K. Lekhal, P. Vennéguès, P. De Mierry, and J. Massies, Appl. Phys. Express. **6**, 092105 (2013)
15. K. Lekhal, S. Hussain, P. De Mierry, P. Vennéguès, M. Nemoza, J.-M. Chauveau, and B. Damilano, J. Cryst. Growth **434**, 25 (2016)
16. C. Gourdon, and P. Lavallard, Phys. Stat. Sol. B **153**, 641 (1989)
17. A. Morel, P. Lefebvre, S. Kalliakos, T. Taliercio, T. Bretagnon, and B. Gil, Phys. Rev. B **68**, 045334 (2003)
18. S. F. Chichibu, T. Azuhata, T. Sota, T. Mukai, and S. Nakamura, J. Appl. Phys. **88**, 5153 (2000)

19. Y. Narukawa, Y. Kawakami, S. Fujita, S. Fujita, and S. Nakamura, Phys. Rev. B **55**, R1938 (1997)
20. S. F. Chichibu, Y. Kawakami, and T. Sota, [Introduction to nitride semiconductor blue lasers and light emitting diodes], Taylor and Francis, New York, 153-270 (2000)
21. Y. Kawakami, [Low-dimensional nitride semiconductors], Oxford University Press, Oxford, 232-255 (2002)
22. C. Netzel, H. Bremers, L. Hoffmann, D. Fuhrmann, U. Rossow, and A. Hangleiter, Phys. Rev. B **76**, 155322 (2007)
23. S. Saito, R. Hashimoto, J. Hwang, and S. Nunoue, Appl. Phys. Express. **6**, 111004 (2013)
24. J. Hwang, R. Hashimoto, S. Saito, and S. Nunoue, Appl. Phys. Express. **7**, 071003 (2014)
25. T. Langer, H. Joenen, A. Kruse, H. Bremers, U. Rossow, and A. Hangleiter, Appl. Phys. Lett. **103**, 022108 (2013)
26. D. Rosales, H. T. Ngo, P. Valvin, K. Lekhal, B. Damilano, P. De Mierry, B. Gil, and T. Bretagnon, Superlattice Microst. **76**, 9 (2014)

CHAPTER III

INTERNAL QUANTUM EFFICIENCY AND AUGER EFFECT IN POLAR ORIENTED GREEN-RED EMITTING InGaN-GaN MULTIPLE QUANTUM WELLS WITH AlGaN STRAIN-COMPENSATING LAYERS

As demonstrated in the chapter II, the growth of high radiative efficiency and long wavelength emitting InGaN-GaN quantum wells (QWs) requires using high indium compositions and thin quantum wells in order to minimize the deleterious influence of the quantum confined Stark effect (QCSE). The relevant indicator is the product of the indium composition timed by the well-width, which, when minimized as much as possible, will lead to the optimization of the optical performances of the device, as we have proposed it earlier in this PhD document.

However, it is tricky to grow high crystalline quality indium-rich QWs because of the differences in thermal stability of the different materials, namely GaN (barrier layer) and InGaN (QW layer) that are assembled to form heterostructures on one hand. On another hand, InN and GaN are lattice mismatched which leads to strained-layers during the coherent epitaxy of InGaN on GaN. Beyond a critical thickness, formation of dislocations or other extended defects becomes highly probable which degrades the InGaN quality.

Recently, S. Nunoue et al. demonstrated that embedding an AlGaN interlayer between the ternary InGaN quantum well layer and the GaN barrier layer could improve the efficiency of green-yellow or even red light emitting diodes (LEDs) based on multiple quantum well (MQW) designs[1-3] In such structures, the AlGaN interlayer enhances the electric field in InGaN/GaN quantum well via increasing of the total polarization mismatch, and it then produces a more pronounced distorsion of the electron and holes wave functions to opposite sides of the InGaN confining layer than in case of GaN-InGaN QWs. Hence, this leads to a red-shift in emission wavelength compared to AlGaN-free InGaN-GaN MQWs as sketched in Fig. 3.1.

In this chapter, *we will present the study of the impact of the design of such strain-compensated multi-quantum wells (SCMQWs) regarding the internal quantum efficiency (IQE) under weak photo-excitation densities. We will also examine its impact for the onset of non-radiative Auger recombination in polar oriented InGaN-AlGaN-GaN in such SCMQWs.*

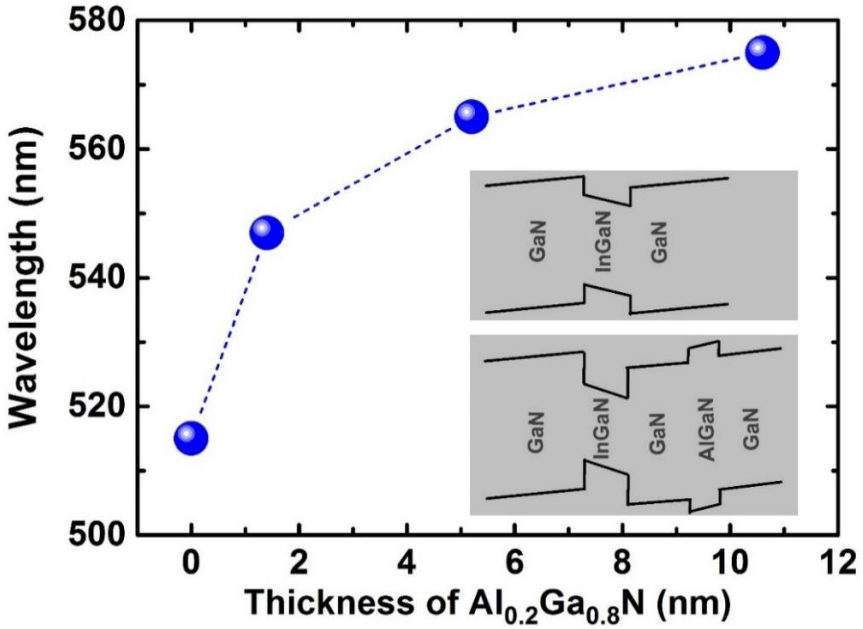

Figure 3.1. Emission wavelength as a function of AlGaN thickness. Inset: potential line-ups of one basic building block of InGaN-GaN multiple quantum wells without and with $Al_{0.2}Ga_{0.8}N$ layer.

3.1. Growth samples process

Starting from the idea that the lattice constant of (Al,Ga)N is smaller than the corresponding values for (In,Ga)N and GaN, we can argue that inserting an AlGaN layer between InGaN quantum well and GaN barrier can reduce the lattice mismatch in the whole structure. It is possible to demonstrate that the elastic strain energy can get a minimum at an equilibrium lattice parameter, a_{eq}, (in-plane lattice parameter) by just changing of AlGaN layer thickness as expressed in following equation:[4]

$$E_{el}(a_{eq}) = \sum_{i=1}^{3}(M_i L_i \Delta_i^2) \quad (3.1)$$

where M_i is the biaxial modulus; L_i is the layer thickness; a_i is the relaxed lattice parameter of each *i* layer; $\Delta_i = (a_{eq} - a_i)/a_i$ is the strain in the growth plane.

Chronologically, we first targeted emission in the yellow, thus we grew four samples namely M_1, M_2, M_3, M_4 with different thickness of AlGaN layer by metal organic chemical vapour deposition (MOCVD). Starting from a *c*-plane sapphire substrate, a 6 µm

of un-doped GaN buffer layer was grown, we then deposited 800 nm of n-type GaN grown at 1080°C that were followed by a ten-period multi-quantum well (MQW) structure.

Within a basic building block, the InGaN quantum well was grown at 715°C during 120 seconds for all samples to get indium composition and well width fixed at 0.21 and 2.6 nm, respectively. To avoid indium desorption, 3 nm of un-doped GaN was grown at the same temperature (715°C) as a protective layer. Then, a couple of barrier layers of $Al_{0.2}Ga_{0.8}N$ and GaN was grown at 940 °C before the growth of the InGaN layer of the next building block began. We wish to outline that the thicknesses of these two layers were changed together to keep a total barrier thickness around 17 nm. The thickness of $Al_{0.2}Ga_{0.8}N$ is 0, 1.4, 5.2 and 10.6 nm for sample M_1, M_2, M_3, M_4, respectively.

To improve the crystalline quality and the optical properties of our samples[5-7], light doping of both of $Al_{0.2}Ga_{0.8}N$ and GaN barrier layers with silicon was decided, at a dose of about 5 x 10^{18} cm^{-3}. Also, we plan to use these MQWs as light converters for monolithic phosphor-free white LEDs with current injection through the MQWs so we need that these layers are doped.[8] The schematic of the growth process of our samples is shown in Fig. 3.2.

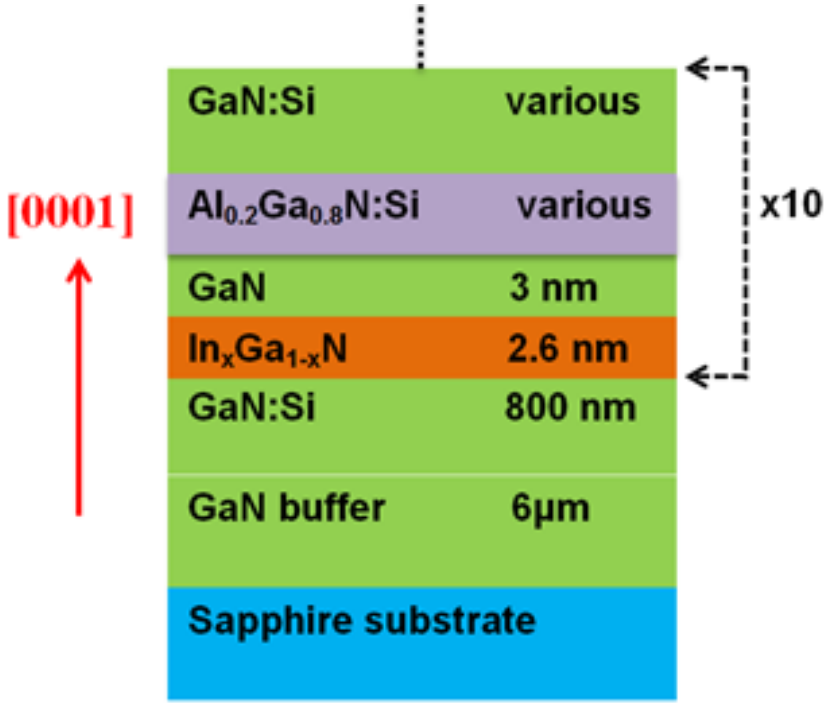

Figure 3.2: Schematic of the sample design.

X-rays diffraction measurements were carried out to get information about samples structure. The diffraction spectra of samples M_1 to M_4 plotted in Fig. 3.3 show that the zero-order of the MQW peak progressively merges with the GaN (0002) diffraction peak

when the AlGaN thickness increases. It indicates that we also get strain compensating in the growth direction of MQW. So, the elastic strain energy is minimized by inserting thicker AlGaN layer, consequently the values of in-plane and on-axis lattice parameters of MQW progressively matches with lattice constant of GaN. The broadening of the satellite lines that probe the periodicity of the MQW system also decrease when increasing the thickness of AlGaN which is a good thing regarding the quality of the growth protocol.

As we got good X-ray diffraction features (Fig. 3.3) and photoluminescence results (hereafter), we extended our approach towards growth a red-light sample called M_5 that grown at posteriori. This sample was grown with the same growth conditions as sample M_3 excepted that the growth temperature was reduced from 715°C to 700 °C to increase indium composition of the InGaN quantum well.[9,10] The growth parameters of all samples are listed in Table III.1.

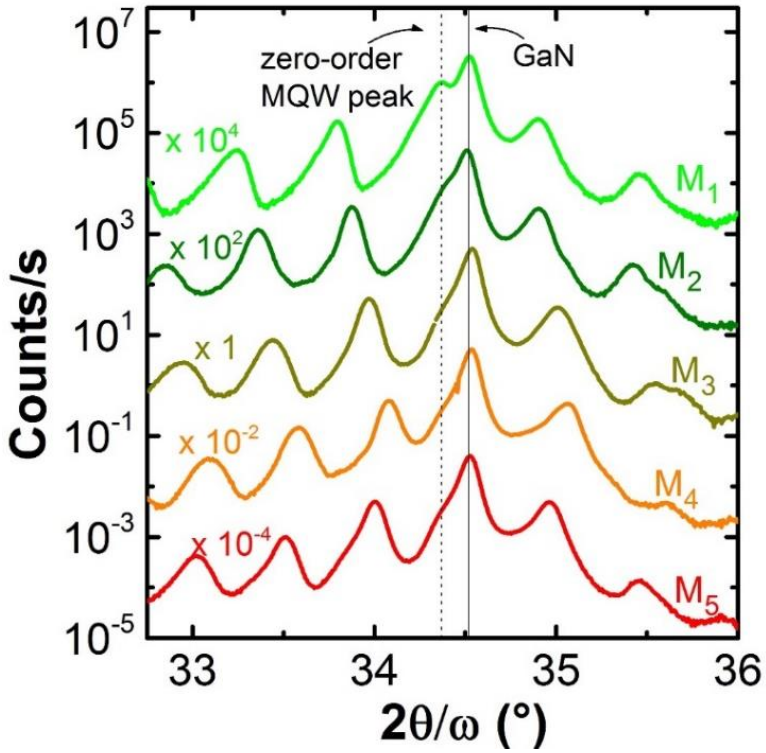

Figure 3.3: 2θ/ω X-ray diffraction spectra of sample sample M_1, M_2, M_3, M_4, and M_5. The solid line shows position of diffraction peak of (0002) GaN planes. The dashed line corresponds to mean peak of the multi-quantum well of sample M_1.

Table III.1: Growth parameters of samples: $T_{G\text{-}QW}$ and $t_{G\text{-}QW}$ respectively correspond to the growth temperature and to the growth time of InGaN quantum well, x_{In} represents the indium composition in the InGaN quantum well, L_{InGaN}, L_{AlGaN}, and L_{GaN} are the thicknesses of the InGaN quantum well, of the $Al_{0.2}Ga_{0.8}N$, and of the GaN barrier layers, respectively. F is the calculated electric field inside InGaN quantum well.

Sample	$T_{G\text{-}QW}$ (°C)	$t_{G\text{-}QW}$ (s)	x_{In}	L_{InGaN} (nm)	L_{AlGaN} (nm)	L_{GaN} (nm)	F ($MVcm^{-1}$)
M_1	715	120	0.21	2.6	0	15.2	2.9
M_2	715	120	0.21	2.6	1.4	15.6	3.1
M_3	715	120	0.21	2.6	5.2	11.9	3.5
M_4	715	120	0.21	2.6	10.6	7.0	4
M_5	700	120	0.23	2.6	5.2	11.9	3.7

According to the parameter values of the different M_1-M_5 samples, we can calculate the equilibrium in-plane parameter of each InGaN/AlGaN/GaN MQW. This value is 3.199, 3.197, 3.194, 3.189, and 3.194 Å for sample M_1, M_2, M_3, M_4, and M_5, respectively. The best lattice matching is therefore achieved for the sample M_4.

3.2. How are impacting AlGaN strain-compensating layers on the optical properties of InGaN quantum well?

In this section, we focus on the influence of the thickness of the AlGaN layer on the optical performance of all the InGaN/AlGaN/GaN multi-quantum well structures by using CWPL and TRPL measurements.

3.2.1. Red-shift and enhancement of photoluminescence intensity

Let us first discuss the CWPL properties of the samples. At low temperature, we observe a red-shift of the maximum PL peak energy for samples M_1 to sample M_5 as shown in Fig. 3.4(a). This red-shift correlates with the increase of the AlGaN thickness. The projections of these 8K photoluminescence features into the chromaticity diagram[11] (CIE-1978 convention) are reported in Fig. 3.4(b). Obviously, as the bandgap of AlGaN is larger than GaN, one could guess that replacing GaN by AlGaN should induce a blue-shift of the PL peak wavelength in straightforward correlation with the deepening of the potential line-ups. This is not observed. Actually, the contrary is found! There is no controversy about that: the observation of this red-shift is correlated to an increase of the internal electric field in the InGaN quantum wells, and it is a manifestation of the QCSE. The values of internal electric field in the InGaN quantum well layers were calculated

using Eq. 1.16 in chapter I. Values we find for the increase of internal electric field that are 2.9, 3.1, 3.5, 4.0 and 3.7 MVcm^{-1} corresponding to sample M_1, M_2, M_3, M_4 and M_5, as listed in Table III.1. We remind that the well layers of sample M_5 contain more indium content than the well layers of the other samples, making this sample to behave "slightly apart" from the rest of the series. Thus, although the electric field is smaller in sample M_5, its PL peaks at longer wavelength than sample M_4.

Besides the red-shift of the PL peak wavelength, we also observe in Fig. 3.4(a) an increase of the PL intensity with the AlGaN thickness. To qualitatively explain this enhancement, we remind that using AlGaN interlayer minimizes the elastic strain energy stored in the structure, and hence may lead to a reduction of dislocations acting as non-radiative recombination centers. Adding AlGaN strain-compensated layer may substantially increase the material quality that in turn enhances the PL intensity through the series of samples M_1 to M_4.

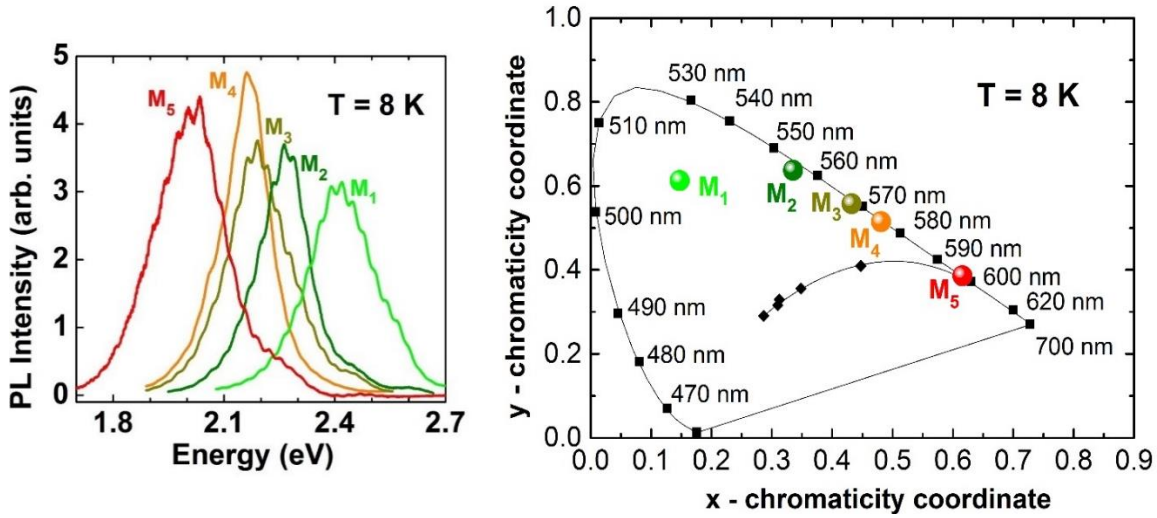

Figure 3.4: (a) Photoluminescence spectra of sample M_1, M_2, M_3, M_4 and M_5 at low temperature. (b) Projection of the 8K photoluminescence features of all samples into the CIE-1978 convention chromaticity diagram.[11] The black diamonds correspond to different temperatures of the black body radiation: 10^4 K 6770 K, 6500 K, 4870 K, 2856 K, respectively from the left-hand side to the right-hand one.

3.2.2. Temperature dependent photoluminescence

Figure 3.5 gives the comparison between the 8 K PL spectra of our samples and their 300 K analogues. At room temperature, we observe a global broadening and a red-shift of the PL spectra compared to low temperature. The PL spectrum of sample M_5 is clearly structured into two components as the collapse of the intensity of the main peak at 2 eV reveals the contribution of the yellow band arises at ~2.2 eV. This latter contribution

poorly varies with T. Regarding sample M_1, a transition state is reported at 2.7 eV. Its PL intensity and its energy do not vary with T and we attribute it from *bonafide* excitons localized to potential fluctuation in InGaN. The intensity of this line varies with the position of the laser and is maximum for the position chosen here as an indication of sample inhomogeneities.

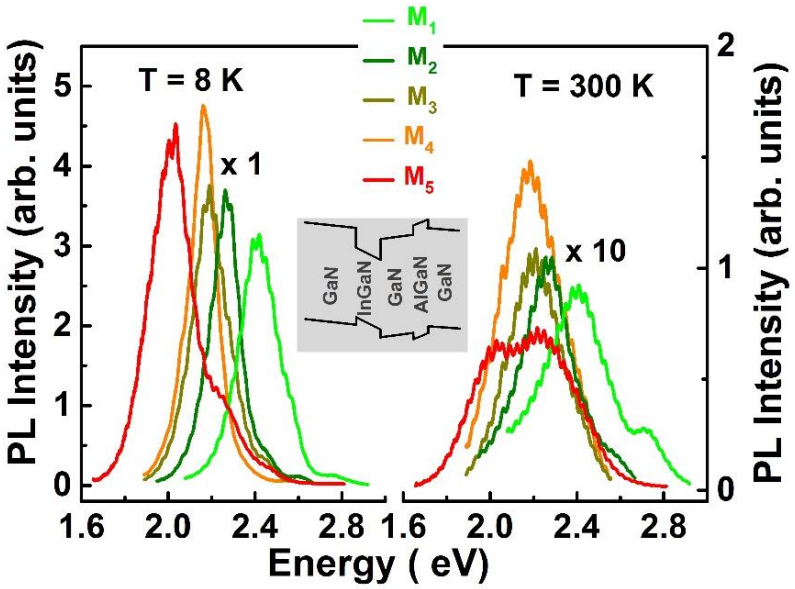

Figure 3.5. Photoluminescence spectra of all samples at 8 K and 300K. The wavelength of the excitation laser was 266 nm, with a power density of 2 Wcm^{-2}.

As shown in Fig. 3.6, the integrated PL intensities keep constant values at low temperature then they collapse at high temperature where the non-radiative recombination processes are substantial. The decrease of the integrated PL intensities with the increase of temperature is caused by two kinds of thermal quenching that can be characterized by activation temperatures T_a and T_b expressed as:[12,13]

$$I_T = \frac{I_0}{1+Aexp\left(\frac{-T_a}{T}\right)+Bexp\left(\frac{-T_b}{T}\right)} \quad (3.2)$$

where I_0 and I_T are the PL intensities at low temperature (8 K) and at a given temperature T, coefficients A and B account for the strength of two thermal quenching mechanisms that correspond to the activation energies E_a and E_b. These activation energies are defined *via* a relationship with the activation temperature as:

$$E_a = k_b.T_a \quad (3.3)$$

$$E_b = k_b.T_b \quad (3.4)$$

in which k_b is the Boltzmann constant.

The values of these quantities are summarized in Table III.2 after a careful fitting of the experimental data by Eq. (3.2). We find a trend that E_a (or T_a) and E_b (or T_b) decrease with the increase of the AlGaN thickness. We interpret the values of these activation energies as two different thermal activation processes.

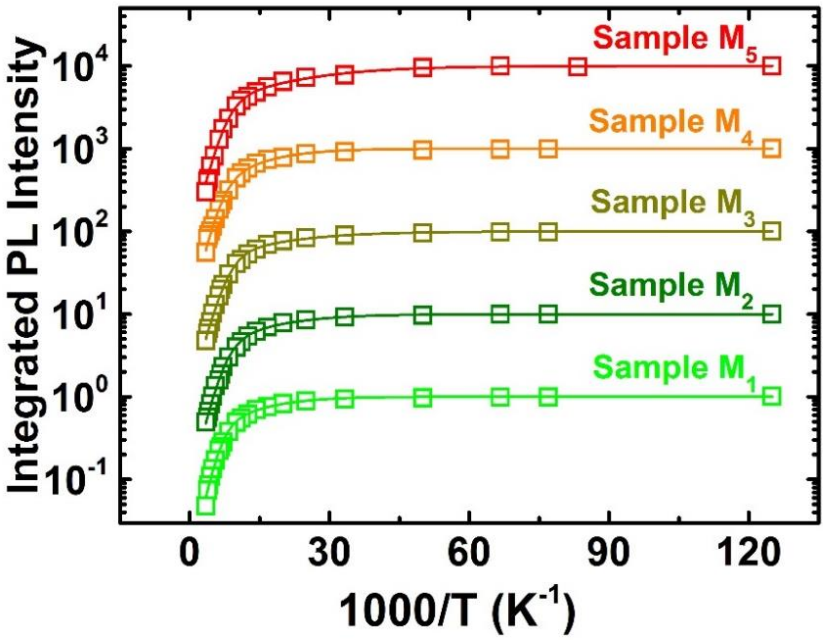

Figure 3.6. Arrhenius plots of integrated PL intensity of all samples as a function of the reciprocal temperature. The open squares represent the experimental data and the solid lines account for the fitting lines.

Table III.2. Characteristics parameters of the samples: x_{In} is the indium composition. L_{InGaN}, L_{AlGaN} and L_{GaN} are the widths of well layer (In,Ga)N, $Al_{0.2}Ga_{0.8}N$ and GaN barrier layers, respectively. Coefficients A, B, activation temperatures T_a, T_b and activation energies E_a, E_b are assessed by applying the fitting due to Eqs. (3.2), (3.3) and (3.4).

Sample	x_{In}	L_{AlGaN} (nm)	L_{GaN} (nm)	A	T_a (K)	E_a (meV)	B	T_b (K)	E_b (meV)
M_1	0.21	0	15.2	4.9	180	15.5	320	696	60
M_2	0.21	1.4	15.6	3.7	114	10	265	618	53
M_3	0.21	5.2	11.9	2.7	95	8	240	610	52
M_4	0.21	10.6	7.0	1.2	72	7	120	529	46
M_5	0.23	5.2	11.9	2.6	73	7	130	734	63

At very low temperature, carriers are localized to shallow and deep local minimum potentials where the carriers mainly recombine radiatively[14], as illustrated in Fig. 3.7. When temperature increases, the carriers are thermally activated. At a temperature T_a, corresponding to the localization energy E_a, where the carriers have high enough thermal energy to get out of the shallow localization states and go into deeper localization ones.[15,16] When the temperature further increases, near the value of T_b, carriers have enough energy to escape from these deep localized-states of InGaN quantum well and migrate through the whole structures.[12] At this stage, the probability that the carriers are trapped by non-radiatively centers significantly increases. Consequently, the PL intensity decreases. We remind that thicker AlGaN layer minimizes the elastic strain energy stored in the structures, and then it decreases the density of non-radiative recombination centers. In addition, adding AlGaN layer probably reduces the interface roughness, this can be the reason of the reduction of the activation energies E_a and E_b with increasing AlGaN thickness.

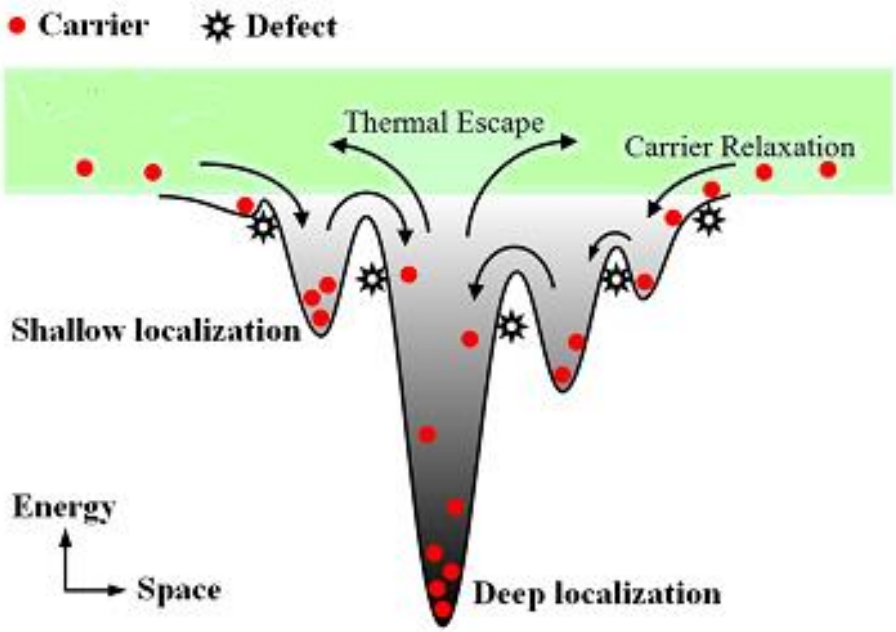

Figure 3.7. Schematic diagram of carrier transport, carrier relaxation at different level of local potential minima in inhomogeneous materials.[14]

When we compare the 300 K photoluminescence of samples relatively to the PL intensity of sample M_1, we find that the PL intensity is enhanced by adding thicker AlGaN layer but is decreased by increase of indium composition, as shown in Fig. 3.8.

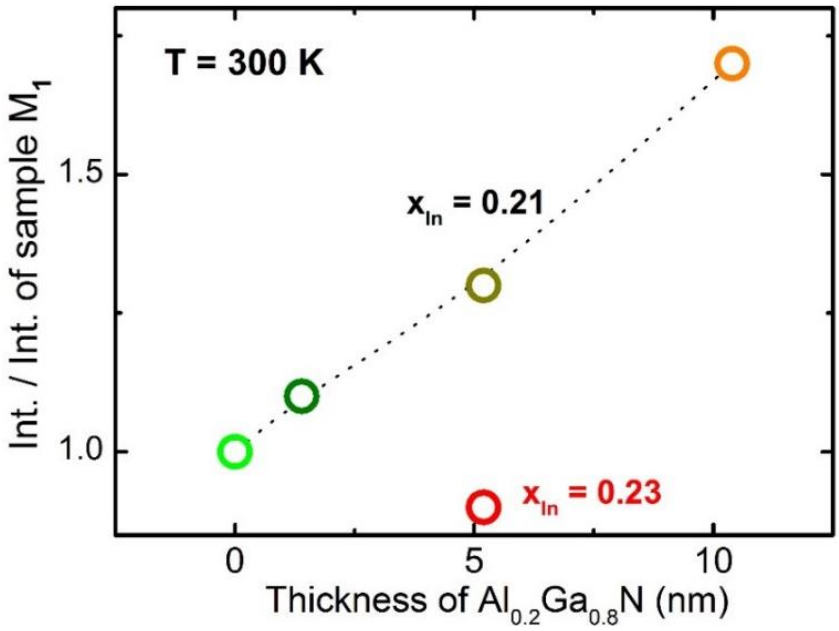

Figure 3.8. 300 K photoluminescence integrated intensity (open circles) as a function of the $Al_{0.2}Ga_{0.8}N$ thickness normalized by the PL intensity of sample M_1.

3.2.3. Effect of the AlGaN layer on exciton states

We remind that a thicker AlGaN layer induces a higher electric field inside the InGaN quantum wells causing a reduction of the exciton binding energy, as we will discuss hereafter.

The electron and hole wavefunctions of these samples have been calculated for us by Pierre Bigenwald. The results are shown in Fig. 3.9. As expected, we clearly see that the electric field splits the wavefunctions of electrons and holes and then reduces their overlap. To match the energies of the calculation with the experimental values we had to slightly modify the composition and the well width of sample M_5, as listed in Table III.3. We know since the work of Gorczyca that the bandgap bowing of ternaries strongly depends on microstructure effects.[17] As we used Morel's model did not include such effect that may shift apart bandgap of sample M_5 for this composition.[18]

Bigenwald also has helped us to compute the evolution of exciton binding energy by using a trial function $\psi_{\rho,z,\phi}(\rho, z, \phi)$, in which z represents the growth direction, ρ accounts for in-plane distance of electron-hole pair, ϕ is the azimuthal angle, to describe the excitonic interaction.

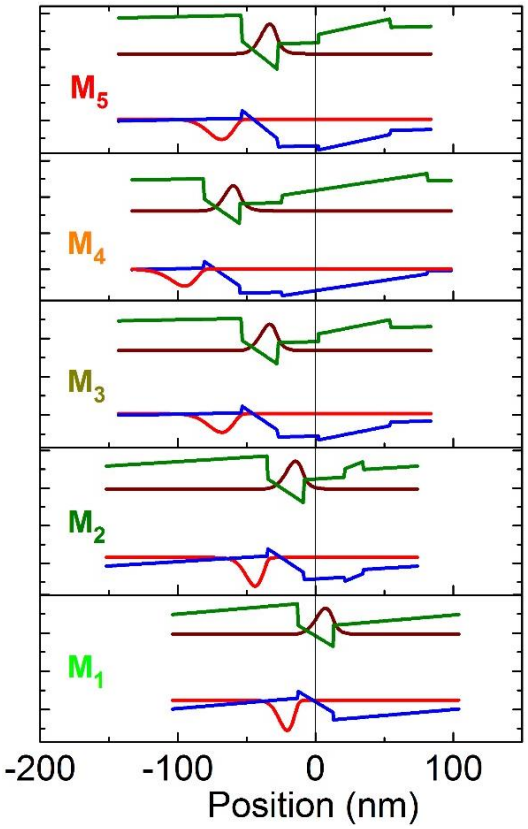

Figure 3.9. The band structure and wavefunctions of electrons and holes in samples M_1, M_2, M_3, M_4, and M_5.

Along growth axis, exciton is not only affected by the heterostructure potential but also by the Coulomb attraction. Therefore, a two-parameter approach is used to describe the hydrogenic part of the envelope function as $\exp(-\sqrt{\rho^2 + \alpha^2 z^2}/\lambda)$ with α is the dimensionality of the excitonic trial function and λ is the in-plane Bohr radius.

Then, the excitonic wavefunction can be expressed as

$$\Psi_{(z_e, z_h, \rho, \emptyset)} = \chi_e(z_e)\chi_h(z_h)\,\psi_{\rho,z,\theta}(\rho, z, \emptyset) \quad (3.5)$$

where χ_e and χ_h are the envelope function of the confined electron and holes, z = z_e - z_h

The excitonic binding energy is determined by a minimization procedure through α and λ

$$E_B = min_{\alpha,\lambda} \langle \Psi | H_{exc} | \Psi \rangle \quad (3.6)$$

with $H_{exc} = -\frac{h^2}{2\mu}\left(\frac{\partial^2}{\partial \rho^2} + \frac{1}{\rho}\frac{\partial}{\partial \rho}\right) - \frac{e^2}{4\pi\epsilon_0\epsilon_r}\frac{1}{\sqrt{\rho^2 + (z_e - z_h)^2}} + \frac{1}{\rho^2}\frac{\partial^2}{\partial \emptyset^2}$ is the Hamiltonian of exciton, μ is effective mass, ϵ_0 and ϵ_r are dielectric constant in vacuum and relative dielectric constant, respectively.

The oscillator strength is proportional to

$$\frac{4}{\lambda^2}\frac{\left|\int \chi_e(x)\,\chi_h(x)dx\right|^2}{\left(\frac{2\alpha|z|}{\lambda}+1\right)\exp\left(-\frac{2\alpha|z|}{\lambda}\right)\int\left(\chi_e^2(z_e)dz_e\right)\int\left(\chi_h^2(z_h)dz_h\right)} \qquad (3.7)$$

The values of the parameters used for the calculation of the excitonic binding energy E_B, and the oscillator strength are listed in Table III.3. We find that the exciton binding energy E_B reduces with the product of indium composition and electric field in InGaN quantum well while the in-plane Bohr radius λ increases with this indicator as shown in Fig. 3.10. The decrease of E_B is an evidence of the spatial separation of the electron-hole wavefunctions induced by the internal electric field in the well layers that produces reduction of overlapping of electron-hole function and gives reduction of oscillator strength for exciton transition. The increase of the in-plane Bohr radius λ results from a decrease of the Coulomb attraction because when the in-plane radius extends, the density of exciton-exciton interaction Ns is reduced by expression $Ns = \beta/\lambda^2$ with $0.01 \leq \beta \leq 0.04$.[19]

Table III.3. Sample parameters are used in the calculation. E, E_B are the band to band energy, the exciton binding energy. The values of α, λ, the band to band overlap, and the oscillator strength in arbitrary units. The well width of sample M_5 is slightly modified compared to the nominal value.

Sample	x_{In}	L_{InGaN} (nm)	E (meV)	α	λ	Overlap	E_B (meV)	Osc strength
M_1	0.21	2.6	2341.5	0.462	51.8	0.29	-21.7	0.19
M_2	0.21	2.6	2306.3	0.461	53.3	0.189	-20.8	0.118
M_3	0.21	2.6	2240.2	0.418	58.5	0.0588	-18.4	0.0305
M_4	0.21	2.6	2178.3	0.42	58.9	0.0426	-18.1	0.0219
M_5	0.23	2.8	2009.1	0.39	60.9	0.0198	-17.5	0.00942

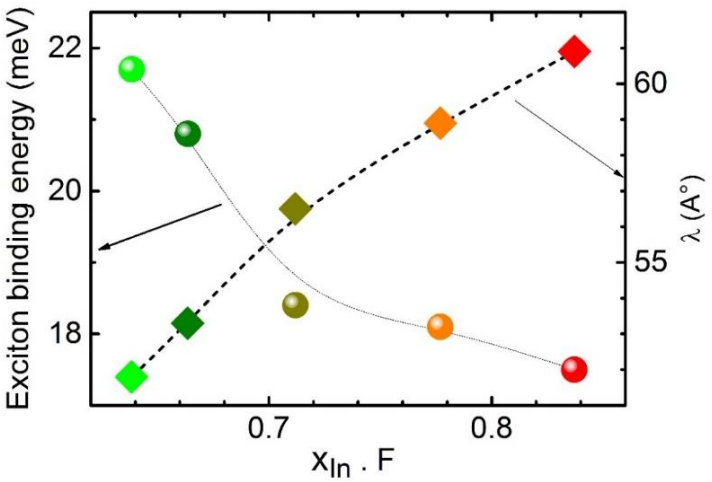

Figure 3.10. Evolution of exciton binding energy (spheres) and in-plane Bohr radius (diamond) as a function the product of the indium composition and the electric field in InGaN quantum well for the samples M_1, M_2, M_3, M_4, and M_5.

3.3. Internal Quantum Efficiency from TRPL in inhomogeneous samples

3.3.1. The internal quantum efficiency at low excitation level

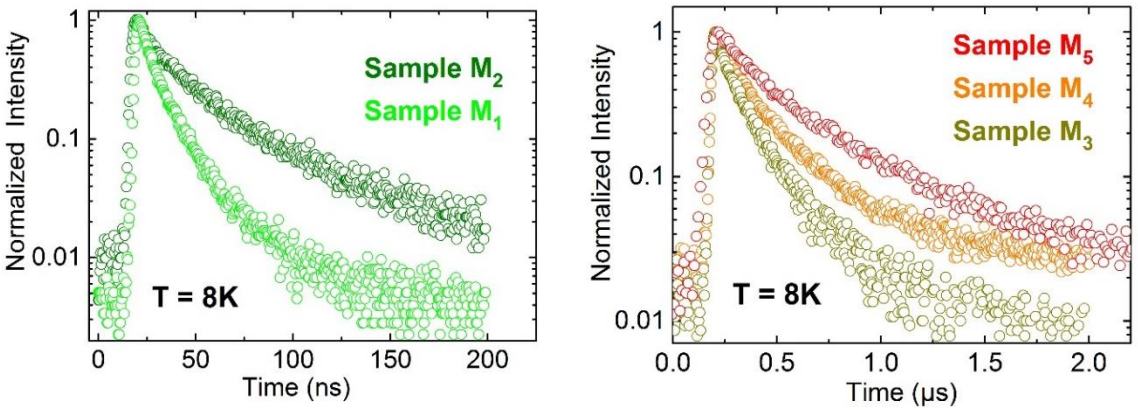

Figure 3.11: Transient photoluminescence of samples M_1, M_2, M_3, M_4 and M_5 measured at 8 K using the adapted time scale windows of the Hamamatsu streak camera. Note that the intensities are zero at both ends of the time scale of the data collection, which indicates that we have a global description of the full decays.

The time-resolved photoluminescence spectroscopy measurement was carried out at 8K to study the PL kinetic processes and to reveal the different recombination processes. As observed in Fig. 3.11, the PL transients of all our samples are not ruled by a single exponential time decay. They instead always exhibit a double-exponential decay with a fast decay component and a long one. The PL intensity I(t) decay is expressed by the following equation:

$$I(t) = A_{fast} \exp\left(\frac{-t}{\tau_{fast}}\right) + A_{slow} \exp\left(\frac{-t}{\tau_{slow}}\right) \quad (3.8)$$

where τ_{fast} and τ_{slow} account for fast decay and slow decay, A_{fast} and A_{slow} represent the coefficient of fast and slow recombination processes, respectively.

Recently, Iwata et al. have developed a model to explain quantitatively the origin of this bi-exponential behavior[20]. The spirit of this model is sketched in Fig. 3.12. **It applicates for samples which are inhomogeneous** and when it is possible to consider regions of the samples where the photo generated electron and holes pairs (excitons) recombine through very different regimes that are characterized by dynamics ruled by τ_{fast} and τ_{slow}. We consider an experiment when the laser excitation is as low as possible (to permit the experiment in good signal to noise ratio) and is realized with a spot of total surface A. Part of the laser spot (with surface A_{slow}) corresponds to a good quality material

with a low enough density of defects so that the excitons (electron-hole pairs) can here recombine radiatively with characteristic time τ_{slow}. In the rest $A_{fast} = A - A_{slow}$ of the sample area shined by the excitation laser, where the sample quality is worse, more defective, excitons can either recombine radiatively or recombine non-radiatively via defects. The characteristic time τ_{fast} for recombination processes in this region is expressed by

$$\frac{1}{\tau_{fast}} = \frac{1}{\tau_{slow}} + \frac{1}{\tau_{nonrad}} \tag{3.9}$$

where τ_{slow} represents for radiative decay time, while τ_{nonrad} represents for the nonradiative decay time.

When $\tau_{fast} < \tau_{slow}$ by one decade or more, and when the temperature is low enough to avoid cross talking of excitons between both regions, the slow decay and the fast decay are spatially isolated. Otherwise the conditions of applicability of the model are not fulfilled. If the photo-excitation density is not small enough phase space filling effects and de-screening of the electric field will occur also proscribing the utilization of this model.

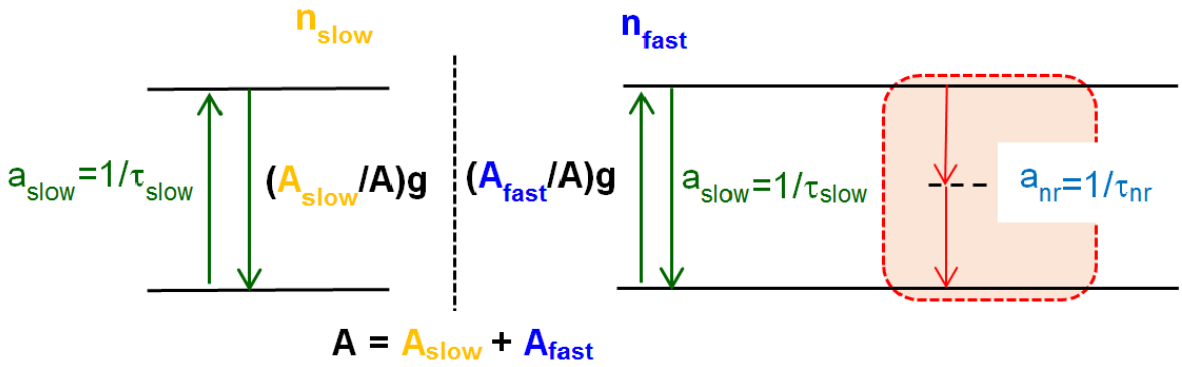

Figure 3.12: Schematic representation of two isolated spatial recombination processes in the sample that are photo-excited by laser with surface A. Radiative and mixed radiative and non-radiative recombination occur in surfaces A_{slow} and A_{fast} with characterized decay times τ_{slow} and τ_{fast}.

Now, we discuss more detail about the dynamic recombination in these two regimes. In the higher quality regime (region free of defects, or very weakly defective), the population of radiatively recombining excitons $n_{slow}(t)$ is obtained as:

$$\frac{dn_{slow}}{dt} = \frac{A_{slow}}{A} g(t) - \frac{n_{slow}}{\tau_{slow}} \tag{3.10}$$

where $g(t)$ is the generation rate of excitons, and $(A_{slow}/A)g$ represents the fraction of photo-generated excitons in the good quality material.

In the high defective region, defects act as non-radiative centers, which can be considered as predators for the preys (the excitons). We call N_{nrtot} and N_{nr} are the total density of non-radiative recombination centers and the occupied non-radiative recombination centers, respectively. The population of excitons $n_{fast}(t)$ in this region is affected by both the radiative recombination and the non-radiative recombination according to the following equation:

$$\frac{dn_{fast}}{dt} = \frac{A_{fast}}{A} g(t) - \frac{n_{fast}}{\tau_{slow}} - P_{capture}(N_{nrtot} - N_{nr}) n_{fast} \quad (3.11)$$

where n_{fast}/τ_{slow} is the radiative part, and $P_{capture}$ is the capture probability of excitons by a non-radiative recombination center.

The population of the occupied nonradiative recombination centers N_{nr} is determined by

$$\frac{dN_{nr}}{dt} = P_{capture}(N_{nrtot} - N_{nr}) n_{fast} - \frac{N_{nr}}{\tau_{nonrad}} \quad (3.12)$$

We remark that the TRPL is performed under low excitation conditions, so we assume here that $N_{nrtot} \gg N_{nr}$ which leads to a definition of the non-radiative recombination rate as

$$P_{capture}(N_{nrtot} - N_{nr}) \approx \frac{1}{\tau_{nonrad}} \quad (3.13)$$

Then

$$\frac{dn_{fast}}{dt} = \frac{A_{fast}}{A} g(t) - \frac{n_{fast}}{\tau_{slow}} - \frac{n_{fast}}{\tau_{nonrad}} \quad (3.14)$$

Combining the above equation and Eq. (3.9), we can write

$$\frac{dn_{fast}}{dt} = \frac{A_{fast}}{A} g(t) - \frac{n_{fast}}{\tau_{fast}} \quad (3.15)$$

The total PL intensity obtained by considering only radiative contribution of both populations is expressed as

$$I_{rad}(t) = A_{fast} \exp\left(\frac{-t}{\tau_{slow}}\right) + A_{slow} \exp\left(\frac{-t}{\tau_{slow}}\right) \quad (3.16)$$

At extremely low temperature, in general, we assume that IQE equals 100% that means electron-holes pairs in active region totally recombine radiatively. In this model, we consider not only contribution of radiative recombination but also contribution of non-radiative channels. Therefore, the IQE is defined as the ratio of the time-integrated intensity (Eq. 3.8) divided by the intensity corresponding to pure radiative recombination (Eq. 3.16):

$$IQE = \frac{\int_0^\infty I(t)}{\int_0^\infty I_{rad}(t)} = \frac{\int_0^\infty \left[A_{fast}\exp\left(\frac{-t}{\tau_{fast}}\right) + A_{slow}\exp\left(\frac{-t}{\tau_{slow}}\right)\right]}{\int_0^\infty \left[A_{fast}\exp\left(\frac{-t}{\tau_{slow}}\right) + A_{slow}\exp\left(\frac{-t}{\tau_{slow}}\right)\right]} = \frac{A_{fast}\tau_{fast} + A_{slow}\tau_{slow}}{(A_{fast} + A_{slow})\tau_{slow}} \qquad (3.17)$$

Carefully fitting the raw data in terms of the parameters of Eq. (3.8) we can fill the cells of Table III.4. Using this data and Eq. (3.17), we can calculate the average values of IQE for our samples and we find that they range from 50 to 57 % at 8 K.

When the temperature increases, the carriers become more mobile than at low temperature, therefore the assumption of isolated regions fails and cross talking between both regions is possible. To estimate the IQE at room temperature (IQE_{RT}) we utilize a scaling argument and we renormalize the value of IQE at low temperature (IQE_{LT}) by the evolution of the PL intensity with increasing temperature.

Let I_{LT} the low temperature value of the integrated PL intensity and let I_{RT} the room temperature value. Then:

$$IQE_{RT} = IQE_{LT} \cdot \frac{I_{RT}}{I_{LT}} \qquad (3.18)$$

The Arrhenius plots of the PL intensities versus reciprocal temperature are given in Fig. 3.6. From them we obtain the ratios $\frac{I_{RT}}{I_{LT}}$ and calculated the values of IQE_{RT}. The values of the IQE at room temperature also improve with increasing thickness of AlGaN layer, as reported in Table III.4.

It is worth reminding that the internal electric field split the wavefunction of electron and hole apart opposite sides of quantum well induces a reduction of the oscillator strength as shown in Fig. 3.9. Thus, it causes an increase of the radiative decay time that is proportional to the reverse of the oscillator strength. In the model of the IQE calculation at low excitation level, we assumed that the slow decay time τ_{slow} characterizes the radiative decay time. A good agreement between the evolution of the τ_{slow} and the reverse of the oscillator strength against the product of indium composition and the electric field in InGaN quantum well as plotted in Fig. 3.13 is a supporting evidence for the accuracy of this assumption.

Table III.4. Parameters of five samples obtained by fitting TRPL data at 8K using equation (1): τ_{fast}, τ_{slow} are the short and long decay times, respectively. Coefficients A_{fast} and A_{slow} relate to the strengths of dynamic kinetics correspond to τ_{fast}, τ_{slow}. IQE_{LT}, IQE_{RT} are the internal quantum efficiency at low temperature and room temperature that are calculated by using equation (10) and equation (11), respectively. I_{LT} and I_{RT} are the integrated photoluminescence at low and room temperature. Peak wavelength is the center of the photoluminescence spectra.

Sample	L_{AlGaN} (nm)	Peak wavelength (nm)	τ_{fast} (ns)	$\tau_{slow} = \tau_{rad}$ (ns)	$\frac{A_{slow}}{A_{fast} + A_{slow}}$	IQE_{LT} (%)	$\frac{I_{RT}}{I_{LT}}$	IQE_{RT} (%)
M_1	0	515	8.5	29.6	0.295	50	0.048	2.4
M_2	1.4	547	29.5	90.5	0.278	51	0.049	2.5
M_3	5.2	565	49.6	199.9	0.386	54	0.048	2.6
M_4	10.6	575	81.6	299.9	0.388	57	0.055	3.1
M_5	5.2	615	165.2	562.5	0.419	56.5	0.03	1.7

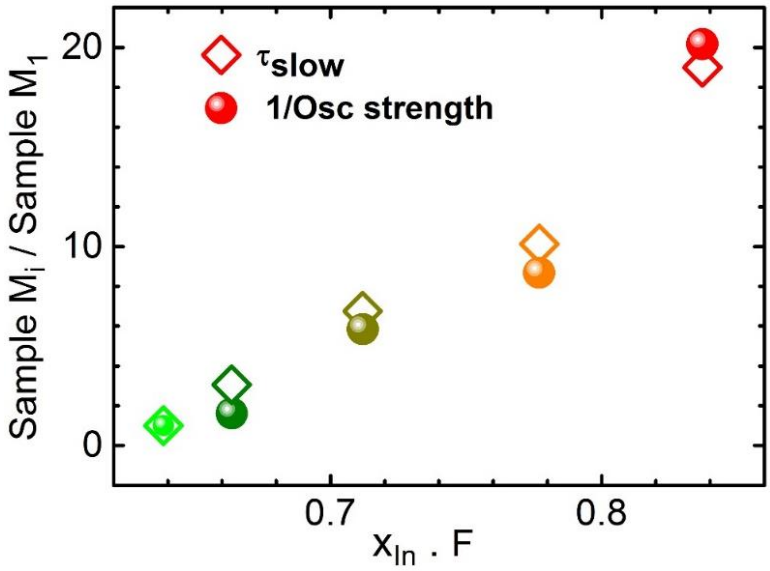

Figure 3.13. Evolution of the slow decay time (diamond) and the reverse of the oscillator strength (spheres) versus product of the indium composition and the internal electric field in the InGaN quantum well (normalized to the values corresponding to sample M_1).

3.3.2. Decay times and quantum confined Stark effect

The general observed trend is an increase of the radiative decay times with the emission wavelength as shown in Fig. 3.14. This is related to the increase of the QCSE due to the increase of either the AlGaN layer thickness or the indium composition, or both.

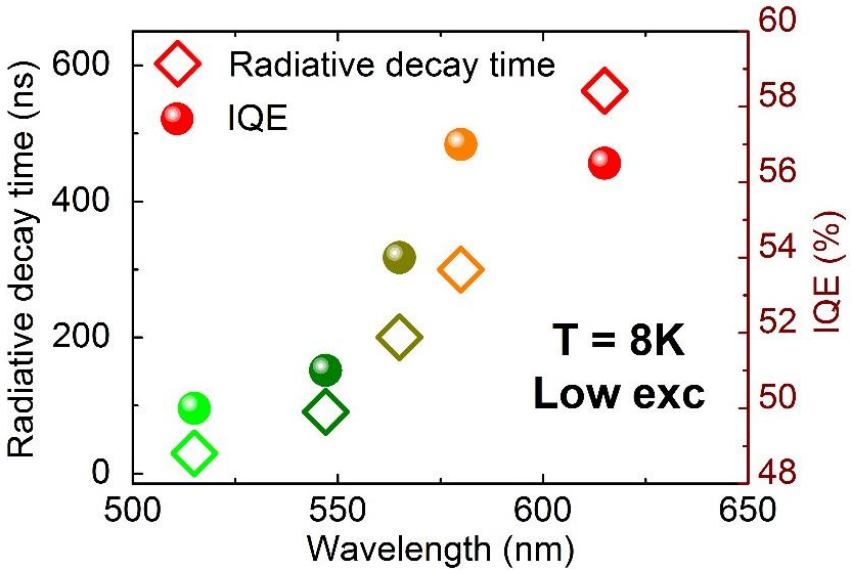

Figure 3.14. Radiative decay time (open diamonds) and internal quantum efficiency (spheres) as a function of the emission wavelength.

We observe also an increase of the non-radiative decay time when the AlGaN thickness increases (Fig. 3.15). Inserting an AlGaN inter-layer between InGaN and GaN, introduces a complementary tensile strain in the whole structure and reduces the elastic energy. This reduces the density of defects, which induces a reduction of the density of non-radiative recombination centers, and in turn this can explain the enhancement of the non-radiative decay. Even if the radiative decay time increases (due to the increase of the internal electric field), the non-radiative decay increase is larger. This explain the enhancement of the IQE with the increase of the AlGaN thickness.

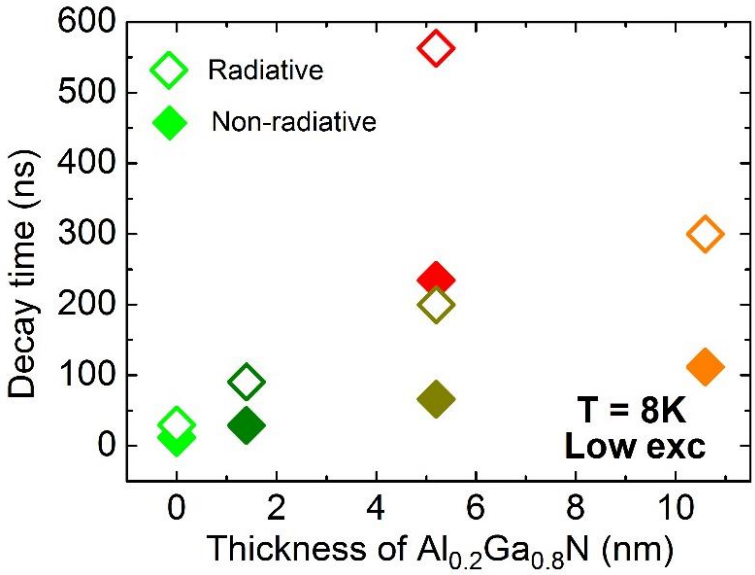

Figure 3.15 Evolution of decay times as a function of $Al_{0.2}Ga_{0.8}N$ thickness: open diamonds show radiative decay time and solid diamonds describe non-radiative decay time.

We now concentrate on the manifestation of the increase of the QCSE on electron and hole envelope functions. Under the influence of the internal electric field, the wave functions of electron and holes are pushed to opposite interfaces of the InGaN-based quantum wells. At constant well width, the higher the internal electric field, the smaller the overlap of the wave functions of electron and holes. This leads to a reduction of the radiative recombination rate or say using another phrasing, this increases the radiative decay time. On another hand, increasing indium composition enhances carrier localization, specially the hole[21,22] and hence prevents the carriers to migrate toward non-radiative recombination centers when the temperature increases. This contributes to strengthen the robustness of the PL intensity versus T. This is the commonly reported effect of the increase of the electric field: an enhancement of the opacity of the electronic density of charge at the InGaN-GaN interface. This suggest us to investigate how big the impact of such an enhancement can be in case of moderately strong photo-injection excitation as the electrostatic repulsion between electrons may hinder the radiative recombination in favor of intrinsic non-radiative Auger recombination processes.

3.4. Investigation of photo-induced non-radiative Auger recombination using power-dependent photoluminescence measurement

The power-dependent PL measurements were performed at 8 K. The samples were excited by the third harmonic of a Ti: sapphire laser at a wavelength of 266 nm with a laser spot surface estimated to 15 μm^2. The excitation power density of laser was changed from 1.2 x 10^{-2} to 3.7 x 10^3 W/cm^2. The light emitted by the samples was detected by using a back-illuminated CCD camera (Andor Newton 920).

3.4.1. The blue-shift of the PL under high photo-created carrier densities

Figure 3.16 displays the PL spectra of sample M_5 for different excitation power densities. The overall PL shapes of the samples do not change with the increase of excitation power. We observe a blue-shift of the PL peak when the excitation power density increases. This blue-shift increases from sample M_1 to sample M_5.

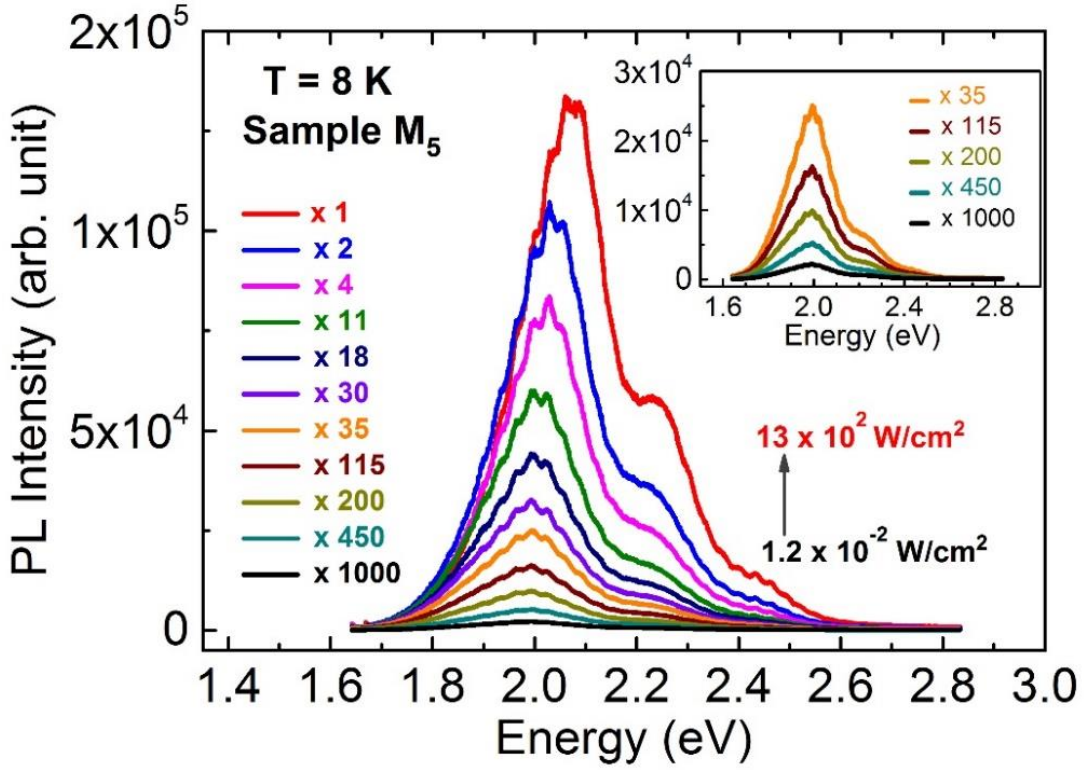

Figure 3.16. Evolution of the PL intensities at 8 K versus power excitation for sample M_5. The PL spectra are multiplied by factors: x1000, x450, etc. when excitation power density increases from 1.2 x 10^{-2} to 13 x 10^2 W/cm^2. Inset: zoom for the spectra at low photo-excitation densities range.

A similar trend was earlier reported for many zinc blende heterostructures grown along the <111> direction.[23] The origin of this blue-shift was explained by combination of Coulomb screening effect of internal electric field[24] and phase-space filling of inhomogeneous effective potential[25]. It is well known that, under a high internal electric field, electron and hole wavefunctions are strongly localized at quantum well interfaces. When photo-generated carrier density increases, it produces a photo-induced dipole that counterbalances the influence of the electric field. In the simplest model of a point charge of density σ, this field writes as $E_{photinducted} = \frac{\sigma}{\varepsilon_0 \varepsilon_r}$, where ε_r is the relative dielectric constant of the material. This simple text book model permits to grasp how the competition between the photon induced field and the photo-created one leads to a blue shift of the transition. The actual situation is more complex to calculate as it requires using the exact charge densities of electron and hole and to self-consistently solve coupled Poisson and Schrödinger equations. Instead of a linear dependence of the electric field with σ, whatever σ, one progressively reaches a sub-linear dependence or even a more complicated situation when more than one conduction or valence states are involved. In the simplest case of one

confined sub-band for the electrons and holes and for moderate injection conditions, the internal electric field flattens, leading to an energy blue-shift grossly equal to the product of the electric field time the well-width, increasing the overlap between electron and holes envelope functions and making the Coulomb interaction to be enhanced (this contribution gives birth to a red-shift). The competition between reduction of QCSE and increasing of exciton binding energy gives a blue-shift. We have here to remind that exciton binding energy under high enough injection conditions so that the integrated potential line-up has got flat is lower than the value obtained using a square well calculation. The reasons for this are immediately found in expressing the Coulomb interaction in the reciprocal space. By definition, the exciton state is built from the empty crystal by removing one electron from the valence band and promoting its energy to an empty state of the conduction band, thus creating a hole state in the valence band. The wave function of both the electron and hole of the exciton both expand along the allowed states (they have to be empty states, according with Pauli's exclusion principle) of the conduction and valence bands. In case of an un-doped semiconductor, these expansions start from wave vectors at zone center up to the upper limits of the Brillouin zone. When the semiconductor is doped (for example n-type), the expansion of the hole wave functions along valence band states is unchanged BUT the expansion of the electron one start at k_F in the phase space, where k_F is the Fermi wave vector, which values depend on the doping. Thus, the kinetic energy interacting electron hole pair is higher than for the undoped situation. This leads to a compensation of the negative Coulomb terms. In case of a photo injection Fermi vectors vary with the pump power, so do the expansions, and also the excitonic binding energy. The flattening of the band leads to an increase of the binding energy, phase space filling effects lead to a decrease. The total effect results of the balancing contribution of both phenomena.[26,27]

Under much higher conditions (not reached here) screening of the dielectric constant may be induced leading to a red-shift of the optical transitions due to a renormalization of the bandgap of the confining material. This electrostatic density of charge being lower in the barrier layers renormalization is then weaker there and we face a situation of non-rigid renormalization of the band line-ups. High excitation conditions make the dielectric constant to increase, which decreases the Coulomb interaction. Of course, beyond the frame of this qualitative description a more complicated theoretical approach is required to calculate all these contributions that includes considering the out of plane components of the electron and hole wave vectors as well as phase space filling

effects; so many contributions that investigation is out of the scope of our experimental work.

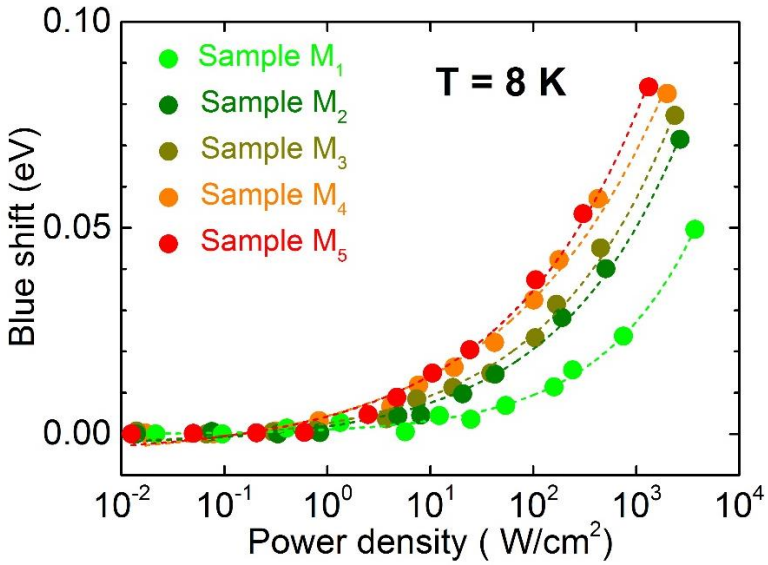

Figure 3.17. The blue shift of all samples plotted as a function of logarithmic of the excitation density. The blue shift decreases from sample M_5 to sample M_4, to sample M_3, to sample M_2, and to sample M_1.

As expected from the simplest of the modeling, we obtain larger blue-shift for stronger internal electric field samples as shown in Fig.3.17. It is interesting to notice that we find a larger blue-shift for sample M_5 in comparison with sample M_4, although internal electric field of sample M_5 (3.7 MV/cm) is estimated smaller than that of sample M_4 (4.0 MV/cm), which corresponds to a smaller potential drop through the quantum well layers. This is not easy to interpret**. We are here facing samples with quantum wells of strongly inhomogeneous bandgaps caused by both inhomogeneities of well widths and fluctuations of the alloy composition** (we are sitting near x_{In}= 0.21). We remark that as all samples grown with similar quantum well thicknesses, the larger blue-shift of sample M_5 is probably caused by fluctuations of the indium content in the well layer which are larger for x_{In} = 0.23 than for x_{In}= 0.21. This may be related to a stochastic statistical binomial alloy disorder. We however have to consider that differences of lattices constant and thermal stability of InN and GaN may also be impacting the growth and the texture of the alloy at the nanoscale beyond prediction of probabilities. When indium content is not homogeneous within quantum well layers, generated electron-holes pairs are localized to local minimum potential. When increasing the photo-injection density, the exclusion principle of Pauli and population effects impose to the wave functions of the carriers to delocalize towards empty high energy regions that are progressively filled with carriers.

The different contributions to the blue-shift that compete are very much depending on the sample design and on the nanostructure of the InGaN alloy.

To summarize, the blue-shift of the InGaN QW PL transition when the excitation power density increases can be explained by 3 phenomena: screening of the internal electric fiel by the photo-created carriers, phase space filling, and carrier delocalization from potential fluctuations.

3.4.2. Experimental evidence of Auger non-radiative recombination

The non-radiative Auger recombination that we will consider here is a three-particle interaction that occurs between two electrons and one hole or one electron and two holes. In such process, the energy resulting from the recombination of an electron-hole pair is transferred to an electron (nnp mechanism) or to a hole (ppn mechanism) instead of interacting with the electromagnetic field for further being exported outside the crystal and being detected as a photon. This is thus an intrinsic non-radiative recombination process where the particle that receives this excess energy jumps toward an excited state and further relaxes it via a more or less complex interaction with the phonon field. The Auger recombination becomes a dominant process when the probability of carrier collision is substantial, which is the case in heavily doped material or under high carrier injection condition.

K. D. Glinchuk et al. demonstrated that changing of evolution of integrated PL intensity versus excitation power from a linear to a sub-linear dependence resulted by competition between radiative and non-radiative recombination channels and can be interpreted to Auger recombination.[28] In our samples, point defects and dislocations can be also efficient non-radiative recombination centers, of extrinsic origin. Their contributions will be treated within the context of the Shockley-Read-Hall (SRH) model for extrinsic non-radiative recombination centers. In this framework, the SRH non-radiative recombination rate is proportional to both the electron and hole densities timed by "ad-hoc" coefficients which probe the efficiencies of the non-radiative centers (or crystalline quality).

The total non-radiative recombination rates may be written in terms of the products of the populations of electrons and holes n and p as:

$$NR_{tot} = an + bp + cnnp + dppn \quad (3.19)$$

While the radiative recombination rate is proportional to the product of the populations of electron and holes:

$R_{tot} = e\ np$ (3.20)

Photo-excitation generates the same numbers of electrons and holes. At an excitation power P let $\nu(P)$ this number. Then $n(P) = \nu(P) + n0$ and $p(P) = \nu(P) + p_0$ where n_0 and p_0 respectively represent the amounts of residual electrons and holes in the darkness. Based on such considerations the integrated PL intensity which varies like R_{tot}/NR_{tot} proportion with excitation will behave sub-linearly beyond an excitation threshold as in this fraction, the numerator R_{tot} asymptotically varies like $\nu(P)^2$ when the denominator NR_{tot} asymptotically varies like $\nu(P)^3$.

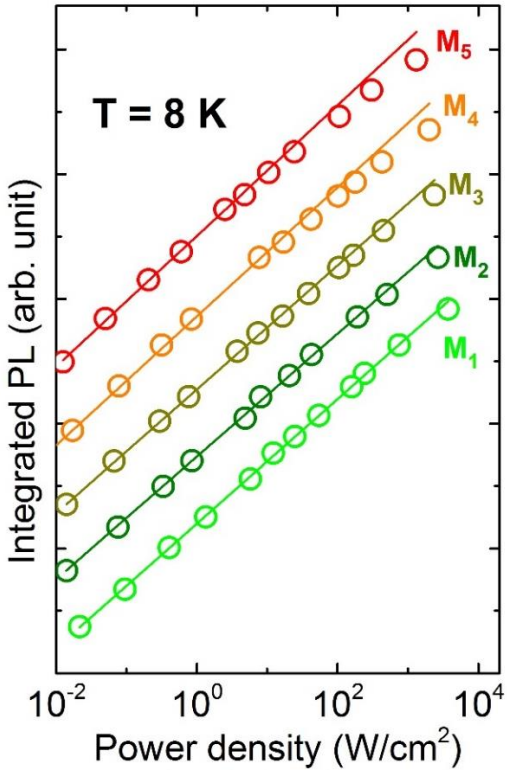

Figure 3.18. Logarithm plots of the PL intensities against the excitation power density. The unity slopes are changed to smaller ones beyond an excitation threshold that is changing from sample to sample.

Figure 3.18 shows that when increasing the excitation power, the slope of the variation of the integrated PL intensities changes from a linear to a sub-linear one beyond a certain threshold power density P_T. P_T decreases with increasing the thickness of AlGaN layer and with the increase of the indium composition as listed in Table III.5. This measurement indicates that the internal electric field significantly impacts the Auger

recombination process. This indicates that the onset of Auger effect is correlated with the accumulation of carriers (in particularly electrons) at interfaces: the higher the internal electric field, the more efficient the accumulation, the lower P_T.

We emphasize that we observe here a similar trend for the evolution of the blue-shift and the onset of Auger effect of sample M_5: the corresponding value of P_T, is smaller than its value of sample M_4 although sample M_5 has smaller internal electric field. We also remind that sample M_5 was grown with lower growth temperature than other samples to get higher indium content in the quantum well. This process induces higher fluctuations of indium composition in the active region of sample M_5. C. K. Wu et al.[29] demonstrated that the higher the fluctuations of the indium content the higher the local accumulation of carriers, hence the stronger the Auger recombination.

Table III.5. Characteristic parameters of the samples: x_{In} is the indium composition. L_{InGaN}, $L_{AlGaN,}$ and L_{GaN} are the widths of the well layers InGaN and $Al_{0.2}Ga_{0.8}N$ and GaN barrier layers, respectively. F and P_T correspond to values of the electric field and the experimental threshold excitation densities for the onset of transition from the linear to sublinear dependence of the integrated photoluminescence intensity versus pump power.

Sample	x_{In}	L_{InGaN} (nm)	L_{AlGaN} (nm)	L_{GaN} (nm)	F ($MVcm^{-1}$)	P_T (W/cm^2)
M_1	0.21	2.6	0	15.2	2.9	500
M_2	0.21	2.6	1.4	15.6	3.1	200
M_3	0.21	2.6	5.2	11.9	3.5	40
M_4	0.21	2.6	10.6	7.0	4	10
M_5	0.23	2.6	5.2	11.9	3.7	4

3.4.3. Impact of internal electric field on IQE

In this section, the power-dependence of internal quantum efficiency (IQE) is discussed in terms of our experimental results and using a simulation. We find a trend that IQE of all samples shapes as a plateau value at low injection conditions and then reduces under high injection conditions. The reduction of IQE is stronger for samples with higher internal electric field.

The IQE is calculated from experiment conditions via the integrated PL intensity I, the light extraction efficiency η and the generation rate, G, as following equation[30]

$$IQE = \frac{I}{\eta.G}, \quad (3.21)$$

The constant value of η is determined from values of I, and IQE at low excitation level.

The values of the generation rate G were calculated directly from experimental conditions

$$G = \frac{P_{laser}(1-R)\alpha}{A_{spot}(h\upsilon)} \quad (3.22)$$

where P_{laser} is the incident laser power, R is the reflection coefficient at the semiconductor to air interface, α is the absorption coefficient of the light in the semiconductor, hυ is the incident photon energy, A_{spot} is the surface of the laser spot.

The carrier density is extracted from experimental value of the IQE, the generation rate and the radiative decay time by equation:

$$n = IQE.G.\tau_{rad}, \quad (3.23)$$

We have to remind here that, the values of IQE and τ_{rad} of sample M_1 to sample M_5 are listed in Table III.4.

The evolution of the IQE versus pump power is plotted using spheres in Fig. 3.19(a). It clearly shows that, when comparing samples having the same indium content, but with different electric fields in the active regions, the onset of efficiency droop occurs at lower excitation densities for the samples having a higher internal electric field. We remind that the higher internal electric field, the more dramatic the impact of QCSE for increasing the radiative decay times. Therefore, at a given P_{laser}, the density of photo-generated carriers is higher in sample M_5 than others as reported in Fig. 3.19(b) due to the dominant influence of the variation of τ_{rad} over α in Eq. (3.22) and Eq. (3.23). The number of electron-electron collisions which increases with the third power of the carrier density (~n^3) favours the promotion of excess electronic energy and eventual electronic escape away from the active region.[31,32]

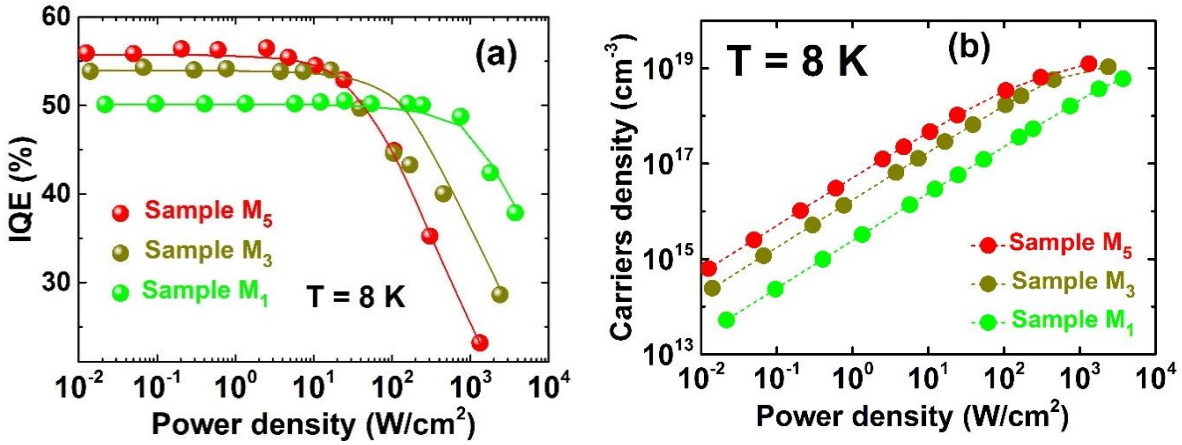

Figure 3.19. (a) Evolution of the normalized experimental values of IQE (spheres) of all samples plotted as a function of excitation power density. Fitting curves are represented as solid lines. (b) Evolution of photo created carrier density as a function of excitation power density of all samples.

We wish to bring our experimental results in harmonic concert with the predictions of a theoretical model easy to handle and world-widely accepted by experimentalists: the ABC model. To do so, we have to estimate the contribution of Shockley-Read-Hall nonradiative recombination, the radiative recombination, and Auger nonradiative recombination by fitting the experimental values of IQE. As our samples have been grown in conditions of a residual n-type doping, we have to use a modified version of the ABC model that includes this residual n-type doping.

In this context, under steady-state excitation conditions, the generation rate can be determined by expression.[33]

$$G = \frac{n(n+n_0)}{\tau_n n + \tau_p(n+n_0)} + Bn(n+n_0) + C_n n(n+n_0)^2 + C_p n^2(n+n_0), \qquad (3.24)$$

where n is the excess of photo-created electron (or hole) density (cm^{-3}), n_0 is the residual doping (cm^{-3}), τ_n and τ_p are the minority carrier lifetimes for the n-type and p-type semiconductor respectively, B, C_n and C_p are the coefficients of radiative recombination, nnp-Auger, and npp-Auger recombination, respectively.

In the absence of residual doping, the coefficient of Shockley-Read-Hall non-radiative recombination is defined as $A = (\tau_n + \tau_p)^{-1}$. By making the standard approximation that $\tau_n = \tau_p$, we have $\tau_n = \tau_p = 1/(2A)$.

Galler et al. demonstrated in Ref. 33 that the efficiency droop is dominated by nnp-type Auger recombination rather than npp-type for an n-type InGaN material. Therefore, we assume here that $C_p = 0$ for our n-doped samples.

Then the generation rate in Eq. (3.24) can be rewritten by a much simpler equation than before:

$$G = \frac{2An(n+n_0)}{2n+n_0} + Bn(n+n_0) + C_n n(n+n_0)^2 \quad (3.25)$$

Then theoretical IQE becomes:

$$IQE = \frac{Bn(n+n_0)}{G}, \quad (3.26)$$

The fitting curves (theoretical IQE) are displayed in Fig. 3.19(a) as solid lines. We find a decreasing trend for all the coefficients A, B, and C with the decrease of the emission energy (Fig. 3.20).

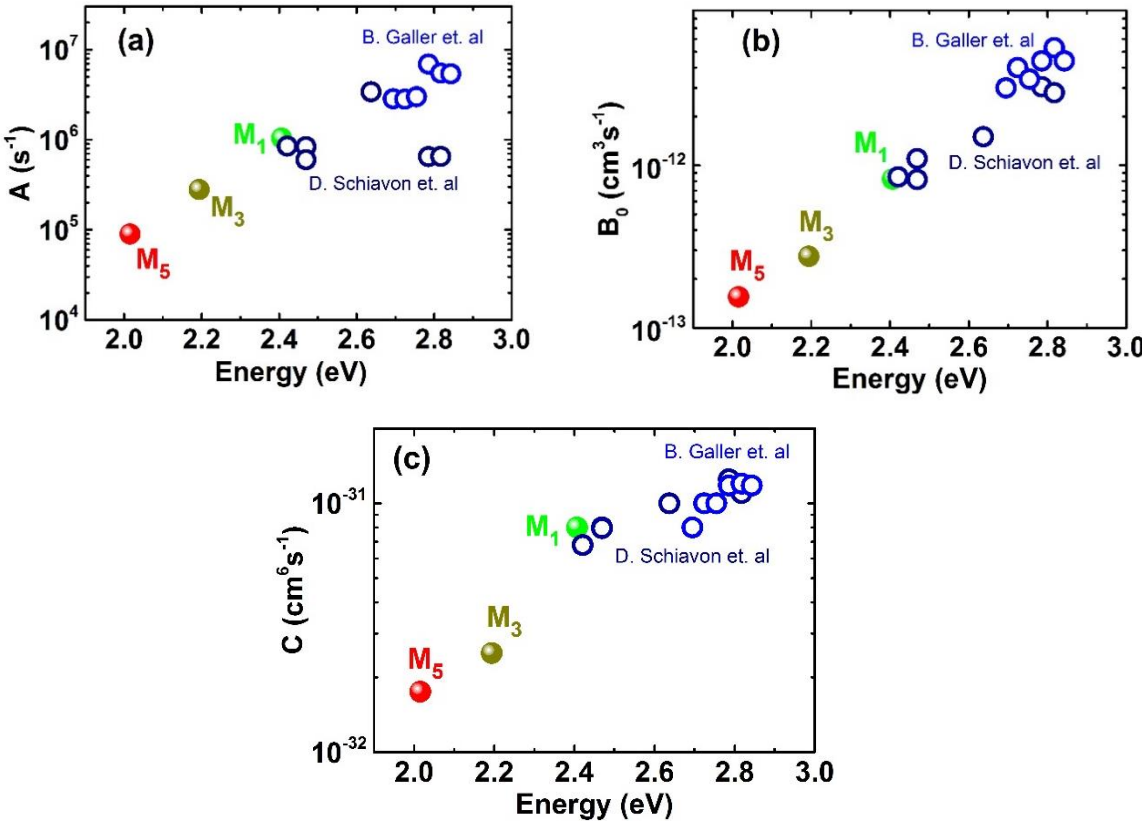

Figure 3.20. The evolution of logarithmic of coefficients A, B and C versus emission energy. The spheres correspond to the data of our samples. The circles represent the data reported by D. Schiavon et al.[34] and B. Galler et al.[35]

As we demonstrated earlier in part 3.1, lattice-matching of a GaN-InGaN-AlGaN three-material structure to GaN can be obtained by correctly designing the thickness of the different layers. This gives a reduction of the defect density related to the built-in strain field and hence an improvement of the crystalline quality. We previously clearly correlated the enhancement of the room temperature and low temperature PL intensities with the reduction

of defect densities by adding an AlGaN strain-compensating layer[4,13]. This contributes here to the decrease of the value of A from samples M_1 to M_5. We have also to remind that the indium composition increases from sample M_1 to sample M_5, which leads to deeper localization potentials[36,37] and prevents the escape of the carriers out of the active parts of the MQWs. Both contributions decrease the values of A from sample M_1 to sample M_5: $A_{M1} > A_{M3} > A_{M5}$.

The increase of the internal electric field reduces the electron and hole wave functions overlap from sample M_1 to sample M_5 and subsequently increase the radiative decay time τ_{rad}. This leads to $B_{M1} > B_{M3} > B_{M5}$. David and Grundmann[38,39] have studied the evolution of B with electron densities and they have shown that, in case of blue light emitters, it decreases at high densities (larger than10^{18} cm^{-3}). We have decided to reduce here value of B with carrier density by a form $B(n) = B_0 / [1+(n/n_{psf})^{\gamma}]$, as plotted in Fig. 3.21(a) where B_0 is value of coefficient B at low excitation density[40] (spheres in Fig. 3.20(b)), n_{psf} = 2 x 10^{19} cm^{-3} is the carrier density for the onset of phase-space filling effect, γ = 0.82 is a dimensionless exponent.[41] Moreover, under high excitation condition, the Coulomb interaction of carrier increase that cause a reduction in decay time of samples, as shown in Fig. 3.21(b).[38]

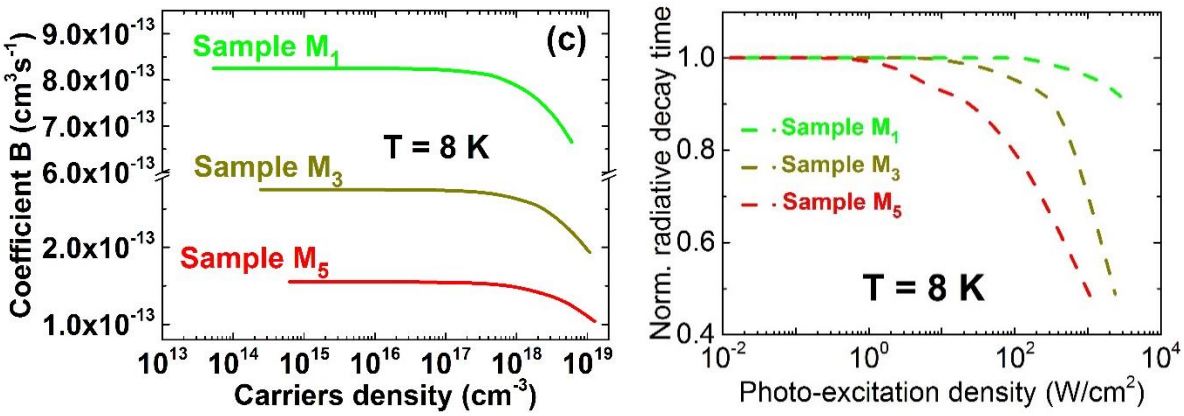

Figure 3.21. (a) Evolution decay time of all samples with the power density. (b) Carrier density as a function of the power density; Dotted lines are the eyes guidance. (c) Evolution of the coefficient B as a function of the carrier density.

Regarding to the values of C, there is a correlation with the values of B as sketched in Fig. 3.22 where we have also reported the data collected by Weisbuch et al.[39,42-44] and the data of Schiavon et al.[34], and Galler et al.[35]. This indicates that the values of C can be framed with an approximation using a scaling argument and from the values of B obtained by TRPL spectroscopy. The localization phenomena have a dominating impact at the scale of the

radiative decay time that is to say at the scale of the radiative recombination rate. We can thus reasonably anticipate from our experimental results of their determinant impact at the scale of the intrinsic non-radiative Auger recombination. It is proportional to cubic of carrier density (~n^3) in the samples. The Fig 3.19(b) shows that the carrier density in the sample M_5 is approximately 10 times or 3 times larger than in the M_1 or in the M_3 samples. Therefore, non-radiative Auger recombination in the red sample is much stronger than in the two other samples even if the value of the coefficient C is smaller in the red sample.

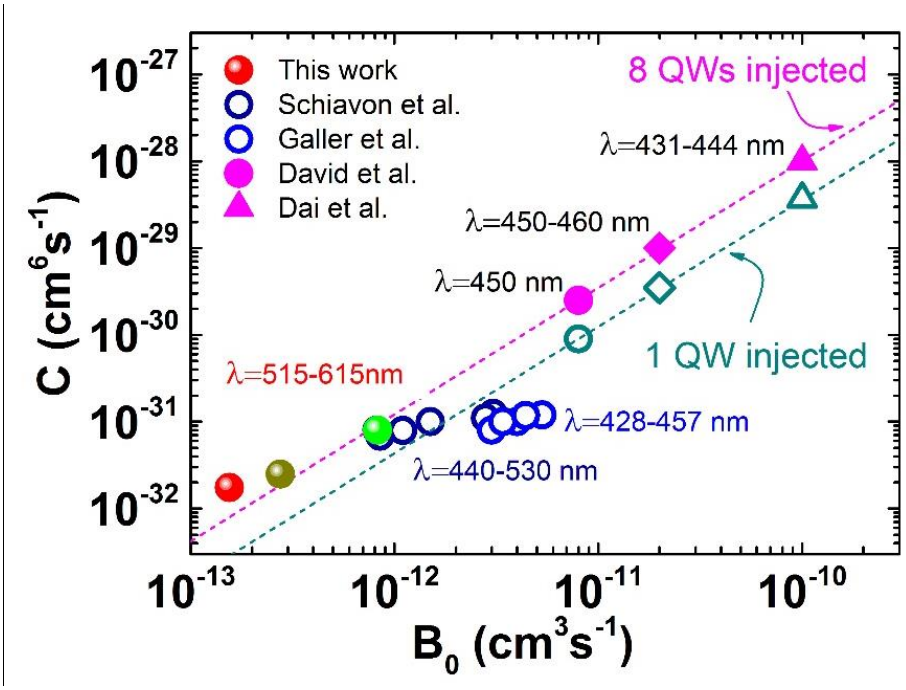

Figure 3.22. Evolution of coefficient C as a function of coefficient B in case of only one or multi-quantum well injected. Circles show values of B in case of single QW.[34,35] Spheres represent data of multi-quantum well.[39,42-44]

As the values of the coefficients A, B, and C are dominantly ruled at different scales by the internal electric field: overlap of electron and hole wave functions, localization near interfaces which favours the collisions between particles of identical charges, we find that the onset of efficiency droop occurs at lower photo excitation densities when the QW emission wavelength increases. This is correlated to the enhancement of the internal electric field in the active part. QCSE plays in concert with the localization of carriers in energetically favourable regions of the QWs.

However, besides a good agreement between our data and the compilation made by Weibuch et al. for multiple quantum wells, we also observe a scattering in the set of data published by Schiavon et al.[34] and Galler et al.[35] for single quantum wells. It motivates us for

investigating the impact of Auger effect on the internal quantum efficiency in a series of single quantum wells. We will keep working in the same bandgap energy region of the material since we are always working with an In composition of 0.21-0.23.

References

1. T. Shioda, H. Yoshida, K. Tachibana, N. Sugiyama, and S. Nunoue, Phys. Status. Solidi (a) **209**, 473 (2012)
2. S. Saito, R. Hashimoto, J. Hwang, and S. Nunoue, Appl. Phys. Express **6**, 111004 (2013)
3. J.-I. Hwang, R. Hashimoto, S. Saito, and S. Nunoue, Appl. Phys. Express **7**, 071003 (2014)
4. K. Lekhal, B. Damilano, H. T. Ngo, D. Rosales, P. de Mierry, S. Hussain, P. Vennéguès, and B. Gil, Appl. Phys. Lett. **106**, 142101 (2015)
5. S. Nakamura, T. Mukai, and M. Senoh, Jpn. J. Appl. Phys. **32**, 16 (1993)
6. P. A. Grudowski, C. J. Eiting, J. Park, B. S. Shelton, D. J. H. Lambert, Appl. Phys. Lett. **71**, 1537 (1997)
7. S. Keller, S.F. Chichibu, M.S. Minsky, E. Hu, U.K. Mishra, S.P. DenBaars, J. Crys. Growth **195**, 258 (1998)
8. B. Damilano, H. Kim-Chauveau, E. Frayssinet, J. Brault, S. Hussain, K. Lekhal, P. Vennéguès, P. De Mierry, and J. Massies, Appl. Phys. Express **6**, 092105 (2013)
9. D. Gerthsen, E. Hahn, B. Neubauer, V. Potin, A. Rosenauer, and M. Schowalter, Phys. Status Solidi C **0**, 1668-1683 (2003)
10. H. Zhao, G. Liu, X. H. Li, G. S. Huang, J. D. Poplawsky, S. T. Penn, V. Dierolf, and N. Tansu, App. Phys. Lett. **95**, 061104 (2009)
11. Light emitting diodes-E. Fred Schubert- Cambridge University Press-2003
12. J. Abell, and T. D. Moustakas, Appl. Phys. Lett. **92**, 091901 (2008)
13. T. H. Ngo, B. Gil, P. Valvin, B. Damilano, K. Lekhal, and P. de Mierry, Appl. Phys. Lett. **107**, 122103 (2015)
14. G.-E. Weng, W.-R. Zhao, S.-Q. Chen, H. Akiyama, Z.-C. Li, J.-P. Liu, and B.-P. Zhang, Nanoscale Research Letters (2015) 10:31
15. H. P. D. Schenk, M. Leroux, and P. de Mierry, J. Appl. Phys. **88**, 1525 (2000)

16. Y. -H. Cho, G. H. Gainer, A. J. Fischer, J. J. Song, S. Keller, U. K. Mishra, and S. P. DenBaars, Appl. Phys. Lett. **73**, 1370 (1998)
17. I. Gorczyca, S. P. Lepkowski, T. Suski, N. E. Christensen and A. Svane, Phys. Rev. B. **80**, 075202 (2009)
18. A. Morel, P. Lefebvre, S. Kalliakos, T. Taliercio, T. Bretagnon, and B. Gil, Phys. Rev. B. **68**, 045331 (2003)
19. P. Bigenwald, P. Lefebvre, T. Bretagnon, and B. Gil, Phys. Stat. Sol. (b) **216**, 371 (1999)
20. Y. Iwata, R. G. Banal, S. Ichikawa, M. Funato, and Y. Kawakami, J. Appl. Phys. **117**, 075701 (2015)
21. L. Bellaiche, T. Mattila, L. W. Wang, S. H. Wei, and A. Zunger, Appl. Phys. Lett. **74**, 1842 (1999)
22. P. Dawson, S. Schulz, R. A. Oliver, M. J. Kappers, and C. J. Humphreys, J. Appl. Phys. **119**, 181505 (2016)
23. P. Boring, B. Gil, and K. J. Moore, Phys. Rev. Lett. **71**, 1875 (1993)
24. I. Akasaki and H. Amano, J. Appl. Phys. **36**, 5393 (1997)
25. S. Chichibu, T. Azuhata, T. Sota, and S. Nakamura, Appl. Phys. Lett. **69**, 4188 (1996)
26. P. Bigenwald, A. Kavokin, B. Gil, and P. Lefebvre, Phys. Rev. B **61**, 15621 (2000)
27. P. Bigenwald, A. Kavokin, B. Gil, and P. Lefebvre, Phys. Rev. B **63**, 035315 (2001)
28. K. D. Glinchuk, A. V. Prokhorovich, and V. I. Vovnenko, Phys. Status Solidi A **54**, 121 (1979)
29. C. K. Wu, C. K. Li, and Y. R. Wu, J. Comput. Electron. **14**, 416 (2015)
30. Q. Dai, M. F. Schubert, M. H. Kim, J. K. Kim, E. F. Schubert, D. D. Koleske, M. H. Crawford, S. R. Lee, A. J. Fischer, G. Thaler, and M. A. Banas, Appl. Phys. Lett. **94**, 111109 (2009)
31. J. Iveland, L. Martinelli, J. Peretti, J. S. Speck, and C. Weisbuch, Phys. Rev. Lett. **110**, 177406 (2013)
32. J. Peretti, C. Weisbuch, J. Iveland, M. Piccardo, L. Martinelli, and J. S. Speck, Proc. SPIE. **9003**, 90030Z (2014)
33. B. Galler, H. J. Lugauer, M. Binder, R. Hollweck, Y. Folwill, A. Nirschl, A. Gomez-Iglesias, B. Hahn, J. Wagner, and M. Sabathil, Appl. Phys. Express **6**, 112101 (2013)
34. D. Schiavon, M. Binder, M. Peter, B. Galler, P. Drechsel, and F. Scholz, Phys. Status Solidi B **250**, 283 (2013)

35. B. Galler, P. Drechsel, R. Monnard, P. Rode, P. Stauss, S. Froehlich, W. Bergbauer, M. Binder, M. Sabathil, B. Hahn, and J. Wagner, Appl. Phys. Lett. **101**, 131111 (2012)
36. M. Filoche, and S. Mayboroda, PNAS **109**, 14761 (2012)
37. T.-J. Yang, R. Shivaraman, J. S. Speck, and Y.-R. Wu, J. Appl. Phys. **116**, 113104 (2014)
38. A. David, and M. J. Grundmann, Appl. Phys. Lett. **96**, 103504 (2010)
39. A. David, and M. J. Grundmann, Appl. Phys. Lett. **97**, 033501 (2010)
40. J. Hader, J V. Moloney, and S W. Koch, Appl. Phys. Lett. **87**, 201112 (2005)
41. E. Kioupakis, Q. Yan, D. Steiauf, and C. G Van de Walle, New J. Phys. **15**, 125006 (2013)
42. C. Weisbuch, M. Piccardo, L. Martinelli, J. Iveland, J. Peretti, and J. S. Speck, Phys. Status Solidi A **212**, 899-913 (2015)
43. D. A. Zakheim, A. S. Pavluchenko, D. A. Bauman, K. A. Bulashevich, O. V. Khokhlev, and S. Yu. Karpov, Phys. Status Solidi A **209**, 456 (2012)
44. Q. Dai, Q. Shan, J. Wang, S. Chhajed, J. Cho, E. Fred Schubert, Mary H. Crawford, Daniel D. Koleske, M.-H. Kim, and Y. Park, Appl. Phys. Lett. **97**, 133507 (2010)

CHAPTER IV

INTERNAL QUANTUM EFFICIENCY IN InGaN/GaN SINGLE QUANTUM WELL EMITTING FROM BLUE TO RED-LIGHT

The analysis of the results presented in the chapter III is somewhat limited in the sense that we don't exactly know the photo-created carrier density in each QW, this density can vary from one quantum well to another one. Indeed, laser light is exponentially absorbed as a function of the InGaN/GaN thickness. Furthermore, it is also possible that the thickness of the InGaN QW evolves (non-intentionally) from the first to the last QW as shown in Fig. 4.1. One way to eliminate these uncertainties is to study a single QW instead of a MQW. Therefore, we propose in this chapter to study the optical properties of blue to red-emitting **single** QWs, seen Fig. 4.2.

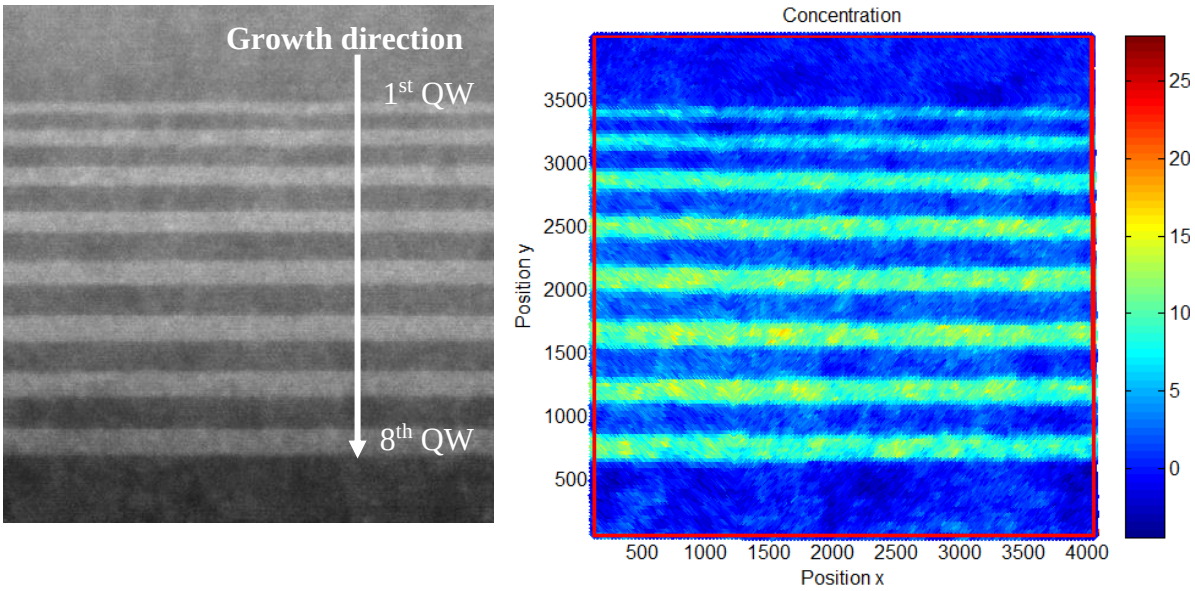

Figure 4.1. A typical TEM images of an 8-period multiple quantum well structure. *Courtesy from Pierre Ruterana and his PhD student, Chery Nicolas.*

In this chapter, the effects of quantum confined Stark effect (QCSE) and carrier localization on internal quantum efficiency (IQE) are investigated by means of photoluminescence (PL) measurements. Spontaneous and the piezoelectric polarizations produce an internal electric field in InGaN/GaN heterostructures grown along the polar orientation.[1,2] This is not only impacting the radiative recombinations but also the non-

radiative recombinations.[3-5] The electronic wavefunction is narrower for a QW with electric field than without. Then, for a same generation rate and recombination rate, the localized electron density is higher in the QW with electric field. This electric field reduces the overlap of electron and hole wave-functions. This reduces the radiative recombination rate and it may also promote Auger non-radiative recombinations.[6] It has been pointed out some time ago that the IQE of InGaN-based LEDs is the highest for the blue region. Hence this quantity reduces when the light emission shifts to longer wavelengths.[7-9] A strong internal electric field blocks carriers of given charges at heterointerfaces, which impacts the efficiency of carrier-carrier repulsion and hence triggers the onset of Auger effect at lower excitation densities than a weak electric field would do.[10, 11]

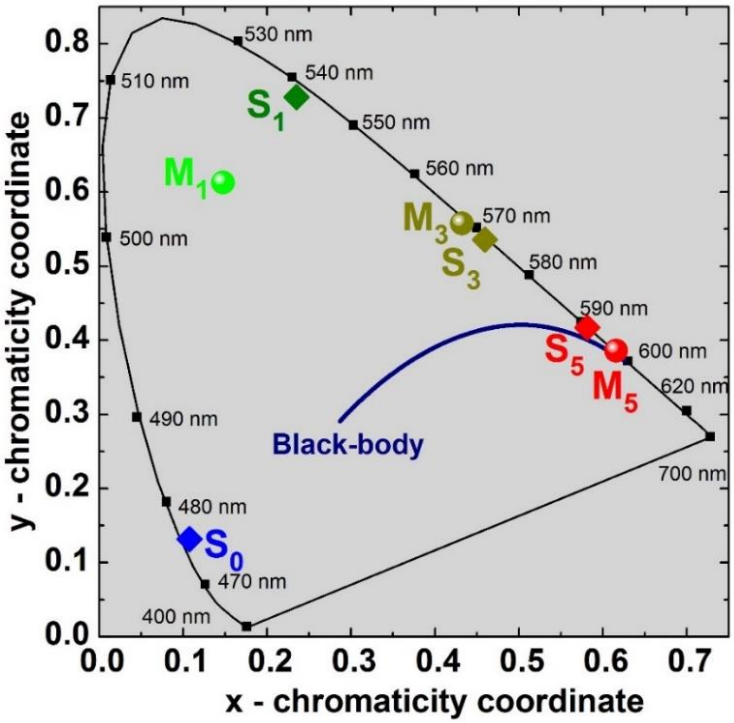

Figure 4.2. Projection of the 8K photoluminescence features of single quantum well samples and of the multiple quantum well into the CIE-1978 convention chromaticity diagram. The solid line is the radiation curve of the black-body.

In our samples, the confining material is a ternary alloy: InGaN. As we discussed in chapter II, it is an alloy with randomly distributed gallium and indium atoms, leading to fluctuations of indium composition in complement to the fluctuations of quantum well thickness. This favours carrier localization in some potential minima in indium-rich part of the confining layers or/and in wide well regions.[12-15] The carrier localization prevents carriers to migrate toward non-radiative recombination centers. Thus, it improves the internal

quantum efficiency (IQE) by limiting the influence of non-radiative recombination to defects, but it also leads to a more efficient non-radiative Auger recombination.[16] So the conditions of occurrence of the different non-radiative recombination mechanisms (Shockley-Read-Hall and Auger) are thus complex functions of joint contribution of the internal electric field, of the localization of carriers to interfaces and to indium rich regions.

To enhance the IQE, it requires elucidating the origins of the mechanisms of droop efficiency and to eventually cure them. After long standing debates in the literature,[17-19] Auger non-radiative recombination has been demonstrated as being the principal mechanism for the reduction of IQE under high excitation condition in the InGaN-based blue light emitters.[20-23] Radiative recombination is proportional to the product of electron and hole populations whilst Auger recombination is a three-particle interaction mechanism, which makes it proportional to the third power of the carrier density and very much tunable by means of an optical excitation.

4.1. Experimental details

4.1.1. Growth process of samples

In this study, a series of single quantum wells (SQWs) structure with different designs are examined: growth with or without AlGaN strain-compensating interlayers, changing indium composition, eventually increasing QW thickness. Adding an AlGaN interlayer can help to compensate the lattice mismatch; which is very good to reduce the dislocation density in MQWs, but it also increases the electric field internal to the QW layer.[24-26] The indium content variation can give us access to different degrees of carrier localization in indium-rich regions of the samples. Different QW widths allow us to examine the impact of the quantum confined Stark effect. These samples emit light in a broad wavelength range of the visible spectrum and are named as S_0, S_1, S_3, S_5 for the blue, green, yellow and red-light emitting, respectively. Note that the notations here are chosen as the same as the notations of MQW samples for similar emission WL.

Figure 4.3 below illustrates the design of the samples which are discussed here. All the samples are grown by metal organic chemical vapor deposition (MOCVD). Trimethylgallium (TMG) or triethylgallium (TEG), trimethylindium (TMI) and ammonia (NH_3) are used as precursors for gallium, indium and nitrogen, respectively.

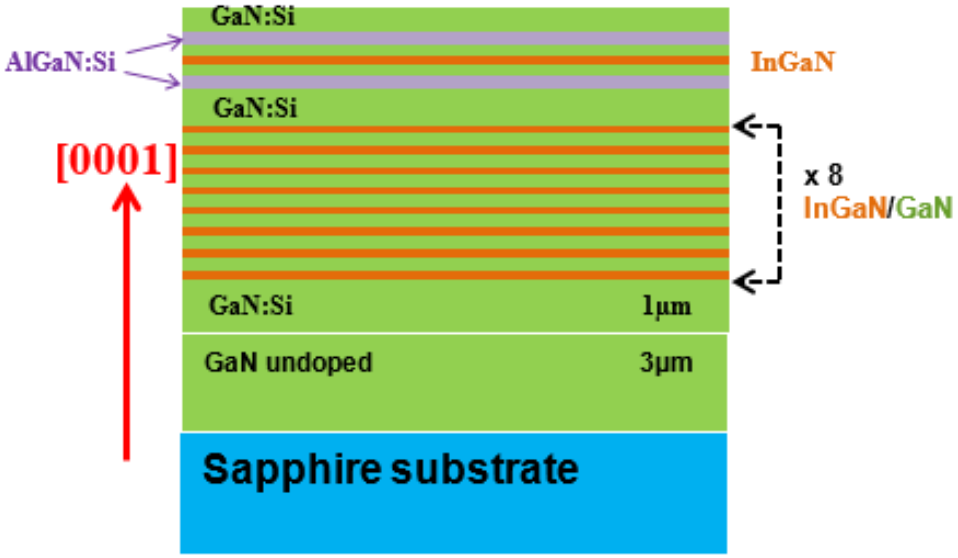

Figure 4.3: Sketch of the structures of the samples

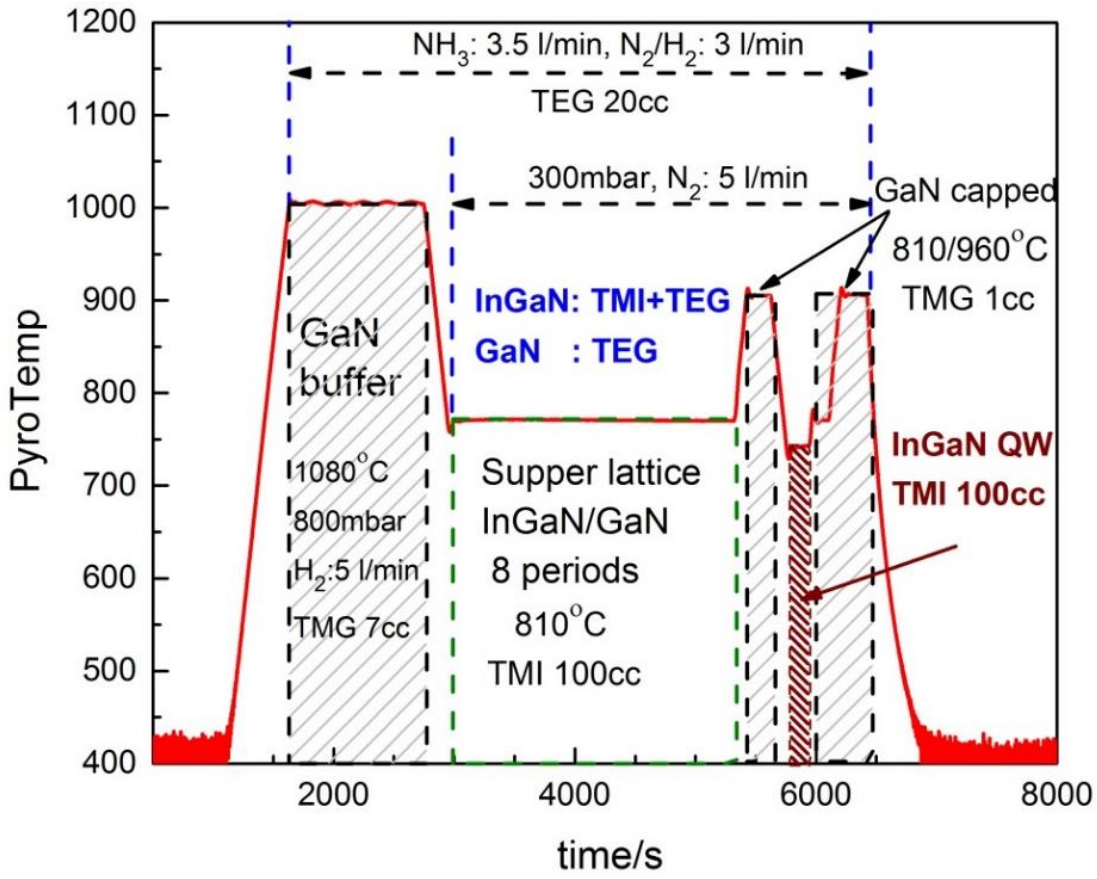

Figure 4.4: Evolution of growth temperature at each step of the growth process.

Figure 4.4 shows the evolution of the temperature and flux of the different chemical gases during the whole growth protocol. The growth rates can be measured in-situ using

laser reflectivity. The red-line in Fig. 4.4 shows the temperature at the surface of the samples measured by an infrared pyrometer. This temperature is lower than the set-up temperature measured by a thermocouple at the backside of the susceptor.

Starting from 3 µm-thick GaN-on-sapphire templates, we first grow a GaN buffer layer with a thickness of about 1 micrometer at 1080 °C. Then, a superlattice with 8-period of (In,Ga)N/GaN was grown at 830 °C with growth time of InGaN and GaN are 105 seconds and 160 seconds, respectively. The growth conditions of this superlattice are kept the same for all the samples. The superlattice is capped by a GaN layer grown at 960°C during 180 seconds. Then a single (In,Ga)N quantum well is grown. The (In,Ga)N growth temperature/time of are 780 °C/60 s for sample S_0, 750 °C/60 s for samples S_1 and S_3 and 750 °C/80 s for sample S_5.

As demonstrated in the previous chapter, using an AlGaN strain-compensating layer improves the crystallize quality. In this study, a 7.4 nm of $Al_{0.14}Ga_{0.86}N$ strain-compensating layer is inserted between (In,Ga)N QW and GaN barrier layers in the sample S_3, the yellow-emitting one. Finally, the InGaN layer capped by GaN following a two-step process: the first step by increasing the growth temperature from growth temperature of quantum well up to 830 °C for 160 seconds and the second step by increasing the growth temperature from 830 °C up to 960 °C then keeping it constant for 206 seconds. It is well known that the growth of InGaN alloy layers requires a lower temperature than the growth of GaN, which is itself grown under optimal conditions at lower temperatures than AlGaN alloys. Then, the lower temperature growth process of GaN layer minimizes indium desorption during the growth of GaN layer at 960 °C. All these details are of paramount importance to optimize the performances of the samples.

The structural parameters of the different samples (see Table IV.1) are extracted from separate calibration samples grown with similar growth conditions. The In composition and InGaN quantum well thicknesses are 0.15, 0.2, 0.2, 0.2 and 2.8, 3, 3, and 4 nm for samples S_0, S_1, S_3, and S_5, respectively. In sample S_3, 7.4 nm of an $Al_{0.14}Ga_{0.86}N$ strain-compensating layer is inserted on top of the InGaN layers and beneath the GaN top barrier layers.

Note that the GaN buffer layer, the GaN capped layer, and the $Al_{0.14}Ga_{0.86}N$ layer of samples S_1 and S_3 are doped with Si at a level estimated in the 2-5 $x10^{18}$ cm^{-3} range.

Table IV.1: Growth conditions and characteristic parameters of the single quantum well samples.

Sample	Growth conditions of QW		x_{In}	L_{InGaN} (nm)	$Al_{0.14}Ga_{0.86}N$	Si-doping
	T_{growth} (˚C)	t_{growth} (s)				
S_0	780	60	0.15	2.8	no	no
S_1	750	60	0.2	3	no	yes
S_3	750	60	0.2	3	yes	yes
S_5	750	80	0.2	4	no	no

4.1.2. Photoluminescence measurement

To investigate the optical properties of all samples, temperature dependent photoluminescence (PL), time-resolved photoluminescence (TRPL) spectroscopy and photo-excitation power-dependence (PEPD) measurements are performed. A laser at a wavelength (WL) of 266 nm is used as the excitation source. The repetition rate of the laser and the laser power are changed to adapt to each kind of measurement.

Temperature dependent PL measurement is carried out for all samples in a temperature range from 8 K to 300 K. In this kind of measurement, the laser repetition rate is selected at 80 MHz and the laser power is kept the same when changing temperature. The signal from the samples is detected by an Andor Newton spectrometer.

For the TRPL measurement, the samples are cooled down to 8 K in a closed cycle He cryostat. The pulse repetition rate of the laser (inverse of pulse width) is chosen at 80 or 8 kHz. The samples are excited under an extremely low excitation condition by a laser power density of 0.4 W/cm^2. The light emission of the samples is recorded by a 500IS Hamamatsu spectrometer that is connected to a Hamamatsu-C10910 streak camera whose resolution is about 150 ps.

For the PEPD measurement, we decided to examine the optical properties of the samples at 8K. The repetition rate of the laser is selected at 80 MHz. This value is higher than the recombination rate of all our samples so the PEPD measurement can be considered as continuous wave (CW) photoluminescence (PL) spectroscopy measurement. The laser power density for this measurement is varied through 4 decades from 1 x 10^{-1} W/cm^2 to 4 x 10^3 W/cm^2. The emission signal from the samples was collected by using a back-illuminated CCD camera (Andor Newton 920).

4.2. Photoluminescence spectra

4.2.1. Photoluminescence characteristics of all samples at 8 K

Figure 4.5 shows the normalized PL spectra of the SQW samples recorded at 8K. The spectrum of the blue light-emitting sample clearly indicates the presence of phonon replicas separated each other by 92 meV. The increase of the indium content and/or the QW width induces a PL line broadenings. This broadening is dominantly due to the fluctuations of the indium composition in the (In,Ga)N layers (see Fig. 4.6) and to the interface roughness typical of indium-based nitride heterostructures.[27] Another reason for the PL broadening in the samples S_1-S_5 is the contribution of the phonon replicas. Their energies splitting is not individually resolved although they can be obtained after a banal line-shape fitting.

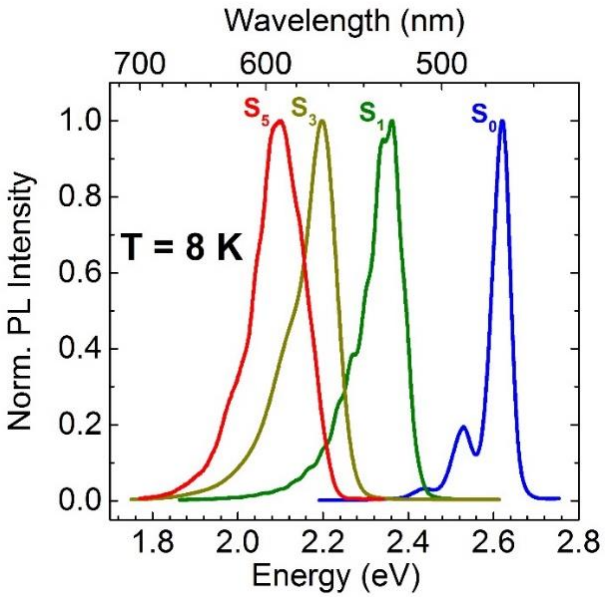

Figure 4.5. The photoluminescence spectra at 8K of all the samples.

Figure 4.6(a) shows the evolution of the bandgap of the $Ga_xIn_{1-x}N$ materials with alloy composition determined by using the equation:[28]

$$Eg(Ga_xIn_{1-x}N) = x\,Eg(GaN) + (1-x)\,Eg(InN) - b\,x\,(1-x) \qquad (4.1)$$

where the quantity b is a positive parameter and depends on the alloy composition, as we discussed earlier in Eq. (21) of the chapter II. The value of b is taken here near 2.8 eV. More details of this calculation are reported in Refs. 28,29.

Figure 4.6(b) shows that the maximum of the photoluminescence broadening due to the alloy disorder occurs for an In composition close to 0.2 corresponding to the range of In content in our samples (see Table IV.1). This indicates that the local alloy fluctuations

are large. Then, it should cause efficient carrier localization. Temperature dependent PL measurements are then performed to evaluate the carrier localization in our samples.

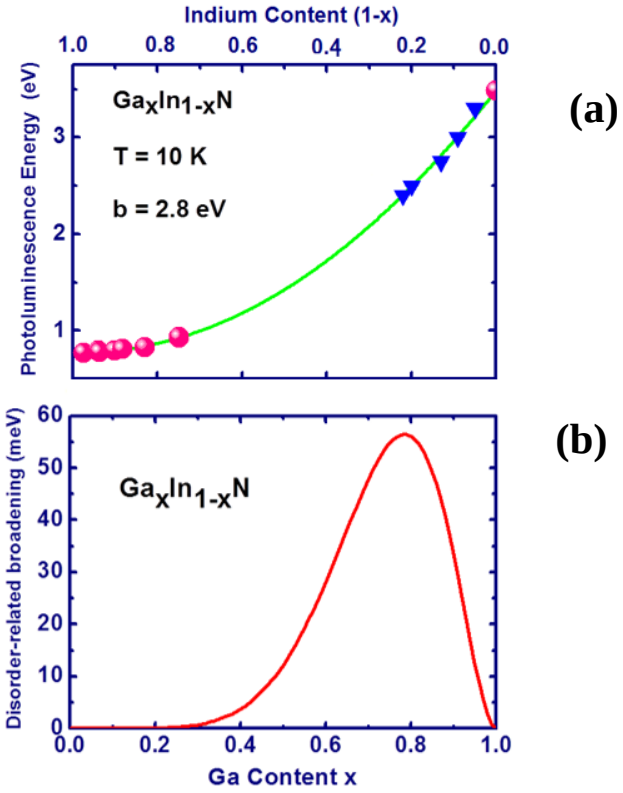

Figure 4.6. (a) Bandgap dependence of InGaN materials as a function of the alloy composition. (b) Photoluminescence broadening due to the chemical disorder in the InGaN alloys.[28,29]

4.2.2. Evolution of the photoluminescence energy versus temperature for the diagnosis of localization effects

Figure 4.7 shows the Arrhenius plot of all our single quantum well samples. We find similar behaviours to those observed for the MQW series: the integrated PL intensity decrease with the temperature is also caused by two kinds of thermal quenching characterized by activation energies E_a and E_b expressed as:

$$I_T = \frac{I_0}{1+A\exp\left(\frac{-E_a}{k_b T}\right)+B\exp\left(\frac{-E_b}{k_b T}\right)} \qquad (4.2)$$

where I_0 and I_T is the PL intensity at low temperature (8 K) and the PL intensity at a certain temperature T, coefficients A and B account for the strengths of the two thermal quenching mechanisms that correspond to the activation energies E_a and E_b and k_b is the Boltzmann constant.

The values of these quantities are summarized in Table IV.2 after a carefully fitting of the experimental data (Fig. 4.7) by Eq. (4.2).

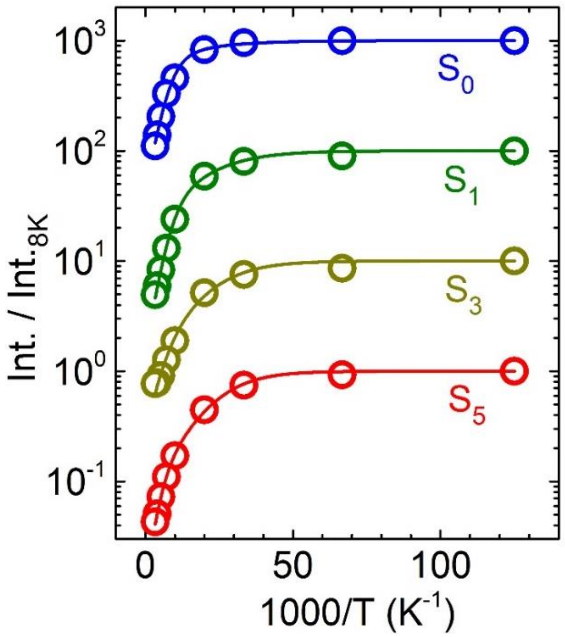

Figure 4.7. Arrhenius plots of integrated PL intensity of all samples as a function of the reciprocal temperature. The open circles represent for experimental data and the solid lines account for fitting lines.

Table IV.2. Coefficients A, B, activation temperatures T_a, T_b and activation energies E_a, E_b are assessed by applying the fitting due to Eq. (4.2).

Sample	A	E_a (meV)	B	E_b (meV)
S_0	8.3	9.5	15.3	39.5
S_1	5.5	8.6	20.8	35.5
S_3	2.9	7.3	17.9	32.0
S_5	0.6	6.0	6.9	29.5

Figure 4.8 shows that when increasing the temperature, the photoluminescence energy exhibits a red-shift. Then with a further increase of the temperature, the red-shift saturates up to a temperature $T_{localization}$ that corresponds to the localization energy $E_{Localization}$ of the electron-hole pairs:

$$E_{Localization} = k_b T_{localization} \quad (4.3)$$

where k_b is the Boltzmann constant

Finally, for temperatures above $T_{localization,}$ carriers have enough thermal energy to escape from deep localized-states of InGaN quantum well and migrate through the whole structures.[30] The peak energy slightly increases again before to reach the expected typical red-shift with increasing T in the high T range.[31] In our samples, in the 8K-300K range, it

never follows this expected general trend at high T, as an indication that localization is still efficient at room temperature. We find that samples which emit light at longer wavelength exhibit higher localization energies. We believed that this kind of localization relates to carrier localization induced by fluctuation of indium composition and fluctuation of QW width. Localization of carrier in the indium-rich regions is very efficient in our samples due to the average indium compositions ranging from 15 to 20 percent.

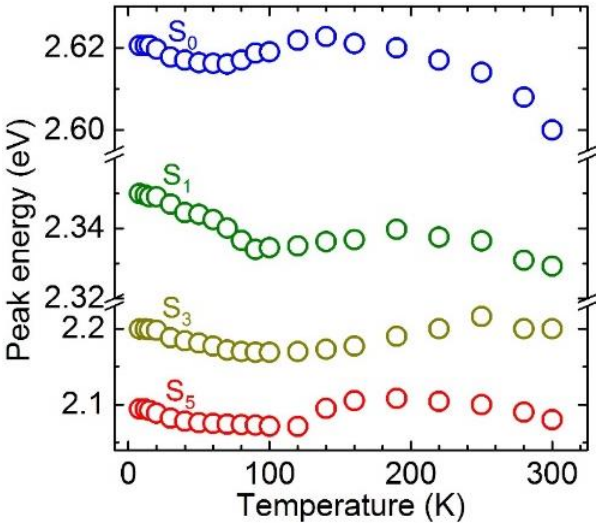

Figure 4.8. Evolution of peak energy of all samples with changing of temperature from 8 K to 300 K.

4.3. Evolution of IQE versus excitation power density

The evolution of the IQE versus excitation power density is examined by using the same method detailed in the chapter III. The value of the IQE at low excitation levels is determined first by using the TRPL, then the values of IQEs at different excitation power densities are extracted from the PEPD measurement.

4.3.1. The IQE at low excitation level

At low temperature and under low excitation conditions, the PL transients of all samples always exhibit a two-exponential decay kinetics, as plotted in Fig. 4.9. Applying the model of Iwata et al.,[32] the values of the IQEs are found and summarized in Table IV.3, for all samples. The IQE is the highest for the blue-light emitting sample (S_0) with a value of 73 percent. When increasing the emission wavelength to the green-red region, the IQEs decrease to 53-54 percent. Larger In composition and thicker QW layer with smaller overlapping wave functions of electron and hole lead to a lower IQE in samples S_1, S_3, and S_5.

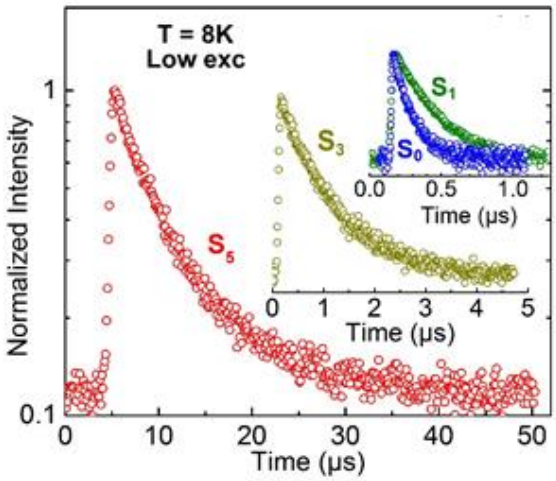

Figure 4.9. The 8 K transient photoluminescence spectra of all the samples determined by the time-resolved photoluminescence.

Table IV.3: Characteristic parameters of SQW samples

Sample	x_{In}	L_{InGaN} (nm)	$Al_{0.14}Ga_{0.86}N$	λ (nm)	$\tau_{rad} = \tau_{slow}$ (ns)	τ_{fast} (ns)	IQE (%)	P_T (Wcm^{-2})
S_0	0.15	2.8	no	475	45	17	73	40
S_1	0.20	3.0	no	525	210	84	54	15
S_3	0.20	3.0	yes	565	1371	510	54.6	1.5
S_5	0.20	4.0	no	595	8550	3045	53	0.25

4.3.2. IQE as a function of the excitation power density

These IQE values are obtained for a photo-excitation density of 0.4 W/cm^2 and we used them to normalize the IQEs as a function of the power excitation (PEPD measurements). Then the evolutions of IQE with excitation densities are obtained by a proportionality argument using as a multiplication factor, the ratio between the PL intensity and the pump power density.[26,33] By doing so, we find that at low excitation range, IQEs of the samples slightly increase with the increase of the pump power, as reported in Fig. 4.10. Then, the IQEs decrease for excitation densities beyond P_T, threshold value from which the evolution of the integrated PL intensity with excitation density changes its slope from linear to sub-linear (inset of the Fig. 4.10). The values of P_T decrease with the increase of the emission wavelength, similarly to we observed for the MQW structures.[33] This behaviour relates to the evolution of carrier densities in the active region with the increase of the excitation power density.

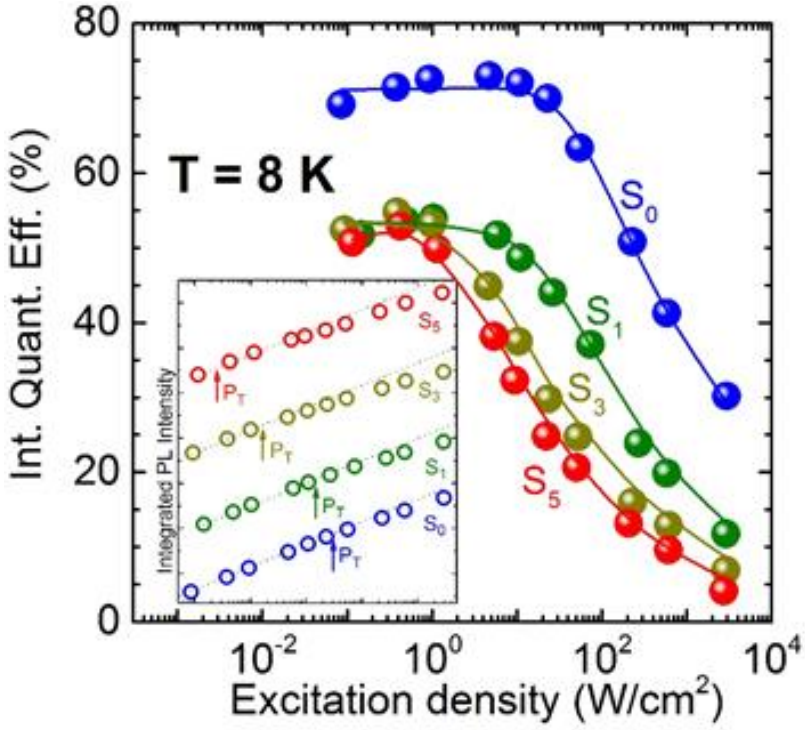

Figure 4.10. Evolution of the internal quantum efficiency as a function of the excitation power density for all samples. Inset shows the evolution of the integrated photoluminescence intensity versus photo-excitation pump power density.

We now calculate the carrier densities in our samples. They are excited by using a laser energy sitting at 4.66 eV (266 nm or 7.5 10^{-19} Joules). This excitation energy is above the values of the bandgaps of: the (In,Ga)N layers, the $Al_{0.14}Ga_{0.76}N$ ones, and the GaN layers as well. Under such excitation energy, photo-created carriers are generated in the whole samples. The absorption coefficient is chosen an average value of $\alpha_{@4.66\ eV}$ = 1.5 x 10^5 cm^{-1} slightly above the near band edge value of Fischer et. al[34] at 1.2 x 10^5 cm^{-1}, to account for the spectral dependence of the complex dielectric constants of the different materials.[35]

Almost all photons are absorbed in the GaN layers (thin GaN capped layer and thick GaN beneath layer), from which the photo-created electron and hole pairs diffuse towards the (In,Ga)N SQW layer. The diffusion length of carriers in InGaN-based heterostructures has been measured to sit in the range of around 0.1 µm to a few µm by Duboz et. al and Hafiz et. al.[36,37] Although this quantity can vary with crystalline quality of the samples, these values were obtained in conditions comparable to the conditions of our experiment and we conclude that almost all photo-created e-h pairs can diffuse towards the quantum well. Then, the carrier density *n* in the InGaN QW is given by:[33, 38]

$$n \approx \frac{P_{laser}\,(1-R)\;\alpha}{A_{spot}\;(h\upsilon)}\,IQE\;\tau_{rad}, \qquad (4.4)$$

where τ_{rad} is the standing time of the e-h in the active QW region that is listed in Table IV.3. At a given power excitation density, a longer decay time results in a higher carrier density in the active region. This triggers Auger recombination at lower value of the threshold P_T.

We emphasise the difficulty to obtain a real and exact determination of quantity of the carrier density as the absorption coefficients in the different layers vary with the values of the internal electric fields, but we are strongly confident in the pertinence of this average determination in terms of weighted thickness of the different layers. This approach is compatible with the previous reports of a carrier capture from barrier layer to the QW layer that increases with the increase of excitation density.[39-41] The assumption here is that the capture rate is constant through the whole range of excitation densities.

4.4. Simulation using the ABC model

The ABC model is supposed to work at low temperature (8 K) although values of its parameters are not easily scaled. Coefficient A accounts for Shockley-Read-Hall (SRH) non-radiative recombination process that is thermally activated.[42] Coefficient B represents the radiative recombination processes that varies like $T^{x/2}$ with temperature T, where x is the dimension of the space where the electron-hole pairs live: x = 3 for bulk, x = 2 for QW, x = 1 for quantum wires, and x = 0 for quantum dots or slightly 3D confined systems.[43] The evolution of the PL energy shown in Fig. 4.8 evidenced the localized behaviour of the e-h pairs. Therefore, B ***weakly*** varies with T in our samples. As B does not drastically vary with T, the variations of A with T are responsible of the collapse of the PL intensity from low temperature to ambient one, that we previously reported for such samples.[27] Coefficient C accounts for Auger non-radiative recombination process that is a complex function of the bandgap of the semiconductor and the lattice temperature.[44]

Barrier layers of some of our samples are doped with silicon. For this reason, a modified ABC model considering the barrier doping n_0 is used. In this model, the value IQE is given by equation:

$$IQE = \frac{Bn(n+n_0)}{\frac{2An(n+n_0)}{2n+n_0} + Bn(n+n_0) + Cn(n+n_0)^2}, \quad (4.5)$$

Then, to estimate the sensitivity to the change of IQE with the residual carrier density, the derivative of IQE with carrier density n is considered. It can be expressed by equation:

$$\dot{y} = I\dot{Q}E = \frac{4AB - BC(2n+n_0)^2}{[2A + B(2n+n_0) + C(n+n_0)(2n+n_0)]^2} \quad (4.6)$$

The derivative $I\dot{Q}E$ passes by zero at $\tilde{n} = (\sqrt{A/C} - n_0/2)$.

Then, maximum value of IQE is:

$$IQE_{MAX} = \frac{1}{1+\frac{2\sqrt{AC}}{B}+\frac{C\,n_0}{2B}} \quad (4.7)$$

The calculation above indicates that the onset of the efficiency droop (at $\tilde{n} = \sqrt{A/C} - n_0/2$) is independent of the radiative recombination processes. It only depends on non-radiative recombination channels: SRH process (A), Auger process (C) and residual doping n_0. Equation (4.7) shows that at constant values of A, B, and C, the IQE_{MAX} gets a smaller value at higher value of the residual doping n_0. We note that the value of n_0 is estimated in the 2-5 $x10^{18}$ cm^{-3} range for all the samples. This indicates that the (Al)GaN layers grown at low temperature (even without Si doping) are highly non-intentionally n-type doped. We shall see that the large value of n_0 is impacting the shape of the function IQE(n) which will be rather flat in the $n < n_0$ range.

In this simulation, we include the screening of the internal electric field that is to say the decrease of the decay time with the increase of excitation power.[45, 46] The effect of phase-space filling is also considered. It leads to a reduction of the radiative recombination coefficient B that we express according to Hader et. al:[47]

$$B(n) = \frac{B_0}{1+(\frac{n+n_0}{n_{psf}})^{\gamma}} \quad (4.8)$$

where B_0 is value of coefficient B at low excitation density, n_{psf} = 2 x 10^{19} cm^{-3} is the carrier density for the onset of phase-space filling effect, γ = 0.82 is a dimensionless exponential.[48]

At high excitation range, the Auger recombination term can become sub-cubic with an evolution of coefficient C similar to that of coefficient B[47,49,50] thanks to a power-law relation of C and B.[51] Therefore, we assume here that the coefficient C has evolution with the carrier density by

$$C(n) = \frac{C_0}{1+(\frac{n+n_0}{n_{psf}})^{\gamma}} \quad (4.9)$$

Then we obtain very good fitting curves with the experimental data. These fittings are plotted as solid lines in Fig. 4.10.

4.5. Discussion

4.5.1. Recombination processes at low temperature

Figure 4.11(a) shows the evolution of the different recombination rates versus power excitation density in the case of sample S_3. At low excitation density, the radiative recombination rate is the largest and both non-radiative recombination rates are equivalent. It gives a slight increase of the IQE. Then, when the non-radiative Auger recombination rate strongly increases and becomes the dominating recombination channel; and the radiative recombination rate is reduced by the phase-space filling effect, the IQE strongly decrease. At these excitation conditions, the variation of the IQE with the photo-excitation density is ruled by a universal power law independent of the design: $IQE = IQE_{MAX} - a\ log_{10}P$ with *a is approximate 1/3*. This behavior is also observed in the MQW structures (samples M_1, M_3, and M_5) with light emission in the same ranges as in this study, see Fig. 4.11(b).

The photo-generated carrier densities are proportional to the standing time of carriers in the quantum wells (Eq. (4.4)). Therefore, at a given photo excitation density, a long decay time leads to a higher carrier density than a short one would give. This enhances carrier-carrier repulsions and promotes Auger recombination. The variation of the radiative decay time with P_T (Fig. 4.11(c)) shows an average slope identical for both SQW and MQW samples. It indicates that long decay times, strongly impact the value of the pump density at which occurs the onset of Auger recombination. Therefore, a strong QCSE induces a reduction of the IQE at a smaller value of threshold P_T of excitation density than moderate or even weak QCSE. In addition, fluctuations of indium content and fluctuations of QW thickness both favour carrier localization to energy minima. They induce local accumulations of electric charges in specific regions. A large value of the localization energy ($E_{localization}$) corresponds to local and dense accumulations of carriers. This favours carrier-carrier repulsion, triggers the Auger recombination, hence resulting in the reduction of IQE and in the reduction of the value of P_T, as reported in Fig. 4.11(c).

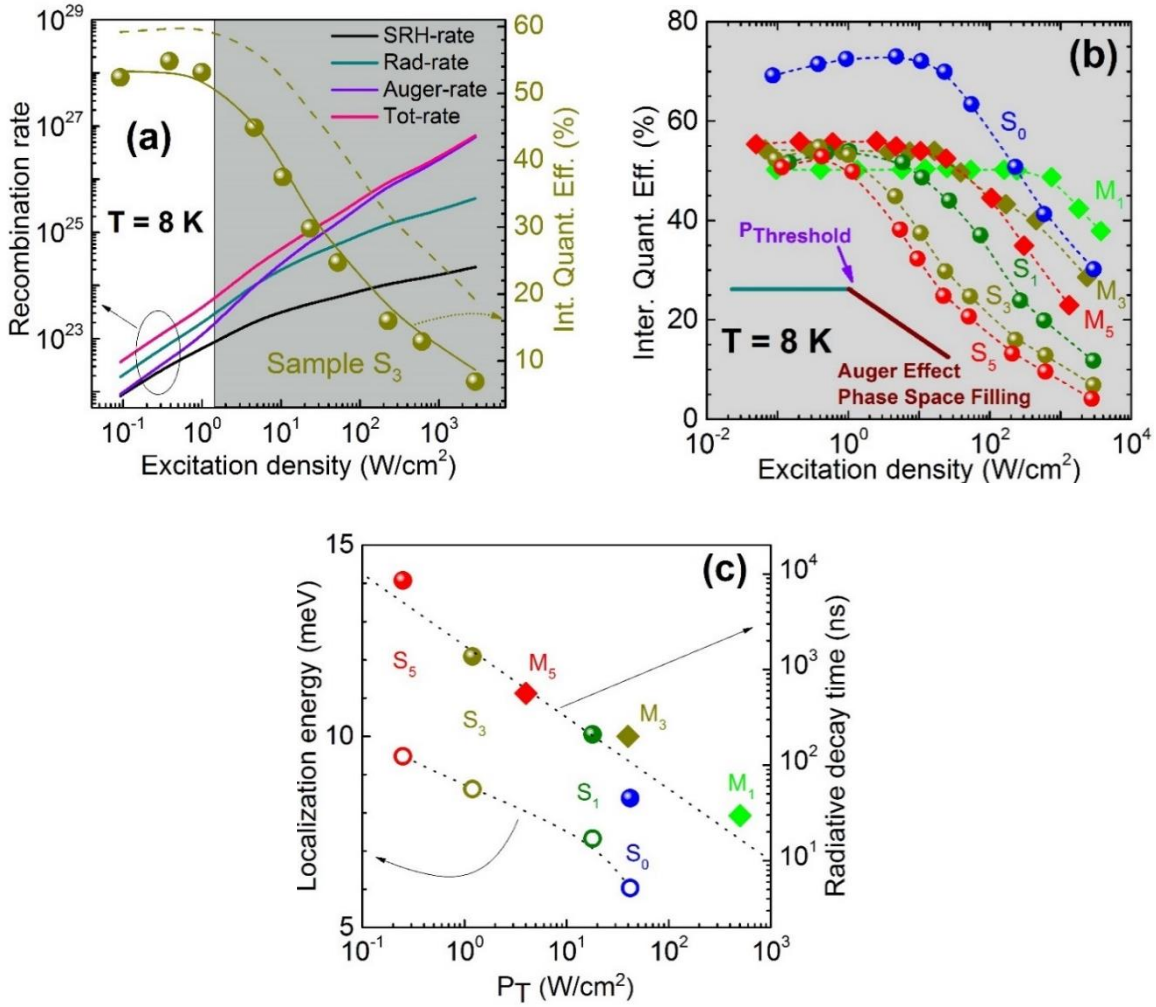

Figure 4.11. (a) **Left-hand axis:** Evolutions of different recombination rates of sample S_3 with photo-created carrier density; black lines, dark cyan lines, violet lines, and pink lines represent for the Shockley-Read-Hall, radiative, Auger, and the total recombination rates, respectively. Solid dark yellow and dashed dark yellow lines are the fitting curves with and without consideration for the phase-space filling effect, respectively.
Right-hand axis: Evolution of internal quantum efficiency of yellow-light emitting sample (S_3)

Figure 4.11. (b) Comparison of internal quantum efficiency of single quantum wells structures (this study) with the internal quantum efficiency of multiple quantum wells structures that emit in the similar light emission range.[33]

Figure 4.11. (c) **Left-hand axis:** Plots of localization energy (circles) **Right-hand axis:** radiative decay time as functions of P_T the threshold of excitation power density.
In both figures (b) and (c) data for SQW are plotted using spheres while solid diamonds represent data for MQW[33]. The dotted lines are guides for the eye.

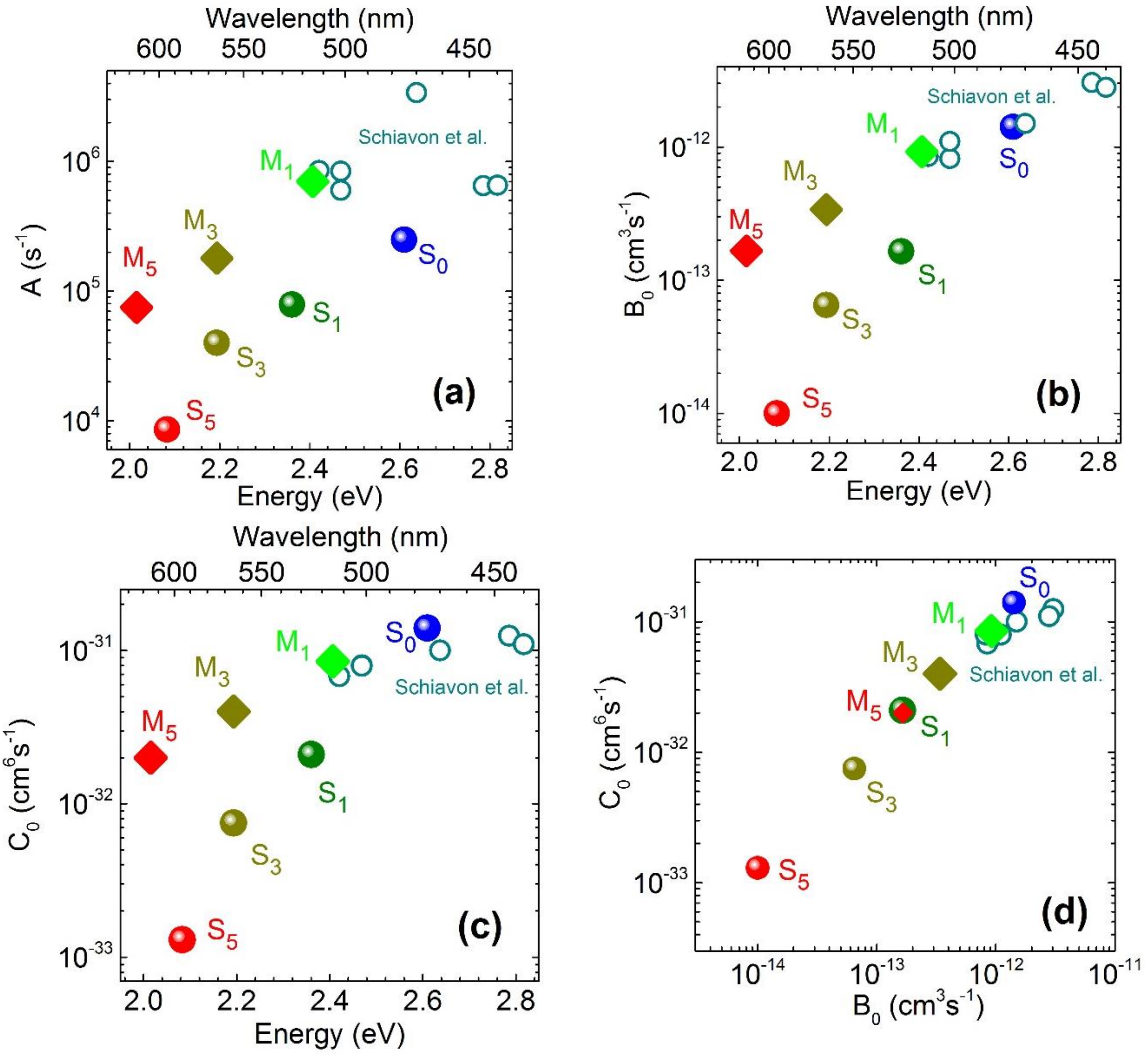

Figure 4.12. (a)-(c) Plot of coefficients A, B_0, C_0 as functions of the emission energy of our single quantum wells samples with the data from literature.[10,33] (d) Relation of the coefficient C_0 with the coefficient B_0.

Figures 4.12 (a)-(c) show that the coefficients A, B_0, and C_0 decrease with the decrease of emission energy for our SQWs and MQWs samples. In our SQW samples, the lower emission energy (longer emission wavelength) samples have higher localization energy. This enhances carrier localization at the in-rich region and prevents carrier migrates toward the non-radiative recombination centers. Therefore, it gives a reduction of coefficient A with decreasing emission energy.

The longer decay times in the lower emission energy samples show that combination of increasing indium content, adding an (Al,Ga)N layer, and increasing QW width increases impact of the QCSE. Then, they produce a reduction of the overlap of the electron and holes wave function that leads to a dramatic reduction of the values of coefficient B_0 for these

samples. Coefficient C_0 of the Auger recombination are related to the radiative recombination coefficient by a relationship $(B_0)^{3/2}$, as shown in Fig. 4.12(d).[51] Then, the decreasing of B_0 leads to the decreasing of C_0.

4.5.2. Dependence of A, B, and C coefficients with temperature

To go further, we examine the temperature dependence of the different recombination coefficients A, B, and C, at low excitation density conditions P = 0.4 Wcm^{-2}. The radiative recombination strongly depends on the QCSE as evidenced by the measurements of radiative decay times that vary from a sample to another one. As shown earlier, localization processes are effective in our samples and temperature weakly impacts the radiative decay times although it enhances the proportion of the fast decay component in the PL transients. Therefore, we assume here that the coefficient B of the radiative recombination keeps a constant value in the whole temperature range.

Several scattering mechanisms and their respective changes with temperature are altogether expressed through the value of the Auger recombination coefficient C.[44,50,52,53] Disentangling requires advanced theoretical calculations that are out of the scope of our experimental work.

To determine the increase of coefficient C with the temperature, we decided to apply a thermal enhancement of the Auger coefficient that was developed by Nirschl et al.[54] and by Galler et al.[22] The evolution of the coefficient C as function of the temperature following such an approach is reported at the top of Fig. 4.13(a). Our slopes depend on the low temperature values of C and are for that reason found slightly smaller than the experimental result reported for blue InGaN single QW by Galler et al.[22] with temperature ranging from 25 K to 100 K. We emphasize the fact that the coefficient C increases with a similar slope than the one found by Kioupakis et al.[55] for InGaN emitting at 590 nm and in agreement with the trend reported by Bertazzi et al.[52] According to theorists, increasing the temperature enhances the phonon density and the interactions of the carriers with phonons. The increase of the values of coefficient C with changing temperature reveal indirect Auger recombinations.[53,55]

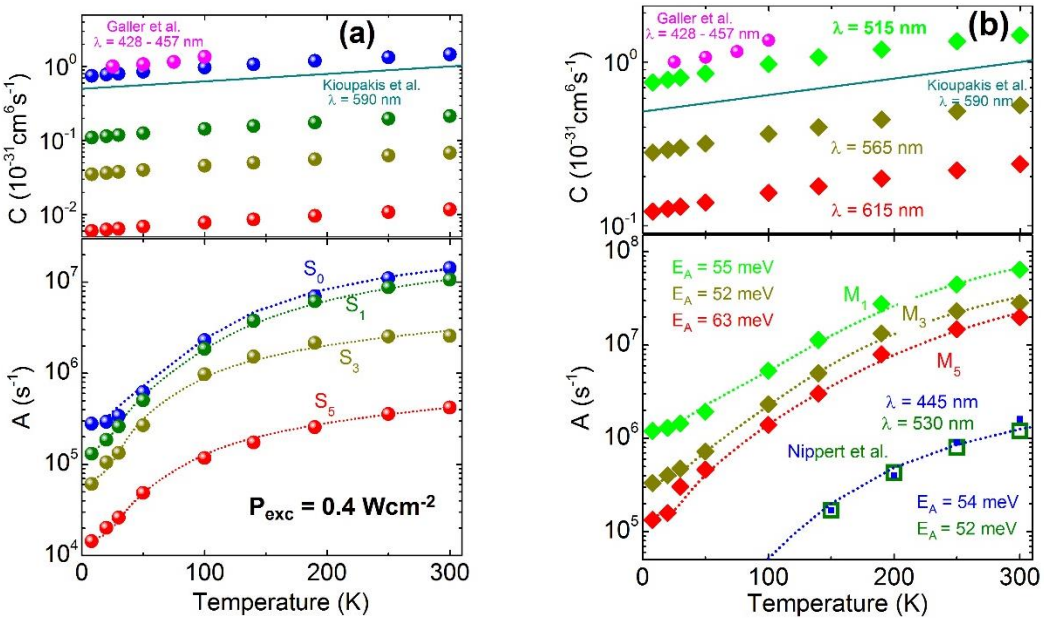

Figure 4.13(a) **Top:** Evolution of coefficients C of all single quantum well samples as functions of temperature; **Bottom:** Evolution of coefficients A of all single quantum well as functions of temperature.

Figure 4.13(b) **Top:** Evolution of coefficients C of all multiple quantum well samples as functions of temperature; **Bottom:** Evolution of coefficients A of all multiple quantum well samples as functions of temperature; green open squares and blue squares are the data published by Nippert et al.[42]

In both figures, short dotted lines are theoretical curves of 2 activation energies; pink spheres show literature data of Galler et al.[22]; dark cyan line is the data published by Kioupakis et al.[55]

Knowing the values of B and C, we can then get the values of the coefficient A from Eq. (4.5) as reported in the bottom of Fig. 4.13(a). We find that the variation of coefficient A with temperature follows a model of two activation energies E_{a1} and E_{a2}, that can be written as:[42,54]

$$A = A_0 + A_{01} exp\left(\frac{-E_{a1}}{k_B T}\right) + A_{02} exp\left(\frac{-E_{a2}}{k_B T}\right), \qquad (4.10)$$

A_0 is an offset value that is in turn very close to the 8K value of A obtained using the ABC model. The values of these activation energies E_{a1} and E_{a2} are determined from the Arrhenius plot of integrated PL intensities as functions of the temperature T. The good agreement between the theoretical curves and the values extracted from the experimental data in the bottom of Fig. 4.13(a) is an evidence of the strong increase of A with T, mainly in correlation with thermally activated processes. The values of the smaller activation energies E_{a1} are close to the values of the localization energy $E_{Localization}$ that were earlier determined by the temperature dependent measurement of the PL energy, see Fig. 4.11(c). These energies relate to the delocalization of carriers weakly localized prior to their non-

radiative recombination.[56,57] The low values of these localization energies are indicative of a good quality of the InGaN layers in our samples. The values of the second set of activation energies E_{a2} are 29.5 mev, 32 meV, 35.5 meV and 39.5 meV. They are attributed to the direct diffusion of carriers from more strongly localized regions towards the nonradiative recombination centers.[58] This second de-trapping process is the dominating channel, that contributes to A in the higher temperature range near 90 K and 120 K for the blue light emitting and green light emitting samples respectively. Regarding yellow and red-light emitters this occurs in a range of temperatures beyond 400 K. This switching is coherent with the energy versus T dependence of the PL energy peak and we believe that this is linked to the relative contributions of both processes and that it is on the one hand linked to the morphology of InGaN at the nanoscale and on another hand correlated to the efficient localization to interfaces roughness. To go further we have re-handled our results on multiple quantum wells.

The evolution of parameter C with T is similar for MQWs and SQWs as reported at the top in Fig. 4.13(b). This is fully different concerning A as indicated at the bottom of Fig. 4.13(b): though there still exist a contribution ruled by a low-value activation energy (in the 9-11-12 meV like for SQWs), the values of the second activation energies of the **strongly dominating process** are from green to red 55 meV, 52 meV and 63 meV, respectively. These values are compared with the values reported by Nippert et al..[42] We believe that vertical fluctuations of well-widths at the scale of the whole MQW stackings lead to broader distributions of interfacial roughness than in case of SQWs, which we believe are the *bonafide* reasons for increasing the value of this second activation energy. On the contrary, as the morphology of the InGaN alloy is almost the same at the nanoscale in both series of samples, the low-value activation energies are similar.

4.6. Conclusions

In InGaN-based heterostructures grown along the polar direction, the QCSE increases the photoluminescence decay time and favours the accumulation of charge carriers at heterointerfaces (electrons at one side of the QW, holes at the opposite one). In addition to the blocking of the carriers to hetero-interfaces by the on-axis electric-field, any increase of the indium composition will favour three-dimension localization of the carriers in quantum well regions for which the indium content is higher than the average value. The increase of carrier density by combined influences of QCSE and carrier localization lowers

the value of the threshold photoexcitation density P_T beyond which the Auger processes become the dominant recombination channel. We have demonstrated how the combined influences of the sample design, decay times, and localization efficiency trigger the onset of phase-space filling effects. These effects reduce the radiative recombination coefficient B at high excitation region and it also favors the onset of Auger effect (it reduces the value of the threshold excitation density P_T). The Auger effect is demonstrated to be the main reason of reduction of the IQE at high excitation conditions. In such regime, the variation of the IQE with photo-excitation density is ruled by a universal power law independent of the design: $IQE = IQE_{MAX} - a\ log_{10}P$ with a is approximate 1/3.

In conclusion, we find that the QCSE, the spatial localizations of carriers, and interaction of the carriers with the phonon field are measured to be the mechanisms that establish the AE and its dependence with the temperature. Shockley-Read Hall non-radiative recombination is calibrated too as well as their dependence with T. At low temperature, both QCSE and carrier localization to either indium-rich or well regions thicker than the average value contribute in concert to trigger electron-electron repulsions and therefore the onset of Auger effect. Under high photo injection densities, the influence of phase space filling effect leads to a detrimental reduction of radiative recombination rate which favours AE and SRH non-radiative recombination process with respect to the radiative one. This produces a dramatic collapse of the IQE. Increasing the temperature enhances the phonon density and the increase of the value of coefficient C with changing temperature reveals indirect Auger recombination that is to say interactions of the carriers with, according to theorists, other phonons than the longitudinal optical (LO) one. The large range of emission wavelength investigated as well as the different designs of the samples studied here also offer a global overview of the mechanisms that rule SRH non-radiative recombination. The temperature dependence of SRH is ruled by two de-trapping mechanisms of the carriers followed by their re-trapping to non-radiative recombination centres. The first mechanism is a de-trapping of the carriers from local fluctuations of composition. This mechanism is ruled by activation energies sitting in the in the 7-12 meV range for both single QW and multiple QW designs. The second mechanism is ruled by activation energies of about 30 meV for single quantum wells and twice this value for multiple quantum wells. Fluctuations of well-widths which are broader distributed around the average values for multiple quantum wells than for single quantum wells rule this second contribution to SRH.

References

1. T. Takeuchi, S. Sota, M. Katsuragawa, M. Komori, H. Takeuchi, H Amano and I. Akasaki, Jpn. J. Appl. Phys. **36**, L382 (1997)
2. F. Bernardini, V. Fiorentini, and D. Vanderbilt, Phys. Rev. B **63**, 193201 (2001)
3. M. Deppner, F. R¨omer, and B. Witzigmann, Proc. of SPIE **8619**, 86191J (2013)
4. E. Kioupakis, Q. Yan, and C. G. Van de Walle, Appl. Phys. Lett. **101**, 231107 (2012)
5. A. David, and M. J. Grundmann, Appl. Phys. Lett. **97**, 033501 (2010)
6. R. Vaxenburg, E. Lifshitz, and Al. L. Efros, Appl. Phys. Lett. **102**, 031120 (2013)
7. R. Nakamura, and M. R. Krames, Proc. of the IEEE **101**, 2211 (2013)
8. M. R. Krames, O. B. Shchekin, R. Mueller-Mach, G. O. Mueller, L. Zhou, G. Harbers, and M. George Craford, J. Disp. Technol. **3**, 160 (2007)
9. M. A. der Maur, W. Rodrigues, A. di Carlo, A. Pecchia, and G. Penazzi, Phys. Rev. Lett. **116**, 027401 (2015)
10. D. Schiavon, M. Binder, M. Peter, B. Galler, P. Drechsel, and F. Scholz, Phys. Stat. Sol. B **250**, 283 (2013)
11. Y.-S. Yoo, J.-H. Na, S. J. Son, and Y.-H. Cho, Sci Rep **6**, 34586 (2016)
12. H. Jeong, H. J. Jeong, H. M. Oh, C.-H. Hong, E.-K. Suh, G. Lerondel and M. S. Jeong, Sci Rep **5**, 9373 (2015)
13. D. Watson-Parris, M. J. Godfrey, P. Dawson, R. A. Oliver, M. J. Galtrey, M. J. Kappers, and C. J. Humphreys, Phys. Rev. B **83**, 115321 (2011)
14. J. H. Na, R.A. Taylor, Kwan H. Lee, T. Wang, A. Tahraoui, P. Parbrook, A. Mark Fox, Sam N. Yi, Young S. Park, Jae W. Choi, and Jung S. Lee, Appl. Phys. Lett. **89**, 253120 (2006)
15. Z. Li, J. Kang, B. W. Wang, H. Li, Y. H. Weng, Y.-C. Lee, Z. Liu, X. Yi, Z. C. Feng, and G. Wang, J. Appl. Phys. **115**, 083112 (2014)
16. C.-K. Wu, C.-K. Li, and Y.R. Wu, J. Comput. Electron **14**, 416 (2015)
17. Y. C. Shen, G. O. Mueller, S. Watanabe, N. F. Gardner, A. Munkholm, and M. R. Krames, Appl. Phys. Lett. **91**, 141101 (2007)
18. G. Verzellesi, D. Saguatti, M. Meneghini, F. Bertazzi, M. Goano, G. Meneghesso, and E. Zanoni, J. Appl. Phys. **114**, 071101 (2013)
19. U. Ozgur, H. Liu, X. Li, X. Ni, and H. Morkoc, Proc. of the IEEE **98**, 1180 (2010)

20. J. Iveland, L. Martinelli, J. Peretti, J. S. Speck, and C. Weisbuch, Phys. Rev. Lett. **110**, 177406 (2013)
21. D. A. Zakheim, A. S. Pavluchenko, D. A. Bauman, K. A. Bulashevich, O. V. Khokhlev, and S. Yu. Karpov, Phys. Status Solidi A **209**, 456 (2012)
22. B. Galler, P. Drechsel, R. Monnard, P. Rode, P. Stauss, S. Froehlich, W. Bergbauer, M. Binder, M. Sabathil, B. Hahn, and J. Wagner, Appl. Phys. Lett. **101**, 131111 (2012)
23. M. J. Davies, P. Dawson, S. Hammersley, T. Zhu, M. J. Kappers, C. J. Humphreys, and R. A. Oliver, Appl. Phys. Lett. **108**, 252101 (2016)
24. T. H. Ngo, B. Gil, P. Valvin, B. Damilano, K. Lekhal, and P. De Mierry, Appl. Phys. Lett. **107**, 122103 (2015)
25. K. Lekhal, B. Damilano, H. T. Ngo, D. Rosales, P. De Mierry, S. Hussain, P. Vennéguès, and B. Gil, Appl. Phys. Lett. **106**, 142101 (2015)
26. T. H. Ngo, B. Gil, P. Valvin, B. Damilano, K. Lekhal, and P. de Mierry, Jpn. J. Appl. Phys. **55**, 05FG10, (2016)
27. F. C-P. Massabuau, P. Chen, M. K. Horton, S. L. Rhode, C. X. Ren, T. J. O'Hanlon, A. Kovács, M. J. Kappers, C. J. Humphreys, R. E. Dunin-Borkowski, and R. A. Oliver, J. Appl. Phys. **121**, 013104 (2017)
28. B. Damilano and B. Gil, J. Phys. D: Appl. Phys. **48**, 403001 (2015)
29. M. Moret, B. Gil, S. Ruffenach, O. Briot, C. Giesen, M. Heuken, S. Rushworth, T. Leese, and M. Succi, J. Cryst. Growth **311**, 2795 (2009)
30. J. Abell, and T. D. Moustakas, Appl. Phys. Lett. **92**, 091901 (2008)
31. P. Dawson, S. Schulz, R. A. Oliver, M. J. Kappers, and C. J. Humphreys, J. Appl. Phys. **119**, 181505 (2016)
32. Y. Iwata, R. G. Banal, S. Ichikawa, M. Funato, and Y. Kawakami, J. Appl. Phys. **117**, 075701 (2015)
33. T. H. Ngo, B. Gil, B. Damilano, K. Lekhal, and P. de Mierry, Superlattices Microstruct. **103**, 245 (2017)
34. A. J. Fischer, W. Shan, J. J. Song, Y. C. Chang, R. Horning, and B. Goldenberg, Appl. Phys. Lett. **71**, 1981 (1997)
35. A. W. R. L. Lambrecht, B. Segall, J. Rife, W. R. Hunter, and D. K. Wickenden, Phys. Rev. B **51**, 13516 (1995)
36. J. Y. Duboz, F. Binet, D. Dolfi, N. Laurent, F. Scholz, J. Off, A. Sohmer, O. Briotc, B. Gil, Mater. Sci. Eng. B **50,** 289 (1997)

37. S. Hafiz, F. Zhang, M. Monavarian, V. Avrutin, H. Morkoc¸, U. Ozgur, S. Metzner, F. Bertram, J. Christen, and B. Gil, J. Appl. Phys. **117**, 013106 (2015)
38. Y. Kawakami, A. Kaneta, A. Hashiya, and M. Funato, Phys. Rev. Appl. **6**, 044018 (2016)
39. W. H. Fan, S. M. Olaizola, T. Wang, P. J. Parbrook, J.-P. R. Wells, D. J. Mowbray, M. S. Skolnick, and A. M. Fox, Phys. Stat. Sol. (b) **240**, 364 (2003)
40. W. H. Fan, S. M. Olaizola, J.-P. R. Wells, A. M. Fox, T. Wang, P. J. Parbrook, D. J. Mowbray, and M. S. Skolnick, Appl. Phys. Lett. **84**, 3052 (2004)
41. J. Wang, K. W. Kim, and M. A. Littlejohn, App. Phys. Lett. **71**, 820 (1997)
42. F. Nippert, S. Y. Karpov, G. Callsen, B. Galler, T. Kure, C. Nenstiel, M. R. Wagner, M. Straßburg, H.-J. Lugauer, and A. Hoffmann, Appl. Phys. Lett. **109**, 161103 (2016)
43. D. Rosales, T. Bretagnon, B. Gil, A. Kahouli, J. Brault, B. Damilano, J. Massies, M. V. Durnev, and A. V. Kavokin, Phys. Rev. B **88**, 125437 (2013)
44. Sheng S. Li, *Semiconductor Physical Electronics*, 2nd ed, Springer: New York, 2006, p144
45. A. David, and M. J. Grundmann, App. Phys. Lett. **96**, 103504 (2016)
46. E. Sari, S. Nizamoglu, I.-H. Lee, J.-H. Baek, and H. V. Demir, App. Phys. Lett. **94**, 211107 (2009)
47. J. Hader, J V. Moloney, and S W. Koch, Appl. Phys. Lett. **87,** 201112 (2005)
48. E. Kioupakis, Q. Yan, D. Steiauf, and C. G Van de Walle, New J. Phys. **15**, 125006 (2013)
49. A. David, and M. J. Grundmann, App. Phys. Lett. **96**, 103504 (2010)
50. W. Guo, M. Zhang, P. Bhattacharya, and J. Heo, Nano Lett. **11**, 1434 (2011)
51. C. Weisbuch, M. Piccardo, L. Martinelli, J. Iveland, J. Peretti, and J. S. Speck, Phys. Status Solidi A **212**, 899-913 (2015)
52. F. Bertazzi, M. Goano, and E. Bellotti, Appl. Phys. Lett. **101**, 011111 (2012)
53. E. Kioupakis, D. Steiauf, P. Rinke, K. T. Delaney, and Chris G. Van de Walle, Phys. Rev. B **92**, 035207 (2015)
54. A. Nirschl, A. Gomez-Iglesias, M. Sabathil, G. Hartung, J. Off, and D. Bougeard, Phys. Status Solidi A **211**, 2509 (2014)
55. E. Kioupakis, P. Rinke, K. T. Delaney, and C. G. Van de Walle, Appl. Phys. Lett. **98**, 161107 (2011)
56. H. P. D. Schenk, M. Leroux, and P. de Mierry, J. Appl. Phys. **88**, 1525 (2000)

57. Y. -H. Cho, G. H. Gainer, A. J. Fischer, J. J. Song, S. Keller, U. K. Mishra, and S. P. DenBaars, Appl. Phys. Lett. **73**, 1370 (1998)
58. J. Abell, and T. D. Moustakas, Appl. Phys. Lett. **92**, 091901 (2008)

CHAPTER V

INTERNAL QUANTUM EFFICIENCY OF InGaN/(In)GaN MULTIPLE QUANTUM WELLS GROWN ON THE (11-22) SEMI-POLAR PLANE

In the previous chapters, the investigation of polar oriented samples emitting in a large range of the visible light from blue to the red-light reveals that the combination of the QCSE and of the spatial carrier localization is the main mechanism for activating non-radiative Auger recombination. This caused a reduction of the efficiency under high excitation conditions. In our opinion, the impact of the QCSE plays a more important role on the reduction of the IQE at high excitation level than the localization effect does. In long-wavelength light emitters, the impact of QCSE is high due to width of the QW or the high In composition. Therefore, to grow an efficient long wavelength emission, it requires to reduce, the carrier accumulation caused by the QCSE at the interfaces of the InGaN QW.

Very recently, some experimental study and theoretical calculations[1-4] demonstrated that using the semi-polar oriented InGaN QW increases the threshold for the onset of reduction of the IQE. In 2009, our co-worker, Philippe De Mierry showed that orange-red light emission can be obtained from InGaN layers on semi-polar (11-22) GaN templates grown on m-plane sapphire. He was able to demonstrate a red-light emission (628 nm) from a LED semi-polar-oriented, with an output power of 4.5 µW at an injection current of 20 mA. He used a 4 periods InGaN/GaN MQW[5]. These reasons lead us to extend our study by using semi-polar InGaN/(In)GaN structures operating from the blue to the red-light.

One challenge for growing an efficient semi-polar InGaN/GaN light emitter is linked to the limited crystalline quality of the GaN buffer layer. The growth semi-polar (11-22) GaN on r-plane patterned sapphire substrate is one solution to improve the quality of this structure.[6,7] In addition, using strain relaxed (11-22) InGaN underlying buffer layer was demonstrated as being a suitable candidate for growing long wavelength devices.[8,9] Therefore, to get efficient red-light emission, we decided to grow [11-22] semi-polar $In_xGa_{1-x}N/In_yGa_{1-y}N$ multiple quantum wells on relaxed $In_yGa_{1-y}N$ layers that are grown on GaN on r-plane patterned sapphire substrate.

5.1. Experimental procedure

5.1.1. Sample structures

Two InGaN/(In)GaN multiple quantum well (MQW) samples are grown in a home-made MOCVD vertical reactor using NH_3, TEG and TMI as the precursor sources of N, Ga, and In. Starting from a high quality GaN template on r-plane patterned sapphire substrate[7] a 0.5 µm-thick GaN layer is grown at 1000 °C. For the sample SP1, a 5 periods InGaN/GaN MQW is grown. For the sample SP_2, a 90 nm-thick InGaN layer is grown at 800 °C followed by 5-periods of an InGaN/(In)GaN quantum well. Growth conditions of the QWs region are kept the same for the two samples with growth temperature, T_g, and growth time, t_g, that are (T_g,t_g) = (760 °C, 3 mins) for the InGaN QW layers and (T_g,t_g) = (800 °C, 9 mins) for the (In)GaN barrier layers.

The structural parameters of the two samples are listed in the Table V.1. The indium compositions of the different layers are extracted from EDX measurements on InGaN thick layers (~100 nm) grown under similar growth conditions. There is a strong gradient of the indium composition from the center to the edge of the sample wafer. The values given in Table V.1. correspond to the center of the wafers and in the following, the PL is also performed at the center of the wafers. We can remark that the In composition of the InGaN QWs of sample SP_1 is 0.23 and 0.35 for sample SP_2, while the growth conditions are identical for both samples. The larger In composition for sample SP_2 is due to the presence of the stress relaxed InGaN layer below the QWs which favours In incorporation.

Table V.1. Growth conditions and structural parameters of the $In_xGa_{1-x}N$/GaN QWs and $In_xGa_{1-x}N$/$In_yGa_{1-y}N$ QWs and the $In_yGa_{1-y}N$ thick layer.

Sample	Description	$In_yGa_{1-y}N$ buffer layer	QW		Barrier	
			In composition	Thickness (nm)	In composition	Thickness (nm)
SP_1	x5 MQW $In_xGa_{1-x}N$/GaN	no	0.23	3.4	0	7.6
SP_2	x5 MQW $In_xGa_{1-x}N$/$In_yGa_{1-y}N$ on $In_yGa_{1-y}N$ layer	y=0.12 90 nm	0.35	3.9	0.12	8.6

5.1.2. Photoluminescence measurements

To study the optical properties of the semi-polar samples, we decided to reproduce all photoluminescence (PL) measurements that we did in the previous studies for these two

samples. Firstly, we start by using the photo-excitation power dependent (PEPD) measurements at 8 K with an excitation energy of 4.66 eV (266 nm). The excitation power density varies from 1.3 x 10^{-2} W/cm^2 to 2.8 x 10^3 W/cm^2 (conditions very similar to those of chapter IV), but contrary to our experiments on polar QWs, we do not observe evidence of the Auger effect. In order to explore conditions with higher excitation densities, we used the second harmonic of the Ti:sapphire laser at 3.18 eV (390 nm) as the excitation source instead of the third harmonic one (266nm). With these conditions, the photo-injection power density can be varied from 4 x 10^{-1} W/cm^2 to 7 x 10^4 W/cm^2.

To keep the coherence between the different measurements, we used the excitation energy at 3.18 eV for all the other measurements: continuous-wave (CW) and time-resolved photoluminescence (TRPL). As we will see in the following, the CW temperature-dependent PL only gave a rough information about the strength of the localization effect in our two samples. Then, to further investigate the effects of the localization on the dynamic of the carrier recombination in these samples, TRPL measurements were also performed in the temperature range from 18 to 250 K.

5.2. Results and discussions

5.2.1. Temperature dependent photoluminescence

The two samples are dominated by broad PL spectra centered at 2.6 eV (blue) and 1.9 eV (red) at room temperature for sample SP_1 and SP_2, respectively (Fig. 5.1). These peaks are related to the InxGa1-xN MQW emission. For sample SP2, we also observe a peak at 2.8 eV attributed to the InyGa1-yN barrier emission. The QW emission peak of these spectra is actually structured by two peaks: one at the high energy (HE) wing and another at low energy one (LE), as reported in Figs. 5.1 (a)-(b). The HE peaks dominate the PL spectra of the samples. The energy difference between two peaks are larger than 92 meV, which indicates that the low energy peaks are not phonon replica of the high energy ones.

We remind that a laser wavelength of 390 nm is used as the excitation source, therefore no PL signal is observed from the GaN band-edge. For the sample SP_2, both the QWs and the barrier layers are excited, while for the sample SP_1 only the QWs are excited. At 150 K, a third peak at ~ 2.24 eV occurs in the PL spectrum of the QW and the PL intensity of the barrier layer is dramatically reduced, as plotted in Fig. 5.1 (c). Then, when the temperature further increases the intensity of this peak reduces and the PL intensity of

the barrier layer increases again. This relation indicates a resonance of signal of QW and the barrier layers. The peak at 2.24 eV is observed when increasing temperature thanks to some thermal population effect in the sample SP_2.

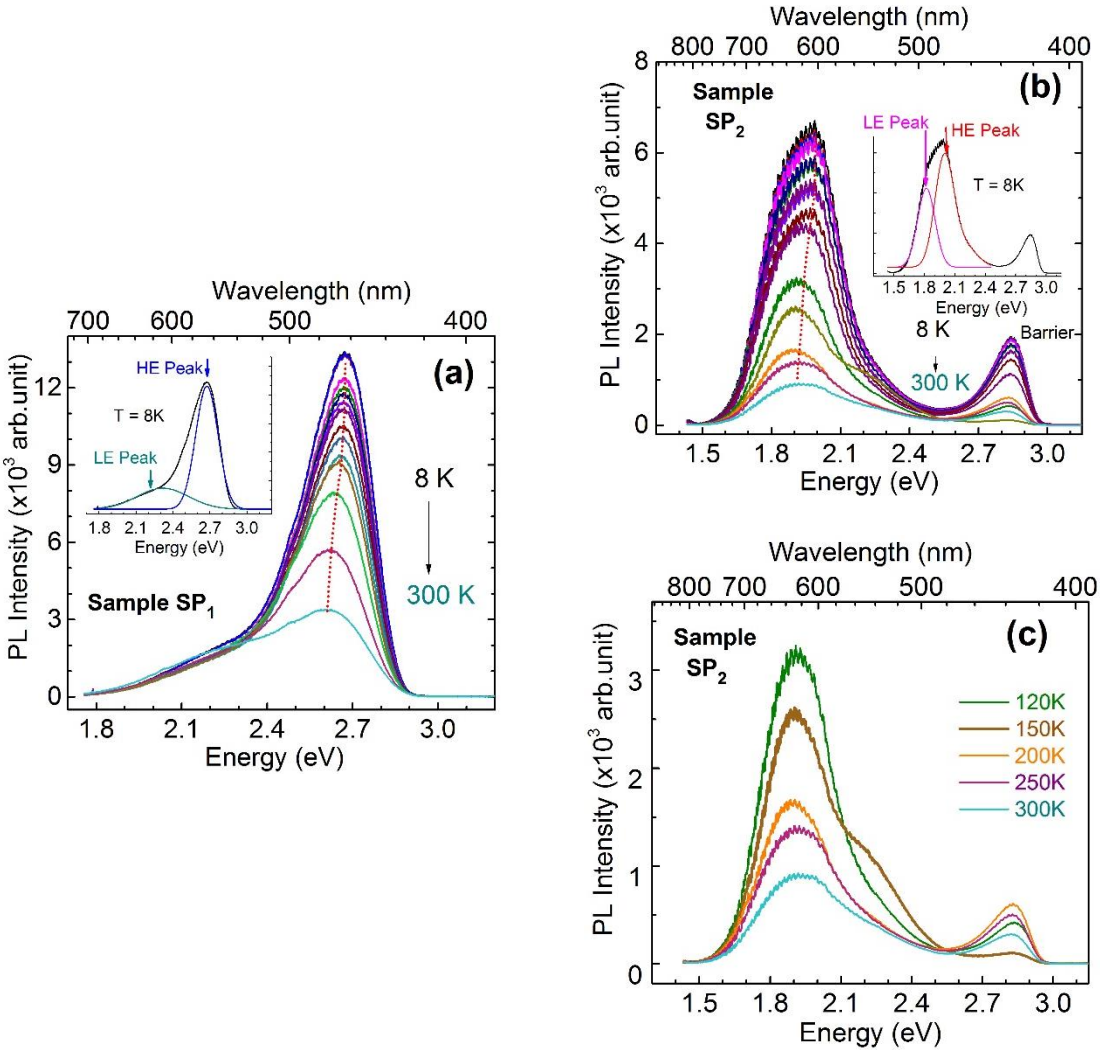

Figure 5.1. The photoluminescence features of the two samples with changing temperature (a): sample SP_1 and (b): sample SP_2. The insets show the spectra at 8 K of each sample consits of two peaks.

Figure 5.2 (a) shows the evolution of the PL peak energy with temperature for the two samples in the 8K to 250 K range. Both HE and LE peaks shift to lower energies when the temperature increases. The HE-peak slightly always red-shifts when increasing T while the LE energy weakly increases in the low T range and then red-shifts when further increasing T above 30K. The two PL peaks of sample SP2 display similar behaviors with constant energy up to a temperature of about 70 K. Above this temperature, the PL peak energies rapidly red-shift.

We remark that, in the case of the polar MQW samples, when changing the temperature, the PL peak energy increases again beyond a (de)localization temperature, Fig. 5.2 (b). There is no observation of this behavior for the two semi-polar samples. This indicates that the carrier localization is stronger in the semi-polar structure than in the polar ones. The different evolution of the peak energy with increasing temperature of the two samples is in relationship with the strength of the localization.[10] In both samples, the HE-peak exhibits larger red-shift than the LE-peak corresponding to the larger activation energies, as shown in Fig. 5.2 (c). This indicates that the strength of the localization effect of the HE peak is larger than that of the LE peak.

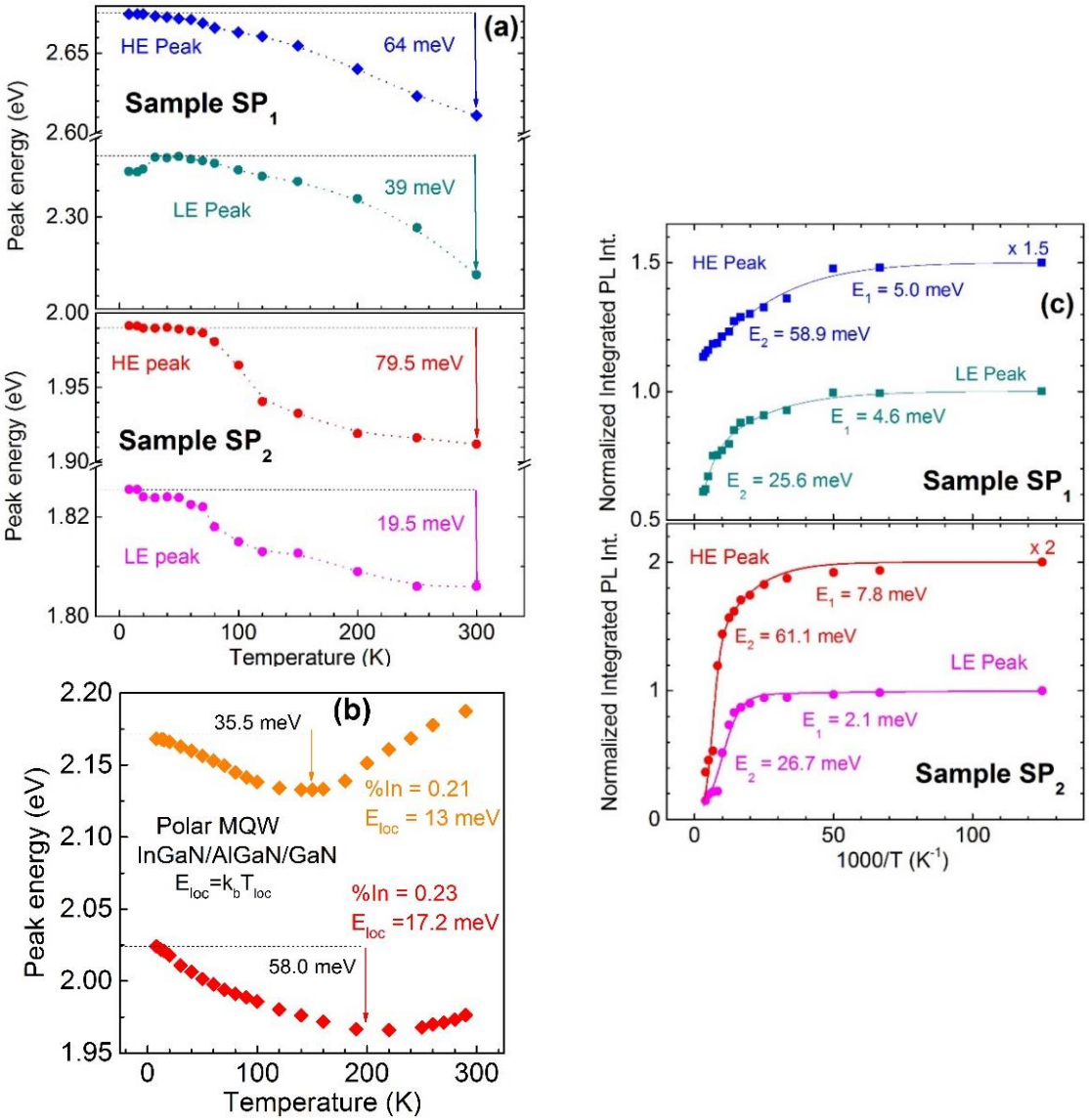

Figure 5.2. (a) The evolution of photoluminescence peak energy of the two samples with increasing temperature in comparison with (b) the data of the polar oriented multiple quantum well sample (M_4 and M_5 in the chapter III). (c) Arrhenius plots of samples with their fitting functions

5.2.2. Time-resolved photoluminescence measurements

After the photo-excitation pulses, the photo-generated carriers can either produce photon via radiative recombination process or recombine non-radiatively via different channels. When the lattice temperature increases, carriers are more mobile, lattice defects or trapping centers are more easily accessible to them. Consequently, the non-radiative decay time decreases as it is the invert of the non-radiative recombination rate. The PL transients of the carrier recombination dynamics of the two samples are reported in Fig. 5.3(a) and Fig. 5.3 (b) showing a decreasing of the PL decay times with increasing temperature from 18 K to 250 K. A single exponential decay is always found for the blue sample, SP_1, when temperature is varied. In the case of the red-light emitting sample, SP_2, a bi-exponential behaviour is measured when temperature is under 150 K. Beyond this temperature, the two decay components merge together to make a single exponential decay. This is interpreted in terms of carrier localization effect in the In-rich regime of the InGaN QW of the sample SP_2 as this sample is grown with a high indium composition (0.35). The PL decay times of the two samples are plotted in Fig. 5.3 (c) as a function of the temperature. At a given temperature, the sample SP_1 exhibits shorter decay time than sample SP_2 does.

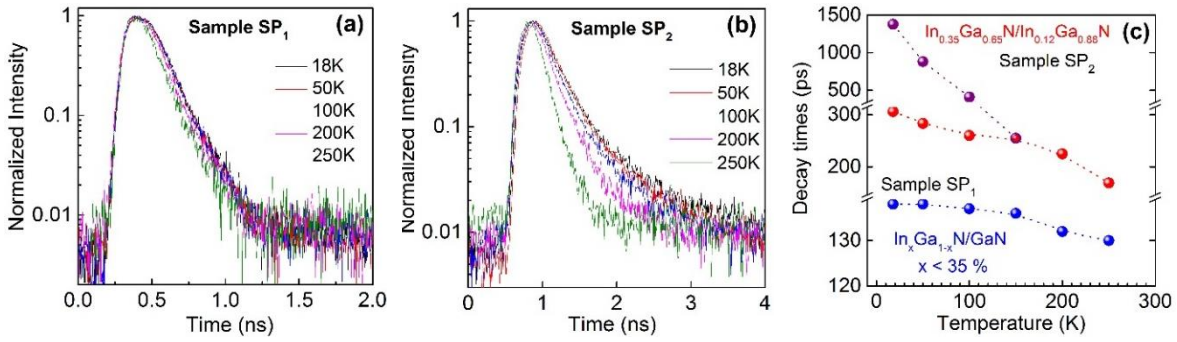

Figure 5.3. The photoluminescence transient of two samples at different temperature in the 18 K to 300K range (a): sample SP_1 and (b): sample SP_2. (c) Decay times of the samples extracted from the experimental data. Dashed lines are guides to the eyes.

The relative contribution of the radiative and non-radiative recombination rates to the photoluminescence intensity is varied with changing temperature. The internal quantum efficiency (IQE) is determined as:

$$IQE = \frac{1/\tau_{rad}}{1/\tau_{rad} + 1/\tau_{nonrad}} = \frac{1/\tau_{rad}}{1/\tau_{PL}} \quad (5.1)$$

where τ_{rad}, and $\tau_{non\text{-}rad}$ are radiative and non-radiative decay times.

We arbitrary assume that at low temperature (18 K), the IQE of sample SP_1 is 80% and the IQE of sample SP_2 is 50 %. IQE of SP_1 is taken below 100 % as we did not make a large number of growth runs, and the PL intensity of SP_2 is 80 % lower than for the polar growth orientation. This will slightly impact the number but not the physics. For sure we cannot reasonably claim to have 100% IQE for the red light-emitting sample. Then, value of the IQE at temperature T can be calculated by the ratio of the integrated PL intensity at T and at 18 K expressed as:

$$IQE_{(T)} = IQE_{(18K)} \frac{I_{(T)}}{I_{(8K)}} \tag{5.2}$$

Combining the Eq. (5.1) and Eq. (5.2) gives us a relation between the radiative decay time, photoluminescence decay time, and the photoluminescence intensity as:

$$\tau_{rad} = \frac{\tau_{PL}}{\frac{I_{(T)}}{I_{(18K)}}} \tag{5.3}$$

Then, value of the non-radiative decay time is calculated by using this equation

$$\frac{1}{\tau_{nonrad}} = \frac{1}{\tau_{PL}} - \frac{1}{\tau_{rad}} \tag{5.4}$$

Knowing the values of the PL decay times and the ratio $I_{(T)}/I_{(18K)}$ allow us to determine the values of the radiative and non-radiative decay times at different temperatures, as plotted in Figs. 5.4 (a)-(b). In the low temperature range, the radiative decay time is short and it dominates the PL decay time for both samples. When the temperature reaches higher values, the radiative decay time becomes longer. For the sample SP_1, the radiative decay time increases slowly with a small average slope of 0.53 $ps.K^{-1}$, inset of the Fig. 5.4 (a). This value is lower than the expected $8ps.K^{-1}$ value expected for free excitons,[11] which indicates a weak carrier localization in this sample, hence carrier can freely propagate through the structures at high temperature. In the case of the sample SP_2, the radiative decay time increases with two slopes: a very small slope in the 18 K to 100 K temperature and a higher slope of 7.9 $ps.K^{-1}$ temperatures above 100K (Fig. 5.4 (c)). This behavior is a probe of strong carrier localization in the In-rich InGaN QW layer at low T and a progressive de-trapping when increasing T.[11-13] As the bandgap of InGaN material depend on alloy composition, Eq. 4.1, any difference in the In composition from the average value originates bandgap potential where carriers are localized at local potential minima. The indium composition of the sample SP_2 is estimated about 35 % corresponding the range of high photoluminescence broadening due to the alloy disorder

occurs in InGaN materials.[14] It presents a large fluctuation of In composition source of strong localization in this sample.

When temperature increases from 18 K to 250 K, the non-radiative decay time gets shorter and shorter. The non-radiative recombination is the dominating channel when temperature is higher than 200 K and 150 K for the sample SP_1 and SP_2, respectively. This behavior relates to non-radiative recombination processes of free carriers. Below 200 K or 150 K, carriers are localized at spatial potential minima, weakly localized in sample SP_1 and strongly localized in sample SP_2. This prevents carriers to migrate towards the trapping centers. Beyond these temperatures, carrier freely move through the whole structure and they easily reach lattice defects and then, recombine non-radiatively.

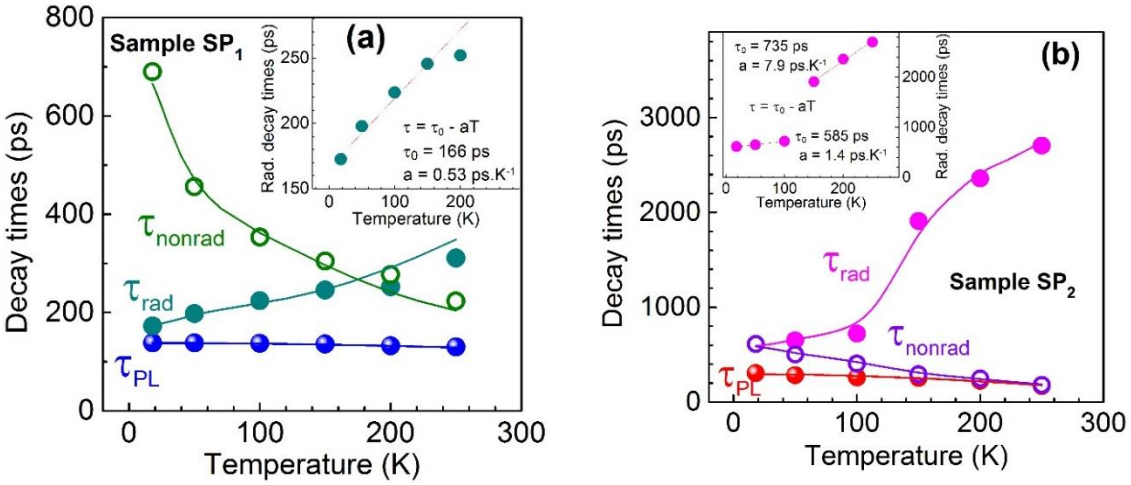

Figure 5.4. The evolution of the PL decay time, radiative and non-radiative decay times as fiuntions of temperature for (a): sample SP_1 and (b): sample SP_2.

To extract more information about the localization of carriers in the sample SP_2, a time-integrated TRPL at 18 K is analyzed. In Fig. 5.5 (a), an overlap at low energy regime of the PL spectra after a short excitation pulse and after a long excitation pulse is a probe of the localization in such sample. As we discussed earlier, at 18 K, the decay time of this sample has two components: a short decay and a long one. In Fig. 5.5 (b), the decay times decrease with the increase of the PL energy. The evolution of the decay time versus the transition energy can be expressed by:[15-17]

$$\tau = \frac{\tau_0}{1+\exp(\frac{E-E_0}{\Delta_0})} \qquad (5.5)$$

where τ_0 and E_0 are a characteristic average value of decay time, a typical energy analogous to a mobility edge in bulk alloys, and Δ_0 accounts for the depth of the localization.

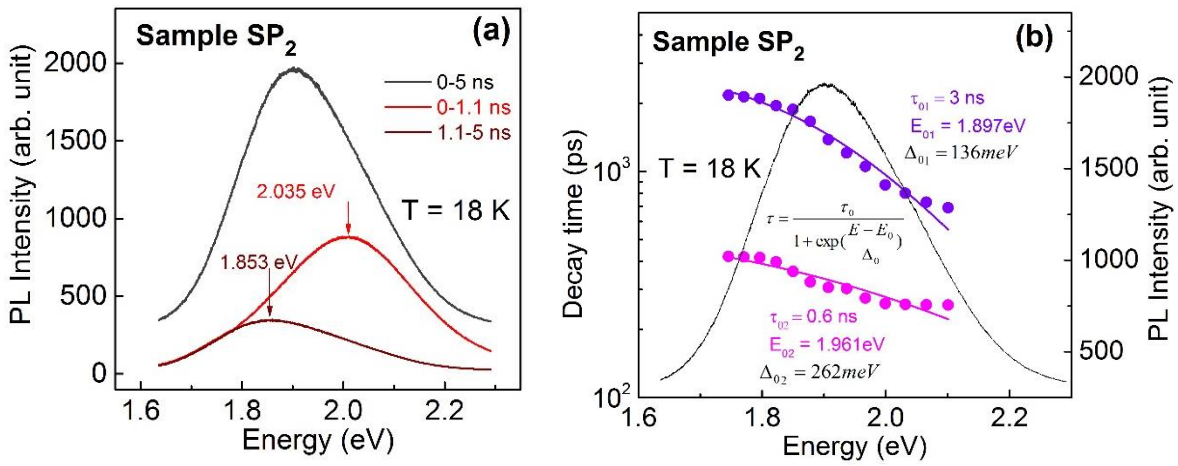

Figure 5.5. (a) The time-integrated photoluminescence spectra of the sample SP_2 at 8 K after short, long, and whole integration times. (b) The spectral dependence of the two decay components.

After a carefully fit of the experimental data with the Eq. 5.5, we find Δ_{01} and Δ_{02} values of 136 meV and 262 meV, for the long and short decay times, respectively. The larger value of Δ_{02} = 262 meV for the short decay time indicates a deeper localization. We believe that this component is mainly related to fluctuations of the average chemical composition (maybe a spinodal decomposition but TEM experiment is not realized at the time of writing) rather than to chemical disorder due to random distribution of Ga and In atoms.

5.2.3. Power dependent photoluminescence

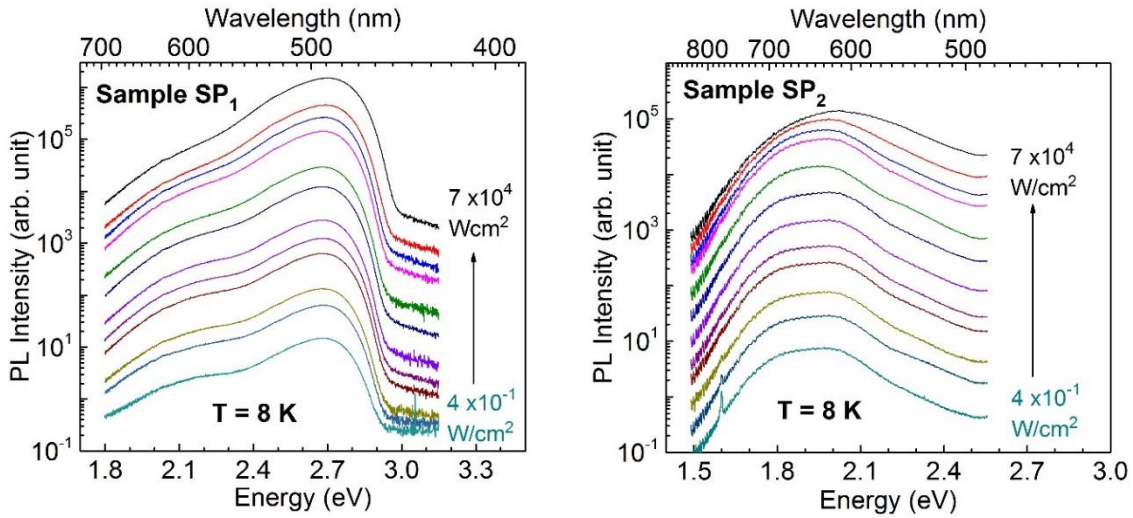

Figure 5.6. The 8 K photoluminescence spectra of the two samples under photo-excitation density varying in 4 x 10^{-1} to 7 x10^4 W/cm^2 range.

Figure 5.6 shows 8 K photoluminescence spectra of the samples with changing the excitation power density. It is clearly shown that at low excitation level, the PL spectra of the two samples consist of two peaks. The PL spectra of two samples keep their shapes until the power density reaches a value of 7 x10^4 W/cm^2.

The WL at 390 nm is used as the excitation source giving a non-identical excitation condition for the two samples: resonant excitation for the sample SP_1, and non-resonant excitation for the sample SP_2. Therefore, the photo-generation rates of carriers in the two samples are different. The carriers are generated only in the QWs of the sample SP_1, while the generated carriers in the QWs of the sample SP_2 are also coming by diffused carriers from the barrier layer. When the excitation WL at 266 nm is used to have non-resonant excitation for both samples, almost the same evolutions of the integrated PL intensity with increasing photo-excitation density are found than when the WL at 390 nm is used, as plotted in Fig. 5.7 (a). Therefore, it is supposed here that using the excitation WL at 390 nm or 266 nm does not impact the values of thresholds P_T for changing the slope dependence from linear to sub-linear.

The thresholds P_T are 1.2 x 10^4 and 1.1 x 10^3 W/cm^2 for the blue sample and for the red sample, respectively, reported in Fig. 5.7 (b). These values are approximately 200 times higher than that of the polar oriented samples, at a similar emission wavelength, Fig. 5.7 (c). This is mainly due to the reduction of the internal electric field by growing sample along semi-polar direction. Decreasing the internal electric field reduces the carrier life time, and therefore the carrier density decreases since it is proportional to the radiative life time, as shown in Figs. 5.7 (c)-(e). This result shows that semi-polar structure is one option for the growth of high efficiency long wavelength emitters.

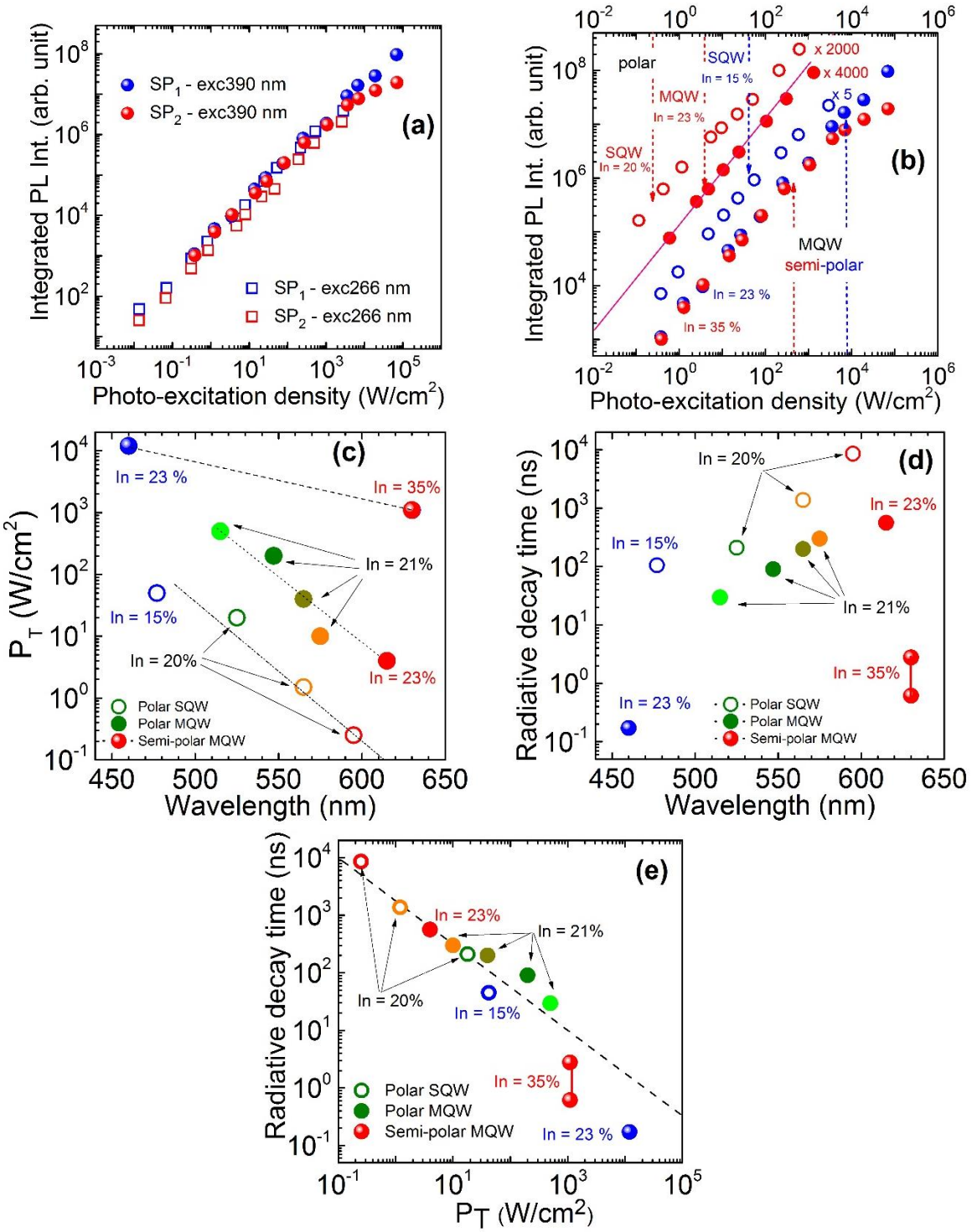

Figure 5.7. (a) Integrated photoluminescence intensity as a function of the photo-excitation power density under excitation wavelength at 266 nm and at 390 nm. (b) Evolution of the integrated photoluminescence intensity with increasing photo-excitation power density of the two semi-polar samples in comparison with polar single quantum well and polar multiple quantum wells. The values of the PL integrated intensity of the polar samples are multiplied by factors of 5, 4000 and 2000. (c)-(d) Plots of the threshold P_T and radiative decay times as functions of the emission wavelength and (e) Plot of radiative decay time at low temperature versus the threshold P_T.

References

1. H. Fu, Z. Lu, X. H. Zhao, Y.-H. Zhang, S. P. DenBaars, S. Nakamura, and Y. Zhao, J. Display Technol. **12**, 736 (2016)
2. R. Nakamura, and M. R. Krames, Proc. of the IEEE **101**, 2211 (2013)
3. M. J. Davies, P. Dawson, S. Hammersley, T. Zhu, M. J. Kappers, C. J. Humphreys, and R. A. Olive, Appl. Phys. Lett. **108**, 252101 (2016)
4. E. Kioupakis, Q. Yan, D. Steiauf, and C. G Van de Walle, New J. Phys. **15**, 125006 (2013)
5. N. Kriouche, Thesis: ‘‘Croissance et propriétés optiques et structurales de nitrures semipolaires (11-22) hétéro-épitaxiés sur saphir’’, l’universite de Nice-Sophia Antipolis2011
6. N. Okada, K. Uchida, S. Miyoshi, and K. Tadatomo, Phys. Status Solidi A **209**, 469 (2012)
7. F. Tendille, P. De Mierry, P. Vennéguès, S. Chenot, M. Teisseire, Journal of Crystal Growth **404**, 177 (2014)
8. J. Kim, D. Min, J. Jang, K. Lee, S. Chae, and O. Nam, J. Appl. Phys. **116**, 163109 (2014)
9. N. Okada, Y. Okamura, K. Uchida, and K. Tadatomo, Optical Materials **58**, 243 (2016)
10. W. Bao, Z. Su, C. Zheng, J. Ning, and S. Xu, Sci Rep **6**, 34545 (2016)
11. D. Rosales, B. Gil, T. Bretagnon, J. Brault, P. Vennéguès, M. Nemoz, P. de Mierry, B. Damilano, J. Massies, and P. Bigenwald, J. Appl. Phys. **118**, 024303 (2015)
12. A. Hangleiter, T. Langer, P. Henning, F. A. Ketzer, P. Horenburg, E. R. Korn, H. Bremers, and U. Rossow, Proc. of SPIE **10104**, 101040Q (2017)
13. B. Liu, R. Smith, M. Athanasiou, X. Yu, J. Bai, and T. Wang, Appl. Phys. Lett. **105**, 261103 (2014)
14. M. Moret, B. Gil, S. Ruffenach, O. Briot, C. Giesen, M. Heuken, S. Rushworth, T. Leese, and M. Succi, J. Cryst. Growth **311**, 2795 (2009)
15. C. Gourdon, and P. Lavallard, Phys. Stat. Sol. B **153**, 641 (1989)
16. D. Rosales, H. T. Ngo, P. Valvin, K. Lekhal, B. Damilano, P. De Mierry, B. Gil, and T. Bretagnon, Superlattice Microst. **76**, 9 (2014)
17. H. T. Ngo, D. Rosales, B. Gil, P. Valvin, B. Damilano, K. Lekhal, P. De Mierry, Proc. SPIE **9363**, 93630K-1 (2015)

CONCLUSION

Along the preceding chapters, firstly, I tried to offer you the experimental evidence of the different mechanism that rule the performances of long-wavelength emitting nitride-based InGaN/(Al)GaN quantum wells grown along the polar direction.

I brought the experimental proof of the existence of both radiative and non-radiative carrier recombination even at low temperature, whereas it is generally assumed an internal quantum efficiency of 100% at low temperature. Increasing the temperature increases substantially the non-radiative recombination rate.

I have also brought the experimental evidence of the possibility to increase the internal quantum efficiency (IQE) by growing multiple quantum well samples with improved crystalline quality. This can be realized in particular by embedding an AlGaN strain compensating layer between the InGaN active layer and one of the GaN barrier layers. The thickness of such AlGaN layer can be adapted so that the total elastic strain is compensated in the whole structure. Then, when lattice matching to GaN is realized, the X-rays diffraction feature brings us the evidence of such lattice matching or it brings us the evidence of an almost perfect one. Simultaneously, the diffraction satellite peaks appear nicely contrasted as the probe of good interface roughness. Even if this control is not perfect we have shown what state of the art is.

A simple CW PL experiment indicates, from the PL intensity obtained under similar photoexcitation conditions, that the low temperature IQE can be enhanced by an amount of 14% (from 50% to 57 %) by just growing such strain compensating layer, this for samples emitting yellow light, orange one and even red one.

To obtain the LT IQE values, we have used time-resolved PL spectroscopy and a model that correlates the IQE to the proportion of the radiative and non-radiative recombination rates at low temperature in these inhomogeneous samples. Under very low excitation conditions, we observe both a long decay time that is interpreted as being the radiative decay time and a shorter one that is a mixing of radiative and non-radiative decay times. From the relative proportion of these characteristic carrier recombination times, this model offers us the possibility to frame the values of IQE.

We remark that the insertion of the AlGaN strain compensating layer reduces the value of the radiative recombination rate due to the increase of the internal electric field in the active InGaN QW layers. Simultaneously, the enhancement of the crystalline quality reduces the density of defect hence reducing the non-radiative SRH recombination. At the end, the balancing contribution of both effects leads to the enhancement of the IQE thanks to the dominating effect of the reduction of SRH.

As we targeted the determination of the IQE under high photoexcitation conditions, we have performed complementary experiments by changing the pump power density through 5 decades. In the low range of photoexcitation densities, there is a linear relationship between the pump power and the PL intensity. Then, beyond a critical threshold value P_T one observes a sub-linear dependence. This threshold value decreases with increasing wavelength which is correlated to an increase of the decay times, that is to say an increase of the QCSE and the localization of electron and holes at different interface of the quantum well layers.

We have studied a series of single quantum well samples (SQWs) and we found that the values of P_T are smaller than for MQWs at a given wavelength. Again, we correlate this to the impact of the QCSE slightly higher for a SQW than for a MQW.

To interpret the evolution of IQEs versus pump power density, we have taken the balance between the radiative to non-radiative recombination rates by assuming two contributions: the SRH one and the Auger recombination one. Then, the IQE is written as

$$IQE = \frac{\Gamma_{rad}}{\Gamma_{SRH} + \Gamma_{rad} + \Gamma_{Auger}}$$

The radiative recombination rate is proportion to the number of electron and to the number of holes. The SRH effect has two proportionality coefficients: one for the electrons and one for the hole and it varies proportionally to the density of carriers:

$$\Gamma_{SRH} = A_n n + A_p p.$$

The non-radiative Auger recombination results of three-particle scattering where one electron and one hole recombine while promoting the energy of a third electron (or hole) into the conduction band (or valence band). Then it is an nnp or a ppn Auger type recombination. This non-radiative Auger recombination rate is written as:

$$\Gamma_{Auger} = C_n nnp + C_p ppn$$

At the end, the IQE can be rewritten as

$$IQE = \frac{Bnp}{A_n n + A_p p + Bnp + C_n nnp + C_p ppn}$$

In our samples here, we have a substile n-type doping (n_0), we had to adapt this ABC model to our samples.

After carefully fitting of the PL versus pump power data, we have been able to correlate the values of A, B, and C coefficients with the emission wavelength. We find a close correlation between the values of B and C. This indicates that the electrostatic repulsion between the electrons localized at a given interface triggers the Auger effect. Of course, the influence of localization is important, but it is not found to be the dominating mechanism.

Our results indicate that internal electric fields and huge QCSE bottleneck and even jeopardize the possibility to highly luminescent devices based on nitrides grown along the polar direction. It is therefore critical for long wavelength emitters to reduce as far as possible the radiative lifetime. The only way to achieve this objective for polar QWs is to target structures with very thin QWs and a very high In composition. Such parameters are difficult to achieve while keeping a high material quality. Reaching yellow or red emission with polar InGaN QWs will always result from a compromise between the material quality, and the QCSE.

By increasing the sample temperature, we could determine the activation energies for the non-radiative recombination. Our results are compatible with ***an enhancement of the Auger effect (AE) due to the interaction of other phonon than the LO ones.*** Finally, we have dedicated a little time to structures of red-light emitting QWs grown along the [11-22] semi-polar orientation on stress relaxed InGaN buffer layers. Our TRPL measurement reveal that the radiative lifetimes are orders of magnitude smaller than for polar QWs showing a small QCSE. Furthermore, at a given wavelength, the onset of AE is at a threshold power density about 200 times higher than for the samples grown along the polar orientation. These complementary investigations realized at the end of my PhD work are of course preliminary but they unambiguously demonstrate that semi-polar orientation is one of the options for the growth of highly luminescent red-light emitters based on nitrides.

CONCLUSION (en Français)

Ce travail de doctorat est dédié à l'étude des mécanismes régissant l'interaction lumière-matière dans des dispositifs optoélectroniques à base d'alliages (Al,Ga,In,)N. Diverses compositions de ces alliages sont assemblées en structures multicouches de matériaux d'épaisseurs nanométriques afin d'obtenir une émission à plus grande longueur d'onde que le bleu, couleur pour laquelle la technologie est mature depuis plus de vingt ans. Il s'agit de réaliser des émetteurs efficaces de lumière jaune, verte ou blanche (avec une approche alternative au pompage optique de luminophore par une diode bleue). Les solutions solides assemblées pour obtenir des émissions à grandes longueur d'onde sont à base de GaN et de $Ga_{0.8}In_{0.2}N$, matériaux pour lesquels les mailles cristallographiques sont désaccordées. Lorsqu'elles sont déposées sur un substrat ou un pseudo-substrat de GaN, matériau pour lequel les dopages n et p sont maitrisés et permettent l'injection électrique des porteurs, les tranches de $Ga_{0.8}In_{0.2}N$ subissent de très fortes compressions dans leur plan de croissance et l'énergie élastique est relaxée par la formation de défauts délétères pour le rendement lumineux. Nous avons construit des hétéro-structures plus complexes en intercalant une couche complémentaire d'$Al_{0.2}Ga_{0.8}N$ afin de réduire la densité d'énergie élastique globale. L'insertion de telles couches améliore la qualité cristalline et augmente leur rendement optique.

Nous avons mesuré le rendement quantique interne en utilisant la spectroscopie de photoluminescence résolue en temps et une analyse des temps de déclins par une approche de type Lotka-Volterra des équations de recombinaison pour obtenir les taux de recombinaisons radiatifs et non-radiatifs. Nous avons montré quantitativement comment les champs électriques internes résultant du contraste de polarisation électrique aux interfaces et les recombinaisons non-radiatives de type Schockley-Read-Hall contribuent à définir le rendement quantique à faible densité d'excitations (optique ou électrique). L'objectif est l'obtention d'une émission spontanée intense pour une densité d'excitation modérée. Nous avons donc conduit une campagne d'expériences en variant l'intensité d'injection. Nous avons montré que l'effet Auger est le facteur dominant régissant la chute du rendement quantique interne sous fortes densités d'injection. Nous avons étudié diverses architectures à simple puits quantique ou à puits quantiques multiples émettant à des longueurs d'onde identiques pour quantifier l'influence spécifique de l'effet Stark

confiné quantique. Nous avons corrélé l'apparition d'un seuil d'excitation au-delà duquel domine la recombinaison non-radiative de type Auger avec l'augmentation du temps de recombinaison radiative et de l'énergie de localisation des porteurs dans l'alliage inhomogène. Nous arrivons à la conclusion que la localisation des porteurs produite par le champ électrique aux interfaces et les fluctuations de la composition chimique de $Ga_{0.8}In_{0.2}N$ contribuent de concert, facilitant l'interaction répulsive électron-électron et la recombinaison non-radiative Auger nnp. Nous avons montré que le modèle ABC permet de bien décrire la physique du phénomène si ses trois paramètres tiennent compte des effets d'écrantages sous injections modérées et des effets de remplissage de l'espace des phases sous fortes injections. Enfin, nous nous sommes écartés de l'étude des structures traditionnellement épitaxiées selon le plan polaire (0001) pour choisir des plans d'épitaxie semi-polaire (11-22). Dans ces conditions, il a été nécessaire de fabriquer des puits quantiques en $Ga_{0.65}In_{0.35}N$. Nous avons montré que la quasi-absence d'effet Stark confiné quantique augmente de manière très significative le seuil d'excitation au-delà duquel domine la recombinaison non-radiative de type Auger. Cette amélioration par rapport aux échantillons épitaxiés selon le plan (0001) est d'autant plus marquée que la longueur d'onde émise est grande.

LIST OF PUBLICATIONS

The thesis is based on results of the following papers:

1) T. H. Ngo, B. Gil, B. Damilano, K. Lekhal, and P. de Mierry, *Internal quantum efficiency and Auger recombination in green, yellow and red InGaN-based light emitters grown along the polar direction*.
   Superlattices Microstruct. **103**, 245 (2017)
2) T. H. Ngo, B. Gil, P. Valvin, B. Damilano, K. Lekhal, and P. De Mierry, *Auger effect in yellow light emitters based on InGaN–AlGaN–GaN quantum wells.*
   Japanese Journal of Applied Physics **55**, 05FG10 (2016)
3) K. Lekhal, B. Damilano, Huong Thi Ngo, D. Rosales, P. De Mierry, S. Hussain, P. Vennéguès and B. Gil. *Strain-compensated (Ga,In)N/(Al,Ga)N/GaN multiple quantum wells for improved yellow/amber light emission*.
   Applied Physics Letter **106,** 142101 **(**2015)
4) T. H. Ngo, B. Gil, P. Valvin, B. Damilano, K. Lekhal and P. De Mierry. *Internal quantum efficiency in yellow-amber light emitting AlGaN-InGaN-GaN heterostructures.*
   Applied Physics Letter **107,** 122103 (2015)
5) H. T. Ngo, D. Rosales, B. Gil, P. Valvin, B. Damilano, K. Lekhal and P. de Mierry. *Photoluminescence behavior of amber light emitting GaInN-GaN heterostructures*.
   Proc. SPIE 9363, Gallium Nitride Materials and Devices X, 93630 (2015)
6) D. Rosales, H. T. Ngo, P. Valvin, K. Lekhal, B. Damilano, P. De Mierry, B. Gil, T. Bretagnon. *The universal photoluminescence behaviour of yellow light emitting (Ga,In)N/ GaN heterostructures.*
   Superlattices and Microstruct. **76,** 9-15 **(**2014)

Other publications:

1) J. Brault, S. Matta, T. H. Ngo, M. Korytov, D. Rosales, B. Damilano, M. Leroux, P. Vennéguès, M. Al Khalfioui, A. Courville, O. Tottereau, J. Massies, and B. Gil. *Investigation of AlyGa1-yN/$Al_{0.5}Ga_{0.5}N$ quantum dot properties for the design of ultraviolet emitters.*
   Japanese Journal of Applied Physics **55**, 05FG06 (2016)
2) J. Brault, S. Matta, T. H. Ngo, D. Rosales, M. Leroux, B. Damilano, M. Al Khalfioui, F. Tendille, S. Chenot, P. De Mierry, J. Massies, and B. Gil. *Ultraviolet light emitting diodes using III-N quantum dots.*
   Materials Science in Semiconductor Processing **55,** 95 (2016)